

METROLOGY AND SIMULATION WITH PROGRESSIVE  
ADDITION LENSES

by  
Dulce Gonzalez Utrera

---

Copyright © Dulce Gonzalez Utrera 2018

A Dissertation Submitted to the Faculty of the  
COLLEGE OF OPTICAL SCIENCES  
In Partial Fulfillment of the Requirements  
For the Degree of  
DOCTOR OF PHILOSOPHY  
In the Graduate College  
THE UNIVERSITY OF ARIZONA

2018

THE UNIVERSITY OF ARIZONA  
GRADUATE COLLEGE

As members of the Dissertation Committee, we certify that we have read the dissertation prepared by **Dulce Gonzalez Utrera**, titled ***Metrology and Simulation with Progressive Addition Lenses*** and recommend that it be accepted as fulfilling the dissertation requirement for the Degree of Doctor of Philosophy.

  
\_\_\_\_\_  
**James Schwiegerling**

Date: 11/20/18

  
\_\_\_\_\_  
**Dae Wook Kim**

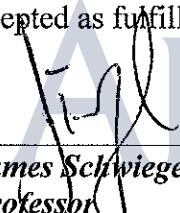
Date: 11/20/18

  
\_\_\_\_\_  
**Rongguang Liang**

Date: 11/20/18

Final approval and acceptance of this dissertation is contingent upon the candidate's submission of the final copies of the dissertation to the Graduate College. ®

I hereby certify that I have read this dissertation prepared under my direction and recommend that it be accepted as fulfilling the dissertation requirement.

  
\_\_\_\_\_  
**James Schwiegerling**  
**Professor**  
**Optical Sciences/Ophthalmology**

Date: 11/20/18

## ACKNOWLEDGMENTS

First and foremost, my sincere appreciation and gratitude to my advisor Dr. Jim Schwiegerling for his mentorship, his guidance and his constant support throughout these years. I would also like to thank the committee members Dr. Dae Wook Kim and Dr. Ron Liang, for their valuable feedback.

Thank you to my colleagues in the Visual and Ophthalmic Optics Lab: Eddie LaVilla, Brian Redman, Carmen Paleta, Carl Chancy, William Duncan, Ashley Valdez, Yu Yan, Sean Ashley, Jieun Ryu, Martin Chao-Hsiung Tseng, Ethan Tank, Soheila Boojari, Yuqiao Han for their valuable comments and help throughout the completion of my PhD .

I would like to thank María and Mohan for being true friends and my support throughout these years. Your friendship has been irreplaceable.

I am thankful to Oscar, whose constant encouragement and endless patience have helped me come this far. Thank you to my family, especially to my parents and my brother without whom I would not be here.

Finally, all my gratitude to Liliana, Poonam, Sandra, Phillipi, Rodolfo, Itzel, Itzel, Gaby, Pabli, Ismael, Juan Manuel and all my friends for making my time in Tucson a unique experience.

I would like to acknowledge CONACyT and TRIF University of Arizona for their financial support.

## DEDICATION

*To my loving grandmothers, Dolores and Catalina.*

## TABLE OF CONTENTS

LIST OF FIGURES . . . . .	<b>7</b>
LIST OF TABLES . . . . .	<b>10</b>
ABSTRACT . . . . .	<b>11</b>
CHAPTER 1. INTRODUCTION . . . . .	<b>12</b>
1.1. The Eye . . . . .	12
1.2. Presbyopia . . . . .	14
1.3. Treatments. . . . .	17
1.3.1. Intraocular Lenses . . . . .	17
1.3.2. Contact Lenses . . . . .	20
1.3.3. Reading Glasses and Bifocal Spectacles. . . . .	22
1.3.4. Progressive Addition Lenses Design . . . . .	23
1.4. Motivation . . . . .	27
CHAPTER 2. METROLOGY OF PROGRESSIVE ADDITION LENSES	<b>29</b>
2.1. Profilometer. . . . .	32
2.1.1. Profilometer Specifications. . . . .	32
2.1.2. Data Collection. . . . .	33
2.1.3. Fitting Data. . . . .	34
2.1.4. Profilometer Results . . . . .	37
2.2. Coordinate Measuring Machine . . . . .	41
2.3. Phase-Shifting and Phase Unwrapping . . . . .	45
2.4. SCOTS . . . . .	46
2.4.1. Principle . . . . .	47
2.4.2. Experimental Setup . . . . .	47
2.4.3. Results . . . . .	48
2.5. UV Deflectometry . . . . .	50
2.5.1. Theory . . . . .	51
2.5.2. Illumination System . . . . .	53
2.5.3. Experimental Setup . . . . .	55
2.5.4. System Calibration . . . . .	57
2.5.5. Fitting Data . . . . .	61
2.5.6. Calibration Sphere . . . . .	63
2.5.7. Results . . . . .	64
2.5.8. Conclusions and Future Work . . . . .	66

TABLE OF CONTENTS—*Continued*

CHAPTER 3. SIMULATION OF MULTIFOCAL VISION . . . . .	<b>68</b>
3.1. Theory and Image Simulation. . . . .	68
3.2. Algorithm Overview. . . . .	70
3.3. <i>Psf</i> Database Creation. . . . .	71
3.3.1. Lens-Eye Model . . . . .	72
3.3.2. Point Spread Function Interpretation. . . . .	75
3.3.3. Point Spread Function Scaling . . . . .	76
3.3.4. Point Spread Function Interpolation . . . . .	77
3.3.5. Point Spread Function Scaling . . . . .	82
3.4. Realistic Simulation . . . . .	89
3.4.1. Wide Field Angle and Distortion . . . . .	90
3.4.2. Image Size. . . . .	92
3.4.3. Image Segmentation and Depth of Field. . . . .	96
3.4.4. RGB Color Model. . . . .	99
3.5. Algorithm Implementation. . . . .	101
3.6. Results. . . . .	103
3.6.1. Results for Three Different Regions. . . . .	103
3.6.2. High Performance Computer. . . . .	104
3.6.3. Final Simulation. . . . .	106
CHAPTER 4. CONCLUSIONS AND FUTURE WORK . . . . .	<b>109</b>
APPENDIX A. ZERNIKE COEFFICIENTS . . . . .	<b>112</b>
APPENDIX B. SOURCE CODE USED TO PERFORM SIMULATION OF MULTI- FOCAL VISION. . . . .	<b>113</b>
REFERENCES . . . . .	<b>121</b>

## LIST OF FIGURES

FIGURE 1.1.	Eye anatomy. . . . .	13
FIGURE 1.2.	Example of a close object through a presbyopic eye. . . . .	15
FIGURE 1.3.	Amplitude of accommodation vs. age. From [1]. . . . .	16
FIGURE 1.4.	AcriSof IQ ReSTOR multifocal IOL Image [2]. . . . .	19
FIGURE 1.5.	Alcon Multifocal Contact Lenses [3]. . . . .	21
FIGURE 1.6.	Bifocal Spectacles. Visible change in power between distance and near region. The lower image shows the abrupt change in magnification (from [4]) . . . . .	23
FIGURE 1.7.	Zones of a Progressive Addition Lens. The right image shows the smooth transition in magnification from the distance region to the near region. (from [4]) . . . . .	25
FIGURE 2.1.	Interferogram of the Progressive Addition Lens under test. . . . .	31
FIGURE 2.2.	MarSurf CD 120 Linear Profilometer. . . . .	33
FIGURE 2.3.	Progressive Addition Lens measured by Profilometer. . . . .	34
FIGURE 2.4.	Freeform Surface from Profilometer data. . . . .	37
FIGURE 2.5.	Freeform Surface from Profilometer data with low terms removed. . . . .	38
FIGURE 2.6.	Differences in micrometers from Profilometer Data and Surface Fitting. . . . .	39
FIGURE 2.7.	Mean Curvature of Zernike Surface. . . . .	40
FIGURE 2.8.	Sample points from the Coordinate Measuring Machine. . . . .	42
FIGURE 2.9.	Differences from CMM Data and Fitting Data. . . . .	43
FIGURE 2.10.	Freeform Surface Fitting using CMM Data. . . . .	43
FIGURE 2.11.	Comparison between profilometer data and CMM data. . . . .	44
FIGURE 2.12.	Curvature Maps of the freeform surface. . . . .	44
FIGURE 2.13.	SCOTS experimental setup. . . . .	48
FIGURE 2.14.	Differences between profilometer and SCOTS data (b) Differences between profilometer and SCOTS data after a 180 degrees rotation. . . . .	49
FIGURE 2.15.	Differences between profilometer data and average of rotations. . . . .	50
FIGURE 2.16.	PMMA Transmission Plot. . . . .	52
FIGURE 2.17.	Fringe projection with an LED $\lambda = 365nm$ . . . . .	54
FIGURE 2.18.	Irradiance profile at the screen with lateral displacement. (a) 10 mm (b) 25 mm (c) 30 mm (d) 35 mm. . . . .	55
FIGURE 2.19.	Linear Relation of irradiance profile phase shift in function of lateral displacement of the object. . . . .	56
FIGURE 2.20.	Deflectometry Experimental Setup. . . . .	57
FIGURE 2.21.	Reflected fringes into calibration Sphere. . . . .	58
FIGURE 2.22.	(a) Intersection of lines. (b) Original Data. (c) Nominal Grid. . . . .	58

LIST OF FIGURES—*Continued*

FIGURE 2.23. Comparison between Nominal Grid and Undistorted Data. . . .	61
FIGURE 2.24. (a) Original map Phase in X from Reference Sphere. (b) Undistorted map Phase in X from Reference Sphere. . . . .	61
FIGURE 2.25. (a) Original map Phase in Y from Reference Sphere. (b) Undistorted map Phase in Y from Reference Sphere. . . . .	62
FIGURE 2.26. Reconstructed Sphere. . . . .	64
FIGURE 2.27. Sphere Mean Curvature and Cylinder power. . . . .	65
FIGURE 2.28. (a) Original map Phase in X from PAL under test. (b) Undistorted map Phase in X from PAL under test. . . . .	65
FIGURE 2.29. (a) Original map Phase in Y from PAL under test. (b) Undistorted map Phase in Y from PAL under test. . . . .	66
FIGURE 2.30. Reconstructed PAL surface. . . . .	66
FIGURE 2.31. Reconstructed PAL surface. . . . .	67
FIGURE 3.1. Lens-Eye model layout in OpticStudio Zemax design software. .	74
FIGURE 3.2. Lens-eye model used for point spread function calculation. The stop is at the center of rotation of the eye, 27 mm from the back vertex of the spectacle. The field of view is sampled with a Cartesian grid. . .	74
FIGURE 3.3. <i>psf</i> sampling for different object distances (a) Near Distance. (b) Intermediate Distance. (c) Far distance. . . . .	75
FIGURE 3.4. Subsections of basis functions . . . . .	78
FIGURE 3.5. Bilinear interpolation example. . . . .	79
FIGURE 3.6. Region 1 analysis. . . . .	80
FIGURE 3.7. Differences between <i>psf</i> found by interpolation and <i>psf</i> found using raytracing code. The <i>psf</i> compared is at the center of Region 1, $(x, y) = (-21, -15)$ . . . . .	80
FIGURE 3.8. Examples of different regions for far field, where the Point Spread Function differs in function of glaze angle. . . . .	83
FIGURE 3.9. Interpolated <i>psf</i> and the <i>psf</i> obtained with raytracing for Regions 2, 3 and 4. . . . .	84
FIGURE 3.10. Interpolated <i>psf</i> and the <i>psf</i> obtained with raytracing for Regions 5, 6 and 7. . . . .	85
FIGURE 3.11. Differences of extrapolation and <i>psf</i> obtained using Zemax. . .	86
FIGURE 3.12. Angular relation between pixel angular size and point spread function angular size. . . . .	87
FIGURE 3.13. Comparison of the interpolated psf based on the psf database and its down-sampled version created to match the angular subtense of pixels in the simulation scene. . . . .	88
FIGURE 3.14. Samsung gear 360 Camera. . . . .	90



LIST OF FIGURES—*Continued*

FIGURE 3.15. Example of scene with three object depths taken with the Samsung Gear 360 camera. . . . .	91
FIGURE 3.16. Example of a grid with positive main and edge distortion applied. . . . .	92
FIGURE 3.17. Example of a grid with negative main and edge distortion applied. . . . .	92
FIGURE 3.18. Example of undistorted scene using GIMP image manipulation software, with three object depths taken with the Samsung Gear 360 camera. . . . .	93
FIGURE 3.19. Cellphone picture taken at $d = 200mm$ from camera. . . . .	94
FIGURE 3.20. (a) Original Picture $FOV = 82^\circ$ , $N_x = 1296$ pixels (b) Cropped Picture $FOV = 60^\circ$ , $N_x' = 949$ pixels. . . . .	96
FIGURE 3.21. Examples of the cellphone at different depths. Everything relative assuming a field of view $FOV = 60^\circ$ equal at $N_x = 1296$ pixels. . . . .	97
FIGURE 3.22. Basis functions in Region 7, at three different object depths. . . . .	97
FIGURE 3.23. Simulation of the same object at different planes of the scene. . . . .	98
FIGURE 3.24. Masked images at different depth planes. . . . .	99
FIGURE 3.25. Color Object. . . . .	100
FIGURE 3.26. Object decomposed in three RGB channels. . . . .	101
FIGURE 3.27. Graphic representation of the first step of the algorithm applied. The $psf$ that corresponds to a determined pixel in the image is searched, if the $psf$ does not exist, interpolation is performed. . . . .	102
FIGURE 3.28. Graphic representation of the second step in the algorithm applied. The $psfs$ are weighted by the correspondent pixel value. . . . .	102
FIGURE 3.29. Graphic representation of the third step in the algorithm applied. Contribution of $psfs$ at each pixel are summed to get the final value for each pixel. . . . .	103
FIGURE 3.30. Simulation results for Far Field and Mid-Field. . . . .	104
FIGURE 3.31. Simulation results for different Near Field distances. . . . .	105
FIGURE 3.32. Comparison of Near Field visual performance. . . . .	105
FIGURE 3.33. Complete simulated 3 depths scene for Near field $d_1 = 200mm$ , $d_2 = 300mm$ and $d_3 = 400mm$ . . . . .	106
FIGURE 3.34. Complete simulated 3 depths scene for Near field $d_4 = 500mm$ and $d_5 = 660mm$ . . . . .	107

## LIST OF TABLES

TABLE 2.1.	Coefficient of the Zernike Standard Polynomial. . . . .	49
TABLE 2.2.	Distortion Coefficients. . . . .	60
TABLE 3.1.	Examples of regions to analyze. . . . .	81
TABLE A.1.	PAL 37 Zernike Coefficients. . . . .	112

## ABSTRACT

The condition in which the eye loses the ability to focus on near objects is called presbyopia. The use of Progressive Addition Lenses (PALs) is one alternative to treat this condition. PALs have a continuous change in power from the top of the lens to the bottom to avoid abrupt change in power. The increment of power in progressive addition lenses is accomplished by increasing the lens curvature from the upper part of the lens to the lower part of it. PALs consist of one freeform surface that provides this power change and the other surface is typically spherical (or aspheric) with its shape chosen to meet the wearers distance prescription.

Because of its application, progressive lenses should be prescribed, made and tested in a very short period of time. A variety of testing methods have been developed through the years. However, these tests are designed to test symmetric optical elements, or use additional optics that are very expensive. What is needed is a new technique that can overcome these difficulties in an economic and fast way. In this dissertation, several methods were implemented to test the freeform surface shape of a Progressive Addition Lens. Two different types of methods were used: contact methods such as the use of a linear profilometer, and a Coordinate Measurement Technique (CMM); non-contact methods such as the SCOTS Test by refraction, and ultraviolet (UV) deflectometry.

Besides surface shape, acceptance of progressive addition lenses must be studied. A methodology to characterize the visual performance of Progressive Addition Lenses is presented with scene simulation of how the wearer sees through the spectacle. Simulated images are obtained by calculating the point spread function through a lens-eye model in function of gaze angle. A modified superposition technique which interpolates the psfs for different gaze angles, as well as at different object distances is developed and used to create simulated images. Such scene simulations would allow patients to examine the variety of tradeoffs with the various treatment modalities and make a suitable choice for treatment.

## CHAPTER 1

## INTRODUCTION

**1.1 The Eye**

The eye is an amazingly sophisticated optical system. Despite the complexity of this very important structure, we rarely stop to think about the fitness and suitability of its design. We do not tend to focus on the deterioration of its performance with age until the errors create significant impact on our visual abilities. Consequently, this section focuses on the elements that comprise this organ, as well as looking at their performance with age and some of the creative appliances that have been created to mitigate this deleterious effects.

The main structure of the eye is a sphere approximately 24 mm in diameter, which is partially surrounded by three layers [5]. The first layer is the sclera, a flexible tissue that surrounds all the eyeball except for the cornea; this is the white part of the eye. Inside the sclera, there is the choroid, a thick layer, which serves as structural support for the retina. This last layer, the retina, is essentially a photosensitive sensor, which converts incoming light into electric signals that the ultimately brain interprets as images [6]. Figure 1.1 shows the basic anatomy of the human eye.

From an optical system perspective, following the light path of an object being viewed by the eye, the first optical element of the eye is the cornea. This is a positive lens that contributes about two-thirds of the power of the eye due to the high change in refractive index at its front surface. Following the cornea, there is a chamber which contains the aqueous humor, a watery fluid that supplies nutrients to the cornea. These two components constitute the anterior chamber of the eye. The next component that appears is the iris, which serves as the aperture stop of the system.

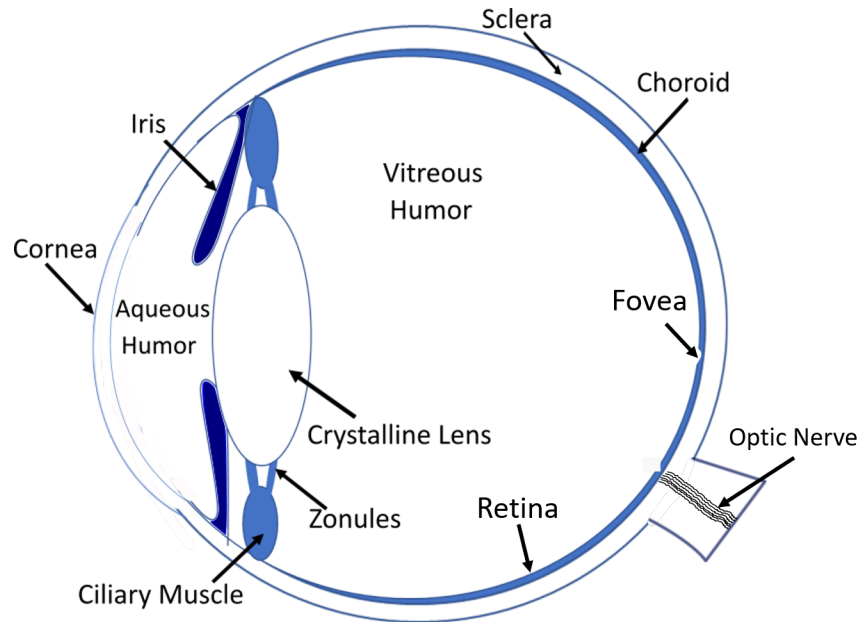


FIGURE 1.1. Eye anatomy.

Two muscles that by expanding and contracting control the pupils size, depending on the ambient environmental light. Normally, for a bright scene the pupil contracts to a minimum aperture of approximately 2 mm, and for a dark scene the pupil can expand to upwards of 8 mm in diameter.

For the purposes of this dissertation, the most important elements of this optical system are the crystalline lens, the zonules and the ciliary muscles. Unlike the cornea, the crystalline lens is a gradient refractive index lens with a variable power. The crystalline lens is surrounded by the ciliary muscles, which are a ring of muscles that are attached to edge of the crystalline lens by the zonules. The curvature, thickness and diameter of the crystalline lens are controlled by the expansion and contraction of the ciliary muscles. When the ciliary muscles relax, the zonules are pulled taught and the curvatures of the crystalline lens surfaces are reduced. When the ciliary muscles contract, the tension on the zonules is reduced and the surface curvatures of the crystalline lens increase. The curvature changes induced by flexing and relaxing

the ciliary muscles enable the crystalline lens to vary in power from about 20 diopters in the relaxed state to upwards of 34 diopters in the fully contracted state of the young eye.

Following the crystalline lens is the posterior chamber. The posterior chamber is filled with the vitreous humor, a jelly-like substance that provides support for the eye and maintains its round shape. Finally, the inner surface of the eye is lined with the retina. The retina consists of an array of photoreceptors that absorb incident photons and converts them to an electrical signal that is transmitted along nerve fibers along the optic nerve to the visual cortex in the brain. The brain ultimately interprets these signals and creates the images we perceive.

## 1.2 Presbyopia

The eye is a complex and amazing optical system. However, as with any other organ, it is vulnerable to the aging process and to different diseases. In this dissertation, we will discuss one special problem that all human beings have when they get older. Presbyopia is the condition in which the eye loses the ability to focus on near objects.

The function of the crystalline lens in the eye is to change its shape to focus at different object distances, changing the eye's refractive power. This action is called accommodation and happens when the ciliary muscle contracts or expands the tension on the zonules, allowing the crystalline lens to change focus from far to near vision.

Accommodation is measured clinically by taking an object and moving it closer to the subject until a blurry image is detected. Vergence is a measure of object distance given in units of diopters. The vergence of an object is the reciprocal of the distance (in meters) between the subject and the object being viewed. The accommodation amplitude, also measured in units of diopters, is simply the difference in object vergence between the nearest object the subject can view clearly and the farthest object that can be viewed clearly [7]. For example, reading distance is typically taken as

33cm, which corresponds to an object vergence of 3 diopters. A distant object can be considered to be infinitely far away, with an object vergence of 0 diopters. For a subject that can just clearly adjust focus between the distant object and the reading distance is said to have an amplitude of accommodation of 3 diopters.

With aging, a loss of accommodation amplitude appears. The eye can no longer change its power sufficiently to bring near object into focus on the retina. Now instead close objects are imaged behind the retina, leading to a blurry image such as the one shown in Figure 1.2 of a food label.

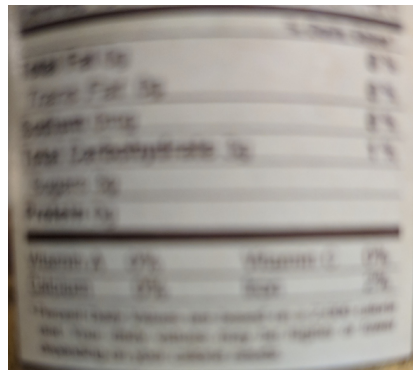


FIGURE 1.2. Example of a close object through a presbyopic eye.

This loss of accommodation is a normal condition called presbyopia (Greek for old eye). Although the exact age of occurrence depends on different conditions for every person, presbyopia usually starts to have significant impact on vision around the age of 40. Figure (1.3) shows a plot of the amplitude of accommodation as a function of age.

The young eye can typically accommodate 14 diopters. This range steadily decreases over the years, but is rarely noticeable to subjects younger than 40 since they can still comfortably read. However, after the age of 40, subjects typically start by needing to fully accommodate or maximally flex their ciliary muscles to bring near objects into focus. This exertion leads to eye strain. As the accommodative range

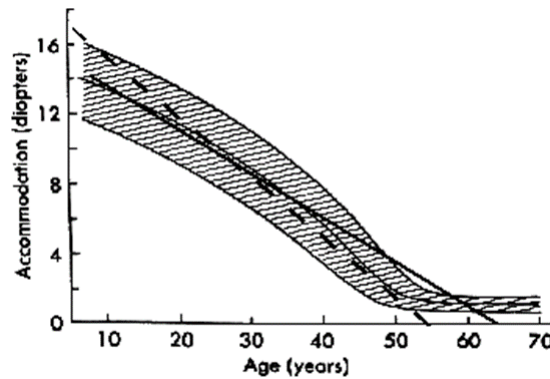


FIGURE 1.3. Amplitude of accommodation vs. age. Image reproduction from [1].

further reduces, subjects need to hold reading material further away to bring it into focus. Finally, an age is reached in which the accommodation and the length of the arms are insufficient to bring near objects into focus.

The loss of accommodation is an inevitable situation and the cause is not fully understood. There are different theories for the etiology of this condition [8]. Atchinson in Reference [8] summarizes these theories. There are two categories for these theories: lenticular theory, and extralenticular theory. The first theory is based on the idea that the crystalline lens loses the ability to change its shape, because the lens hardens with age. On the other hand, there is the extralenticular theory, in which the prevalent idea is that the ciliary muscle gets weak, or that the zonules loses elasticity with age. The crystalline lens continues to grow throughout the lifetime, adding layers of material to its outer region while compacting the material at its core. This has the effect of increasing its density and causing the lens to mechanically stiffen with age. Furthermore, the increased size of the crystalline lens leads to a reduction in the tension of the zonules so that they may not be able to exert the same forces on the periphery of the lens. Regardless of the reason, suffering from presbyopia is part of being human. A variety of treatments of different degrees of complexity and



invasiveness have been developed to deal with this condition.

## **1.3 Treatments**

In this section, some treatments to help alleviate the effects of presbyopia are briefly explained. These treatments can be classified into two groups. The first one consists in treatments that require surgery to replace the eye lens with an artificial one. On the other hand, the second class of treatments consist of therapies that involve the use of external appliances, such as contact lenses, reading glasses, bifocals and progressive addition lenses.

### **1.3.1 Intraocular Lenses**

Cataracts are another common ailment of the crystalline lens that occurs with age. Cataracts are the gradual clouding of the crystalline lens and is due to a lifetime of absorption of ultraviolet light, which causes a breakdown in the proteins the compose the crystalline lens material. The clouding of the lens causes increased scatter and stray light in the eye and a reduction in vision. Typically, intraocular lenses (IOLs) are used in cataract surgery [9]) where the cloudy lens is removed and replaced with an artificial lens. The onset of cataracts usually lags behind presbyopia by several decades, so treating presbyopia with IOLs is typically considered an elective surgery that is not covered by medical insurance. Even with this drawback, Clear Lens Extraction procedures are becoming more prevalent where the non-cataractous but presbyopic lens is removed and replaced with an IOL. Conventional IOLs have a single power and consequently only provide the recipient with a fixed focal distance. To treat presbyopia with IOLs, multifocal lenses are required which provide two or more powers within the same lens platform to create multiple object distances that are conjugate to the retina. Extensive research and resources are being put into developing accommodating IOLs which change power in response to contraction of

the ciliary muscle. While progress has been made on a truly accommodating IOL, this technology is still on the horizon.

There are many types of multifocal intraocular lenses that can be used to compensate for the eye's loss of accommodation. Among them are refractive multifocal lenses, diffractive multifocal lenses and accommodative lenses. An extensive review of the commercially available intraocular lenses can be found in Reference [10]. Refractive multifocal lenses were the original choice for multifocal lenses. They consisted of multiple regions within the lens aperture that contained different refractive powers. A common configuration for refractive multifocal lenses is a series of annular zones of alternating high and low power. Light passing through the low power regions from distance objects is focused to the retina, whereas light from near objects passing through the high power regions also focuses on the retina. In this manner, the lens acts as a bifocal. However, since these lenses are located within the eye, both optical regions are simultaneously active. This means that in addition to the foci described above, there is also extraneous light where light from the distant object passes through the high power regions and light from the near object passes through the near region creating out-of-focus images on the retina. Consequently, in-focus and out-of-focus images are projected onto the retina simultaneously. This effect is called Simultaneous Vision and has the effect of reducing the contrast of the in-focus image. Refractive multifocal lenses have been largely abandoned these days and have been replaced with diffractive multifocal lenses because diffractive multifocal lenses tend to have less issues with the out-of-focus components. Diffractive multifocal lenses are the polar analog of a diffraction grating. A binary diffraction grating disperses light into a multitude of diffraction orders. Each order has a diffraction efficiency which describes the amount of energy going into each order. The angle of the diffraction order is dependent upon the grating period. The diffraction efficiency can also be tailored into specific orders by blazing the diffraction grating and changing its step height. For a multifocal diffractive IOL, the grating is now in polar form where the

grating period follows the Fresnel zones of the lens. Blazing the diffractive zones and adjusting the step height of the blaze can concentrate most of the energy into two diffraction orders leading to a bifocal lens. In Figure 1.4, an example of an apodized bifocal diffractive IOL, marketed by Alcon is shown. The steps following the Fresnel zones of the lens are evident in the central portion of the lens. The term apodized here has a slightly different meaning than what is familiar in optical engineering. Here, apodized means that the step heights of the diffractive zones gradually reduce towards the periphery of the lens. This allows the diffractive lens blend seamlessly into a refractive lens in the periphery which helps mitigate some of the side effects of simultaneous vision.



FIGURE 1.4. AcriSof IQ ReSTOR multifocal IOL [2].

Diffractive multifocal IOLs still have some side effects to be considered. For example, at night halos and diffraction rings can appear around lights. These lenses are far from perfect, but represent an improvement over refractive multifocal IOLs.

To fully eliminate the bad effects of simultaneous vision, a truly accommodating IOL is needed. Accommodating IOLs have been pursued which modify the power of the eye by either moving axially within the eye or by changing their surface curvatures in response to constriction of the ciliary muscles. However, reliable accommodating IOLs have not reached the market yet and remain an unsolved challenge in treating presbyopia.

Regardless of the form of the multifocal IOL, this route for treating presbyopia is highly invasive since it requires surgery and is expensive. There are less expensive and easily reversible options available.

### **1.3.2 Contact Lenses**

The use of multifocal contact lenses is another option to treat presbyopia. There are several treatments that use this ophthalmic device in different ways to achieve the same goal. Indubitably, all of them have present their own advantages and disadvantages.

One of the presbyopic contact lens correction techniques is monovision. This treatment consists of the patient wearing a contact lens in one eye to correct for near distance and wearing a distance correcting contact lens in the other eye. Simultaneous vision in this case takes a slightly different form, where one eye has a sharp image from near objects and blurry images from distant objects and vice versa in the fellow eye. This treatment modality can work because the brain tends to suppress the blur caused by one eye [11]. However, similar complaints of glare and halos occur with monovision as with that of the multifocal IOLs described above. Furthermore, monovision tends to impede depth perception since the two eyes are focused differently.

The use of bifocal and multifocal contact lenses is another option to be considered. Historically, bifocal contact lenses operate in much the same manner as the refractive multifocal IOLs described above. The contact lens consists of different regions

containing different powers to achieve simultaneous vision. Diffractive multifocal contact lenses have been largely avoided for comfort reasons. The discrete steps of the diffractive lens tend to irritate the corneal surface or the eyelid depending upon which surface the diffractive pattern is placed. The modern form of multifocal contact lenses is typically an aspheric lens with a smooth change in radius of curvature towards its periphery, changing the power progressively at different radial regions. In effect these aspheric lenses introduce high spherical aberration to extend the depth of focus of the lens [12]. The drawback of this spherical aberration, of course, is a reduction in image quality and contrast associated with an aberrated system. Figure 1.5 shows an example of an aspheric progressive multifocal contact lens.

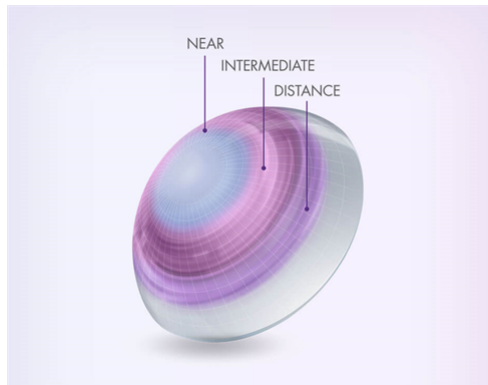


FIGURE 1.5. Alcon Multifocal Contact Lenses [3].

Simulations of images, as they are seen in different multifocal contact and IOLS has already been done in the Laboratory of Visual and Ophthalmic Optics of the University of Arizona [13]. A portion of this dissertation is devoted to extending these techniques to the spectacle lens-based presbyopia treatments describe in more detail below.

### 1.3.3 Reading Glasses and Bifocal Spectacles

Loss of accommodation translates into difficulty in focusing on close objects. To treat presbyopia at least two types of prescriptions are needed: a far distance correction and a near distance correction (reading section). This is why the easiest and most common solution to treating presbyopia is the use of reading glasses. These are spectacles that are only worn when reading close objects. A second pair of glasses may be required to see distant objects if the person additionally suffers from refractive error. The difficulty associated with reading glasses is that it cannot be worn all the times. The wearer has to put on reading glasses for near tasks and then remove them (or replace them with another pair of glasses) to perform distance tasks. In addition, situations where rapid switching between near and far objects become awkward at best, such as the situation of driving and then looking at the dashboard.

Bifocal spectacles help to solve this problem by having two different prescriptions in the same spectacle frame. The first bifocals are attributed to Benjamin Franklin, who cut two spectacle lenses with different prescriptions in half and put one half of one, and other from the other into a frame. However, although both regions had good optical quality, the separation is annoying to the wearer. Although their design has been improving with time, one of the problems is the abrupt change in power between these two regions, and the distraction of the visible line between them [14]. The power change causes an abrupt increase in magnification for objects appearing in the lower (near vision) region of the lenses. This magnification change can cause issues with tasks such as walking down stairs. There are also cosmetic considerations associated with bifocal spectacles as many people feel old when their glasses have the telltale line across them.

The abrupt change in power between regions is shown in Figure 1.6.

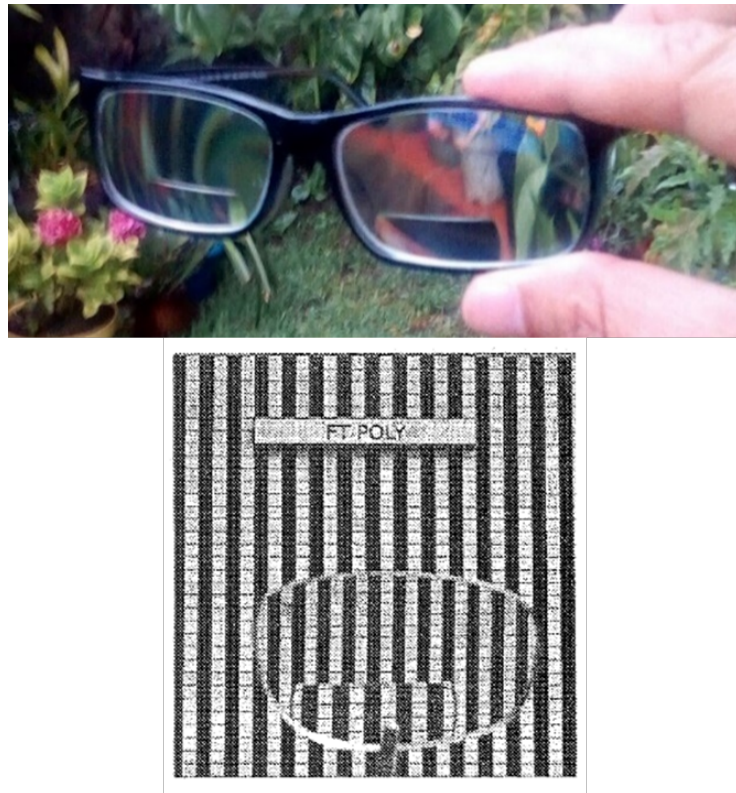


FIGURE 1.6. Bifocal Spectacles. Visible change in power between distance and near region. The lower image shows the abrupt change in magnification (from [4])

#### 1.3.4 Progressive Addition Lenses Design

As mentioned above, one of the problems of bifocal spectacles is the abrupt change in power/magnification that occurs when transitioning from the distance region to the near region of the lens. The use of Progressive Addition Lenses (PALs) is another alternative to treat presbyopia. PALs are multifocal vision spectacles that have change in power without the discontinuity associated with bifocal lenses. PALs have a continuous change in power from the top of the lens to the bottom to avoid the abrupt change in power. To see different object distances, eye rotation is needed. The eye rotates to the point where the PAL provides the correct power to bring the

object of regard into focus. One tradeoff of PALs though is the presence of unwanted astigmatism in the lower periphery of the lens, which can cause visual discomfort to the wearer.

The increment of power in progressive addition lenses is accomplished by increasing the lens curvature from the upper part of the lens to the lower part of it. PALs typically consist of one freeform surface that provides this power change and the other surface is typically spherical (or aspheric) with its shape chosen to meet the wearers distance prescription. To create a smooth and continuous freeform surface, the lateral regions of the lower portion of the lens necessarily have shapes that introduce unwanted astigmatism [15].

In general terms, as shown in Figure 1.7, the structure of Progressive Addition Lenses consists in four zones:

1. Distance Zone.
2. Intermediate Zone or Progressive Corridor.
3. Near or Reading Zone.
4. Blending Region.

The intermediate zone, also called progressive corridor, is the transition where the power increases gradually from the distance prescription to the highest power of the lens in the near region. The length and width of the corridor is determined by the design of the PAL and it follows the Minkwitz theorem described below.

The near zone, at the lower part of the lens, is the region with the highest spherical power. Because of the linear relation between spherical power and curvature, this zone is the steepest one. As mentioned before, to join this region with the distance zone without visible discontinuities, the freeform surface must gradually change shape from the distance curvature to the near curvature. In doing so, the side effect is that the areas on either side of the progressive corridor and the near zone have large levels of surface astigmatism leading to poor visual performance when viewing through these



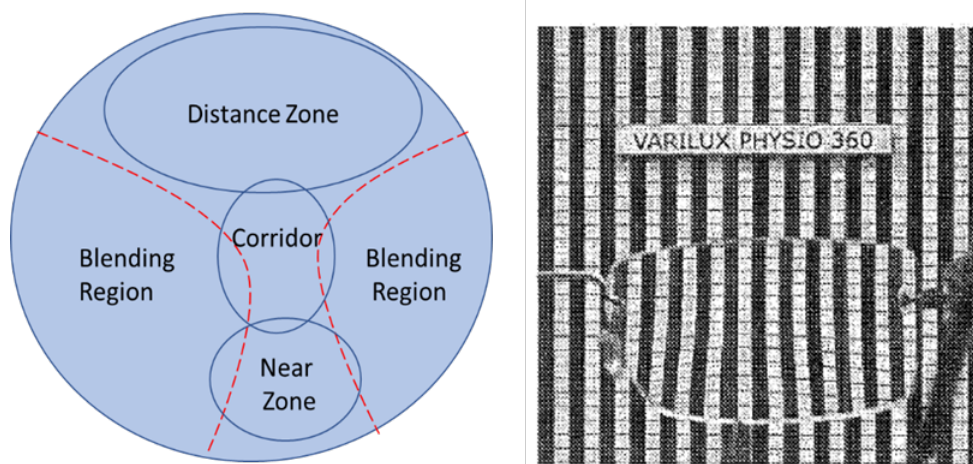


FIGURE 1.7. Zones of a Progressive Addition Lens. The right image shows the smooth transition in magnification from the distance region to the near region. (from [4])

areas. These zones without good visual quality are called blending regions.

The organization of the various power zones of the PAL require the wearer to adapt new eye rotation and head alignment strategies for viewing objects at different distances. When viewing distant objects through the upper portion of the lens, the wearer can typically scan their eyes across the horizontal field. However, when viewing intermediate objects such as a computer screen, the progressive corridor is narrow and the whole width of the computer screen will not be sharp if the eye scans along the horizontal field. Instead, the wearer tends to align their eyes in the progressive corridor and uses their head to scan back and forth to keep the ideal portion of the intermediate power zone in line with their line of sight. Although the near region is slightly wider than the progressive corridor, a similar head scanning requirement is needed for near objects.

An important concept of progressive addition lenses is the umbilical line. Along this line spherical power increases towards the lower part of the lens. The local surface curvature along the umbilical line is the same in the two principal directions, meaning

zero astigmatism is introduced along its path. However, the surface astigmatism increases when moving away from the umbilical line. The Minkwitz Theorem is a description of how the astigmatism changes when moving away from the umbilical line and it is important for understanding different designs of Progressive Addition Lenses.

The Minkwitz theorem states that the amount of change in cylinder power ( $\Delta cyl$ ) in a region near the umbilical line, is approximately twice the change in spherical power added ( $\Delta Add$ ) along this line.

$$\Delta cyl \approx 2 \Delta Add. \quad (1.3.1)$$

This theorem opens the discussion about two different design philosophies of Progressive Addition Lenses: hard design and soft design.

Hard design PALs have a short progressive corridor, permitting rapid access to different zones with eye rotation. In these designs, the distance and near vision areas are wider. However, following the Minkwitz theorem, when a rapid change in spherical power add occurs, there is a rapid increase in astigmatism on either side of the progressive corridor and therefore high intensity aberration in the blending regions. Because the big amount of peripheral distortion and astigmatism, the adaptation period is more difficult.

On the other hand, in soft design PALs, the spherical power change from the distance to near region is spread over a long distance. This leads to a progressive corridor that is wider and larger. Thus, there is less distortion at the peripheral view. One disadvantage compared to the hard design is that the areas at distance and near vision zones are narrower. These soft designs are good for new presbyopes, because the gradual change in unwanted astigmatism provides an easier period of adaptation.

Progressive addition lenses are a good option when looking for continuous vision from far to near distance. Despite the disadvantages mentioned above, new techniques

are emerging in the fabrication field, allowing custom freeform surfaces to compensate wearer needs. Nowadays, each design is customized to fit the frame and patient prescription [16]-[17], therefore new techniques of surface verification are needed.

## 1.4 Motivation

As a consequence of the variety of solutions to treat presbyopia and the advantages and disadvantages of these treatments, the patient who suffers from this condition has to make an informed decision of what method will fit their needs.

With the technological advances in fabrication, such as freeform surfacing, the design of PALs can be customized for different patients. Nonetheless, surface characterization is as important as the fabrication process. Due to the application of progressive addition lenses, they should be tested in a very short period of time. For this reason, in the first part of this dissertation different techniques of freeform metrology are presented.

Besides surface shape, acceptance of progressive addition lenses must be studied. This is a subjective measurement, and usually two types of studies are applied: wearer trial and preference trial. In the first one, the wearer uses one model for several days and then evaluates its performance. For the second one, the preference trial, subjects are given two different models and then they decide which one they prefer [18]. Such studies are time consuming and expensive. Furthermore, it is difficult to provide the wide range of lens forms that are available.

In the second part of this dissertation, a methodology to characterize the visual performance of Progressive Addition Lenses is presented. Scene simulation of how the wearer see through the spectacle is obtained by calculating the point spread function through a lens-eye model in function of gaze angle. Such scene simulations would allow patients to examine the variety of tradeoffs with the various treatment modalities and make a suitable choice for treatment, or at the very least narrow the

list of choices prior to dispensing.

Characterizing the shape of the surface constitutes a challenge because of the difficulty of testing these freeform surfaces due to their large departure from a spherical shape. For the same reason, the PSF that defines the lens is highly shift variant, so a simple convolution of the PSF and the scene is not enough to create a simulated scene.

In this dissertation, four different methods to test the freeform surface are explained. After characterization of the surface form, a modified superposition technique which interpolates the PSFs for different gaze angles, as well as at different object distances is developed and used to create simulated images that the patient can use to decide if progressive lenses are the right option.

## CHAPTER 2

# METROLOGY OF PROGRESSIVE ADDITION LENSES

Optical design theory and raytracing tools provide a powerful platform to design and simulate optical components. Increased computational power has led to ease of design of wildly aspheric and freeform surfaces. However, there remains a non-trivial path from design to fabrication and testing of these surfaces. Accurate measurements of an optical surface, defined as metrology, is an important step in building a high-performance optical system. The surface form can only achieve what can be measured and limitations on metrology makes the fabricator blind to the source of errors in an assembled system.

Because of the characteristics of the surface to achieve a continuity of different optical powers through the lens, there are several fabrication techniques for Progressive Addition Lenses. The original PALs were created using slumping glass process. This process consists on heating an initial piece of glass on a ceramic slumping block initially created with the freeform surface shape, the goal is to obtain glass molds to use them for the production of plastic lenses. However, because heat is involved in the process, material properties of the glass and ceramic have to be taken into account to design the shape of the ceramic slumping block. To overcome these problems, numerical modelling is used for designing the surface [19].

Nowadays, diamond turning machining is employed to fabricate PALs, usually tool servo is used. Fast tool servo (FTS) and slow tool servo (STS) can manufacture the surface of non-rotation symmetry by controlling the position of the cutting tool with high accuracy [20]. One example of fabrication of PALs using FTS is found in reference [21]. The FTS uses a voice coil actuator to drive the cutting tool. The

process to fabricate the progressive addition lens consists in use a sphere as base and cut it to achieve the freeform surface. Two diamond tools are used, the first one for rough cutting and the second one for finish the cutting. After finishing, the surface has to be polished to remove the marks.

Interferometric tests are very powerful techniques to detect phase change between the reference beam and the tested beam. However, because of the non-symmetric nature of Progressive Addition Lenses (PALs), interferometric testing of these lenses needs more complex configurations and more expensive optical elements. PALs typically are meniscus lenses. The freeform surface of the PAL can appear on either the concave or convex surface. Furthermore, the surfaces of PALs are fast. In general, fast convex surfaces are difficult to test interferometrically even if they are spherical since they require a fast transmission sphere and a large aperture to ensure coverage of the surface. Front surface PALs add an extra degree of complexity with the steep aspheric departure from a best fit sphere. Computer-Generated Hologram to compensate the wavefront of freeform surfaces under test are often used to test aspheric and freeform optics [22]. CGHs can be expensive and each PAL design would require a unique CGH. There are also alignment challenges with CGHs that limit the throughput of testing these surfaces in a manufacturing environment. Without a CGH, it is difficult or impossible to get the surface shape from interference patterns, as demonstrated in Figure 2.1 due to the aliasing that occurs. This aliasing observed in the interferogram happens because the freeform surface departs from the spherical reference surface used, leading to errors in the results. Therefore, reliable measurement of custom PAL profiles for various presbyopic prescriptions is an important challenge to overcome using traditional metrology techniques.

The interference pattern shown in Figure 2.1, is from a KODAK Progressive Addition Lens. The freeform surface is on the convex side of the lens. The nominal radius of curvature of this surface is  $R = 83.728mm$  and the diameter of the lens is  $D_{lens} = 80mm$ . The labeled add power of the lens is 1.00 to 3.00 in 0.25 Diopter

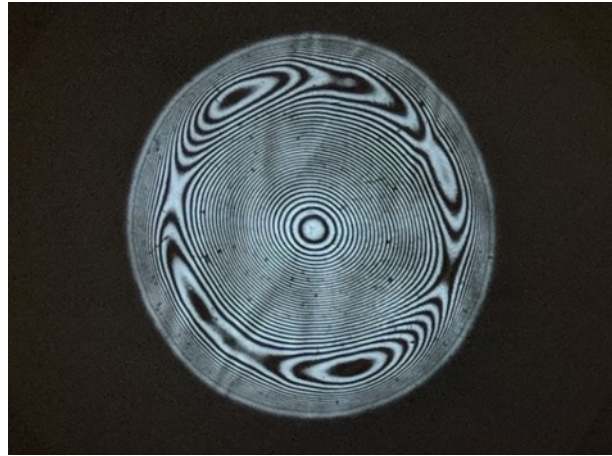


FIGURE 2.1. Interferogram of the Progressive Addition Lens under test, using ZYGO interferometer with a reference sphere F/1.5.

steps. This lens is used throughout the dissertation for analysis and measured by different techniques.

Because of its application, these spectacles have to be fabricated and tested in a very fast way. To decrease the price and testing time, several techniques to test Progressive Addition Lenses were studied, such as using a lateral shear interferometer to measure power variation as it is demonstrated in Reference [23], in this technique the PAL under test is placed in such a way that the light after the lens is collimated. The light is reflected by the front surface and the surface back of a plane parallel plate of glass the beams are sheared a distance  $s$ . The beams are not perfectly collimated and therefore interference fringes appear. The principle here is that the space between fringes is inversely proportional to the local power of the lens. Another approach to characterized Progressive Addition Lenses is test them with a modified Hartmann test. In this case, the plate with holes is replaced with a circular scanning laser beam, simulating the eye looking at different directions of the lens. One positive sensitive detector recovered the light spot after the lens. This light spot is analyzed and is expressed in Fourier series to recover the spherical power, and astigmatism at

different angles [24].

In this dissertation, several methods were implemented to test the freeform surface shape of a Progressive Addition Lens. Two different types of methods were used: contact methods such as the use of a linear profilometer, and a Coordinate Measurement Technique (CMM); non-contact methods such as the SCOTS Test by refraction, and ultraviolet (UV) deflectometry.

## 2.1 Profilometer

The mathematical description of the freeform surface from the Kodak Progressive Addition lens is unknown. In general, manufacturers keep the progressive surface design proprietary. There is limited information regarding designs available in the academic and patent literature. At best some patents will provide a sag table of the surface that can be fit and analyzed, but these are not widely available and tend to be the same design across multiple patents. Since the ideal shape of the Kodak lens used here is lacking, a reference or gold standard with which to compare is needed. We found this reference by using a linear profilometer available in the Visual and Ophthalmic Optics Laboratory. However, one trade-off of this instrument is that it is a contact profilometer. This means that the tip makes physical contact with the piece under test. Although contact force between the tip and the surface can be controlled, material and mechanical properties of the surface under test must be considered to avoid the risk of damaging the part.

### 2.1.1 Profilometer Specifications

The instrument used to measure the freeform surface from the Progressive Addition lens was a linear profilometer MarSurf XC 2 with CD 120 drive unit, (Mahr Federal, Providence, RI). This measuring station is a contact profilometer with two probe arms of length  $175\text{mm}$ , and  $350\text{mm}$ . The tip radius of the probe arms is  $25\mu\text{m}$ .



This instrument works on a traversing length in  $X$  of  $0.2mm$  to  $120mm$  ( $0.0079in \times 4.72in$ ). The measuring range in  $Z$  is  $50mm$ .

The resolution in  $Z$  depends on the stylus tip used. For the  $350mm$  probe arm the resolution is  $20.38\mu m$ . Meanwhile for the  $175mm$  probe arm it has a resolution of  $0.19mm$ . The resolution in  $Z$ , relative to the measuring system is  $0.04\mu m$ . The contact measuring force range is  $1mN$  to  $120mN$ . The PAL is mounted on an  $x - y$  stage. The probe arm is dragged across the surface to measure its sag.

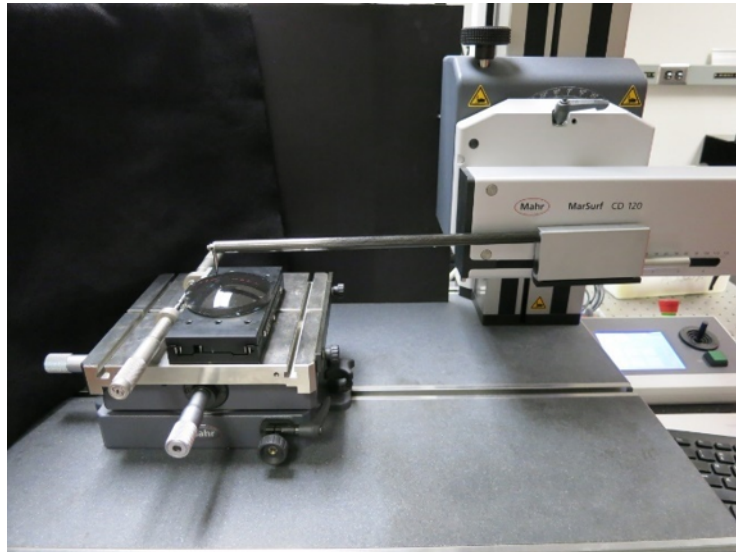


FIGURE 2.2. MarSurf CD 120 Linear Profilometer.

### 2.1.2 Data Collection

It is traditionally assumed that the piece under test is rotationally symmetrical and the profilometer is used to measure one profile with high accuracy. Nonetheless, in the case of testing freeform optics, one profile is not enough to get the full description of the surface. Therefore, multiple scans must be performed.

To perform the measurements, the tip used had dimensions of  $350 \times 33mm$  due

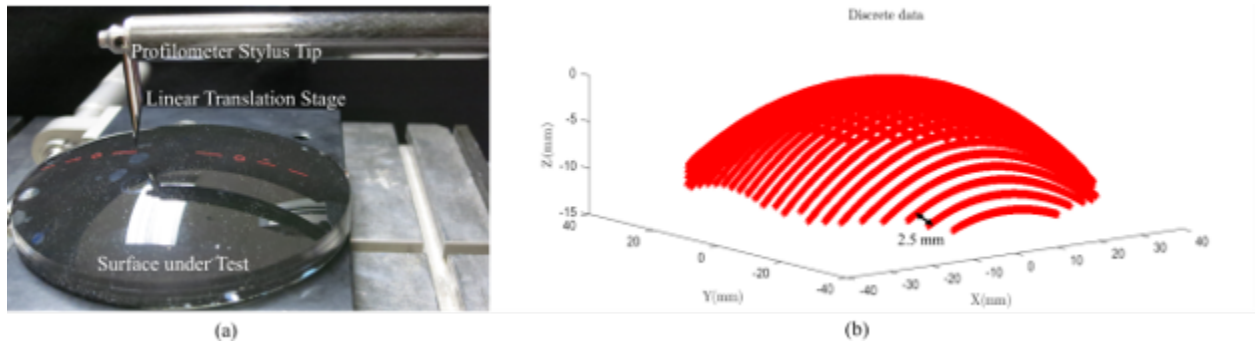


FIGURE 2.3. (a) Progressive Addition Lens under test mounted on a linear stage. (b) Discrete data obtained from the Profilometer after 31 profile measurements, the origin is at the center of the lens.

to the size of the lens and the smoothness surface. The PAL is mounted on a linear stage and laterally translated between scans. We performed 31 profiles along the  $X$  axis, translating the lens every  $2.5\text{mm}$  along the  $Y$  axis. The scans started at one side of the lens and the stage was driven in the same direction for subsequent scans. This technique helps to reduce errors occurring from backlash in the stage.

The data obtained from the profilometer is in the coordinate system of the instrument. To fit the data, all the points were translated to a coordinate system where the origin is at the center of the lens. Following translation, the data are masked into a circle of radius  $r = 37.5\text{mm}$ .

### 2.1.3 Fitting Data

Due to the circular shape of an optical element, one set of functions usually used in the optics field is the Zernike polynomials. These have very convenient mathematical properties over the unit circle. They are orthogonal have continuous derivatives, are related to aberrations and depending on the number of terms can described very complex shapes [25].

The surface shape can be represented as a linear combination of Zernike polyno-

mials, given by

$$z(\rho, \theta) = \sum_{n,m} a_{n,m} Z_n^m(\rho, \theta), \quad (2.1.1)$$

where the definition of the Zernike polynomials is

$$Z_n^m = \begin{cases} N_n^m R_n^{|m|}(\rho) \cos m\theta & \text{for } m \geq 0, \\ -N_n^m R_n^{|m|}(\rho) \sin m\theta & \text{for } m < 0, \end{cases} \quad (2.1.2)$$

where the index  $n$  is the radial order and defines the maximum polynomial order of  $R_n^{|m|}$ . The azimuthal frequency is indicated by the index  $m$ , an integer that must satisfy  $|m| \leq n$ . The normalization constant  $N_n^m$  is defined by

$$N_n^m = \sqrt{\frac{2n+2}{1+\delta_{m0}}}. \quad (2.1.3)$$

The radials polynomials are given by

$$R_n^{|m|}(\rho) = \sum_{s=0}^{(n-|m|)/2} \frac{(-1)^2(n-s)!}{s! \left[ \frac{n+|m|}{2} - s \right]! \left[ \frac{n-|m|}{2} - s \right]!}. \quad (2.1.4)$$

In the case of using sampled data, the orthogonality property of the Zernike polynomials on the unit circle is no longer valid. However, if the data is well sampled over a circle, the coefficients of the expansion can be found using a least-square method as it is described in Reference [25].

Assume the matrix operation

$$\mathbf{Ax} = \mathbf{b}, \quad (2.1.5)$$

where  $\mathbf{b}$  is a column vector with the measured data from the profilometer  $z(\rho_i, \theta_i)$ , with  $N$  the number of sample points.

$$\mathbf{b} = [z(\rho_1, \theta_1) \ z(\rho_2, \theta_2) \ z(\rho_3, \theta_3) \ \dots \ z(\rho_N, \theta_N)]^T. \quad (2.1.6)$$

The matrix  $\mathbf{A}$  is defined by

$$\mathbf{A} = \begin{pmatrix} Z_0^0(\rho_1, \theta_1) & Z_1^{-1}(\rho_1, \theta_1) & Z_1^1(\rho_1, \theta_1) & \dots & Z_{n_{max}}^{n_{max}}(\rho_1, \theta_1) \\ Z_0^0(\rho_2, \theta_2) & Z_1^{-1}(\rho_2, \theta_2) & Z_1^1(\rho_2, \theta_2) & \dots & Z_{n_{max}}^{n_{max}}(\rho_2, \theta_2) \\ \vdots & \vdots & \vdots & \vdots & \vdots \\ \vdots & \vdots & \vdots & \vdots & \vdots \\ Z_0^0(\rho_N, \theta_N) & Z_1^{-1}(\rho_N, \theta_N) & Z_1^1(\rho_N, \theta_N) & \dots & Z_{n_{max}}^{n_{max}}(\rho_N, \theta_N) \end{pmatrix}. \quad (2.1.7)$$

Each column corresponds to a different Zernike polynomial and it has  $j + 1$  number of columns, where  $j$  is given by

$$j = \frac{n(n+2) + m}{2}. \quad (2.1.8)$$

Each row corresponds to the Zernike polynomial evaluated at each point  $(\rho_i, \theta_i)$  and it has  $N$  number of rows. The unknown that we want to determine is the column vector  $\mathbf{x}$  that has  $j + 1$  elements and it contains the expansion coefficients that represent the measured data as a linear expansion.

$$\mathbf{x} = (a_{0,0} \ a_{1,-1} \ a_{1,1} \ \dots \ a_{n_{max}, n_{max}})^T. \quad (2.1.9)$$

To solve for  $\mathbf{x}$  in Equation 2.5.4 we assumed that the matrix  $\mathbf{A}$  has many more rows than columns  $N \gg j + 1$ . In this case, both sides of the equation is multiplied by  $\mathbf{A}^T$

$$\mathbf{A}^T \mathbf{A} \mathbf{x} = \mathbf{A}^T \mathbf{b}. \quad (2.1.10)$$

Now, solving for  $\mathbf{x}$  multiplying both sides of the equation by the inverse of the matrix  $\mathbf{A}^T \mathbf{A}$  we get

$$\mathbf{x} = [\mathbf{A}^T \mathbf{A}]^{-1} \mathbf{A}^T \mathbf{b}. \quad (2.1.11)$$

The column vector  $\mathbf{x}$  will give us the Zernike expansion coefficients of the fitted data.

#### 2.1.4 Profilometer Results

The 2D set of discrete measurement points is fitted to a set of Zernike polynomials using the method described by [25]. The data obtained from the profilometer are in Cartesian coordinates  $(x, y)$  and are transformed to spherical coordinates  $(\rho, \theta)$  due to the nature of Zernike polynomials. Surface maps of the fits are shown in Figure 2.4 for two different numbers of expansion terms.

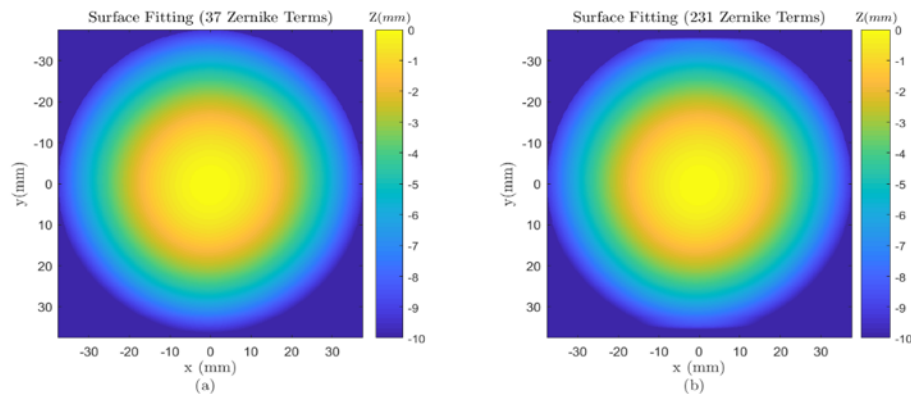


FIGURE 2.4. Freeform Surface from Profilometer data of a Kodak Progressive Spectacle Lens. (a) 37 Zernike Terms. (b) 231 Zernike Terms.

By subtracting the low order Zernike terms, of the residual surface height is revealed to understand how the radius of curvature varies to get different optical power.

In Figure 2.5 the freeform surfaces with 4 Zernike terms removed are shown. The terms removed are the first Zernike terms, piston, tilt x, tilt y, and power or defocus. This allows to see the asymmetric nature of the PAL.

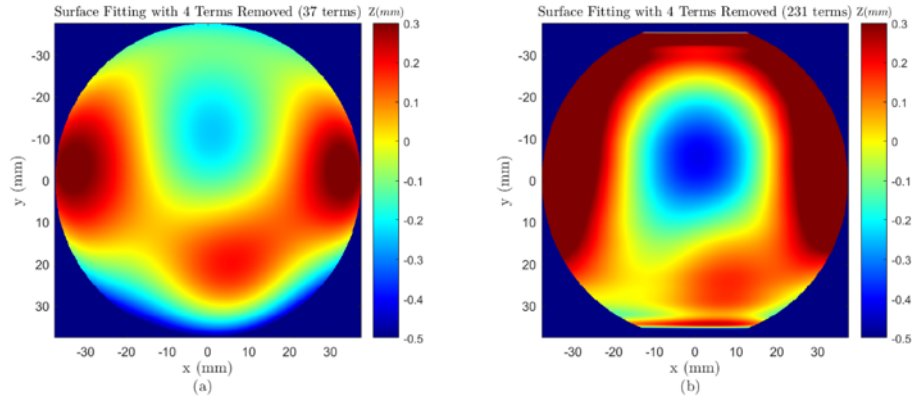


FIGURE 2.5. Freeform Surface from Profilometer data with low terms removed. (a) 37 Zernike Terms. (b) 231 Zernike Terms.

Although the surfaces look similar. When we analyzed the fitted surfaces with the original data obtained from the profilometer. We found important differences, as is shown in Figure 2.6. Analyzing the differences, we found a  $RMS$  value for 37 Zernike terms of  $RMS = 0.16\mu mm$ . In the case of the 231 terms, we found a  $RMS$  value of  $RMS = 6.79\mu m$ . This is because at the edge of the lens, the fitting is not well behaved.

As shown in Figure 2.6, the profilometer lines are present in the residual data. The source of these errors is likely backlash, and straightness and flatness errors in the translation stage. The fitting coefficients are shown in Appendix A.

The properties of PAL surfaces are typically illustrated with maps of the average local surface power and local surface astigmatism. To analyze the local curvature of the freeform surface, differential geometry and the "Fundamental Forms" are used. These expressions allow a pair of principal curvatures to be computed. The principal curvatures are the steepest curvature and flattest curvature at a given point on the

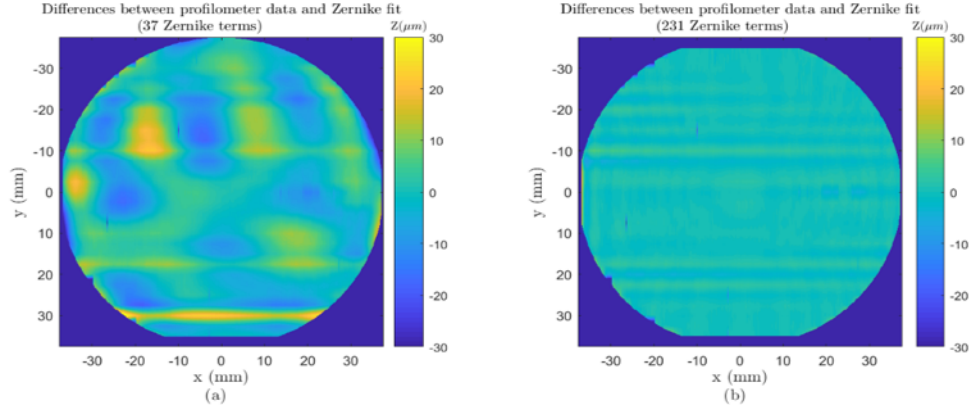


FIGURE 2.6. Differences in micrometers from Profilometer Data and FiSurface Fitting. (a) 37 Zernike Terms (b) 231 Zernike Terms.

surface. The principal curvatures are always orthogonal to one another. The mean curvature at a given point is calculated as the average of the principal curvatures. The different between the steep curvature and the flat curvature is used to determine the surface astigmatism. In Cartesian coordinates, the Fundamental Forms are given by

- First Fundamental Form

$$E = 1 + \left(\frac{\partial f}{\partial x}\right)^2 \quad F = \left(\frac{\partial f}{\partial x}\right) \left(\frac{\partial f}{\partial y}\right) \quad G = 1 + \left(\frac{\partial f}{\partial y}\right)^2$$

- Second Fundamental Form

$$L = \frac{\partial^2 f / \partial^2 x}{(EG - F^2)^{1/2}} \quad M = \frac{\partial^2 f / \partial x \partial y}{(EG - F^2)^{1/2}} \quad N = \frac{\partial^2 f / \partial^2 y}{(EG - F^2)^{1/2}}$$

where  $f$  is a two dimensional function describing the surface sag. Based on the Fundamental Forms, the mean curvature  $H$  can be computed, where

$$H = \frac{EN + GL + 2FM}{2(EG - F^2)} = \frac{1}{2}(\kappa_1 + \kappa_2). \quad (2.1.12)$$

The spherical power of the surface is related to the mean curvature by the following Equation

$$\phi = (n' - n)C = \frac{(n' - n)}{R}. \quad (2.1.13)$$

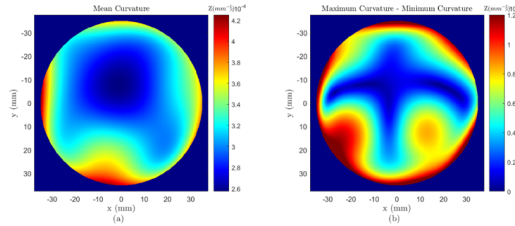


FIGURE 2.7. Mean Curvature of Zernike Fit calculated using the Fundamental Forms. (a) Local Spherical (b) Local Cylinder.

However, the Power map for the spectacle lens is calculated by adding the back surface power of the PAL. Here, the back surface power is assumed to be constant (i.e. the back surface is a sphere) and that the PAL is a thin lens meaning that the surface powers simply add to give the total power.

The mean curvature for the surface fitting is shown in Figure 2.7(a). The lowest curvature (blue region) of the lens is at the center part, and the curvature increases progressively to the bottom part of the lens. From Equation 2.1.13, optical power has a linear dependence on curvature, then the higher power is at the reading section.

The Gaussian curvature is calculated from the Fundamental Forms as

$$K = \frac{LN - M^2}{EG - F^2} = \kappa_1 \kappa_2. \quad (2.1.14)$$

Every point in a continuous surface  $z = f(x, y)$  has two principal curvatures  $\kappa_1$  and  $\kappa_2$ , minimum and maximum curvature through this point.



$$\kappa_1 = H + \text{sqr}t(H^2 - K), \quad (2.1.15)$$

$$\kappa_2 = H - \text{sqr}t(H^2 - K). \quad (2.1.16)$$

The difference between the maximum principal curvature and the minimum principal curvature is related to the local cylinder power. A map of this difference is shown in Figure 2.7(b). As expected at the center and along the progressive corridor, the surface has low astigmatism. Meanwhile, at the lower lateral edges corresponding to the blend regions, the surface astigmatism is markedly increased. This cylinder power introduces astigmatism to wearers of progressive addition lenses when viewing objects through these portions of the lens.

From the analysis described in this section, the surface described by 37 Zernike expansion terms is used as the reference when compared to other modalities for measuring this freeform surface.

## 2.2 Coordinate Measuring Machine

In 1959, the first appearance of the Coordinate Measuring Machine (CMM) was at the International Machine Tool exhibition in Paris. Ferranti, a British company, developed the CMM to overcome the challenges of measuring precision components [26]. Through the years, this instrument has been evolving. One important achievement was the introduction of a touch trigger probe by Renishaw in the early 1970s. This technological advance and the addition of a motorized probe head in the 1980's, allowed the CMM to have automatic and accurate 3D measurements for different tested components.

The CMM is a contact metrology instrument that consists of a test probe that moves in three directions X,Y and Z. This device gives the Cartesian position of the test probe. The difference with this and the profilometer is that a random sample

of points across the surface under test is provided. Effectively, a point cloud of the surface is created and the sampling can be adjusted by simply touching the probe more densely in a given region. One of the advantages of the CMM over the profilometer, is that the  $x, y$  and  $z$  coordinates are given by the same instrument, avoiding the backlash and other travel errors introduced by the translation stage.

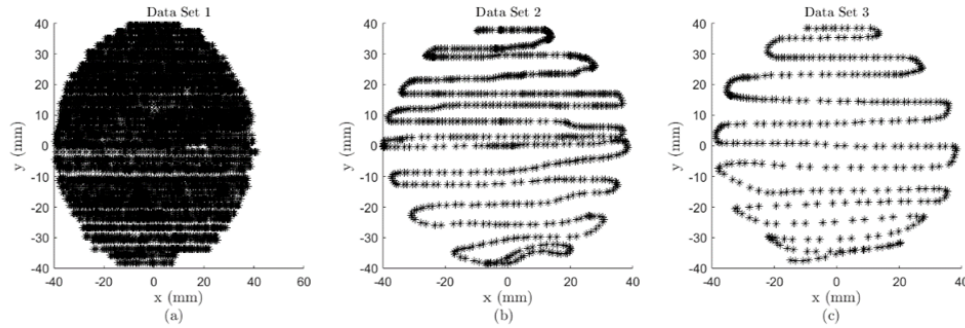


FIGURE 2.8. Sample points from the Coordinate Measuring Machine (a) Data Set 1. (b) Data Set 2. (c) Data Set 3

To obtain the sag data of the PAL, the Coordinate Measurement Machine in the College of Optical Sciences is used. This is a CMM Tesa Micro-hite. The size is  $18'' \times 28'' \times 16''$ . The PAL is mounted to a granite table and the surface is measured with with different patterns. These patterns are shown in Figure 2.8.

Three sets of discrete data from the surface are obtained, and these data are fit using the method described previously in Section 2.1.3. The differences between the measured data and the fitted data to 37 Zernike terms are shown in Figure 2.9.

The  $RMS$  errors for each set are the followings: Set 1  $RMS_1 = 0.0137mm$ , set 2  $RMS_2 = 0.0141mm$ , and set 3  $RMS_3 = 0.0122mm$ .

An average of the three data sets was taken and analyzed. The average  $RMS = 13.3\mu m$ . A representation of the surface is shown in in Fig. 2.10(a).After removing the lower terms, we get the surface shown in Fig. 2.10(b).

A comparison between the profilometer data and the CMM data with the low

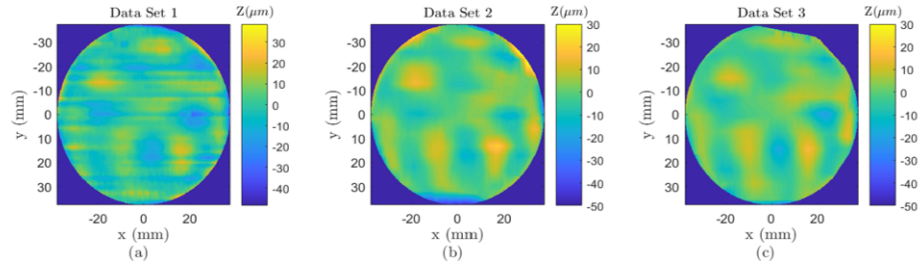


FIGURE 2.9. Differences from CMM Data and Fitting Data. (a) Data Set 1 (b) Data Set 2 (c) Data Set 3.

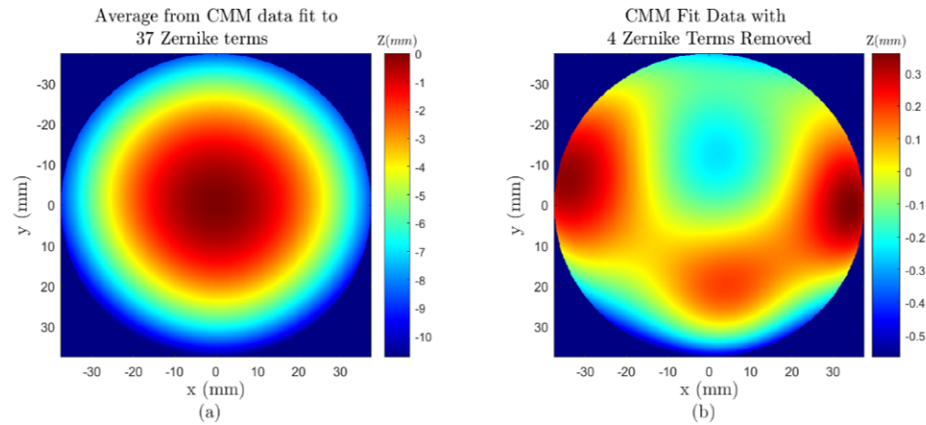


FIGURE 2.10. (a) Freeform Surface Fitting to 37 Zernike terms. (b) Freeform surface with low Zernike terms removed.

terms removed is presented in Figure 2.11. We found an  $RMS$  error of  $RMS = 0.0262mm$  and a  $PV = 0.1956mm$ . Most of the differences occur at the extreme edges of the lens.

The mean curvature was computed using Equation 2.1.12. The color map shown in Figure 2.12(a) shows the expected behavior of a progressive addition lens. The increment of curvature from the top to the bottom of the lens. This could be translated into an increment of the optical power, from the far region to the near region of a progressive addition lens.

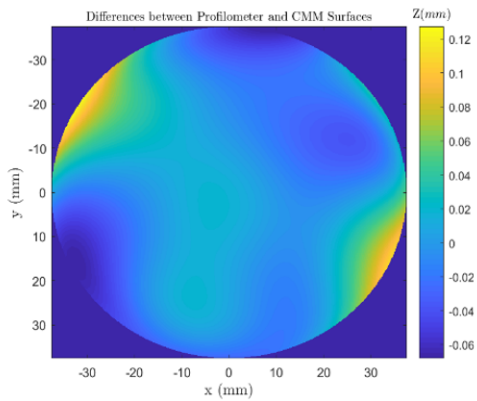


FIGURE 2.11. Comparison between profilometer data and CMM data, with  $RMS = 0.0262mm$  and a Peak of Valley value  $PV = 0.1956mm$ .

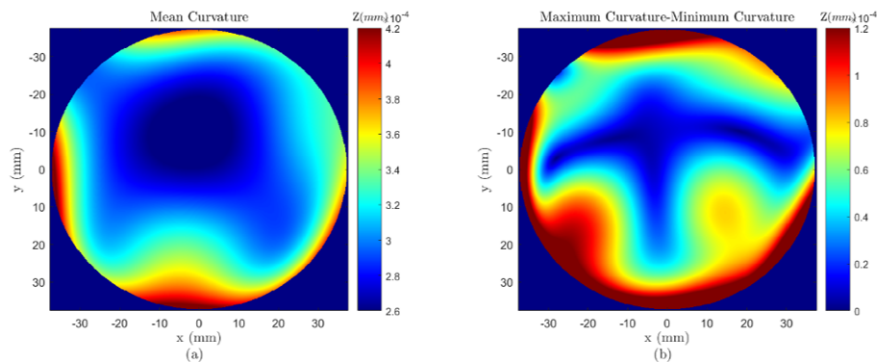


FIGURE 2.12. Curvature Maps of the freeform surface of a Progressive Addition Lens. (a) Mean Curvature Local Spherical. (b) Local Cylinder

Taking the differences between the principal curvatures of the surface, the cylinder power is found. As shown in Figure 2.12(b), the surface astigmatism again increases in the lower periphery, illustrating the behavior expected for a progressive addition lens.

After analyzing both contact methods to measure the freeform surface from the progressive addition lens, interesting properties of these spectacle lenses are found. The freeform surface introduces a power variation without discontinuity across the

lens and allows the wearer to see different object distances clearly. Yet, this surface also introduces cylinder power, especially in the blend regions, that leads to image blur when viewing through these regions.

Although these properties can be studied, the problem with these methods as described before is that they are contact methods, and there is risk of scratching the surface. Another problem with these contact methods is the time that takes to perform all the measurements. For these reasons, the following non-contact methods are explored. Both of the non-contact methods described below use the phase shifting technique to extract surface information. Phase shifting and the associated phase unwrapping techniques are explained in the following section.

### 2.3 Phase-Shifting and Phase Unwrapping

The principle of phase-shifting is used as a baseline for the following non-contact metrology methods. Therefore, a brief explanation is provided in this section. These metrology techniques use a sinusoidal light pattern projected onto the test surface [27]. The sinusoidal or fringe pattern is shifted  $N$  times by  $2\pi/N$ , where  $2\pi$  corresponds to one complete period of the sinusoid. The shifted pattern is recorded at each of the  $N$  locations. In the following cases, a four-step method is used, meaning  $N = 4$ . To retrieve the phase at each point on the surface the following expression is used

$$\Psi = \arctan \left( -\frac{I_2 - I_4}{I_1 - I_4} \right) \quad (2.3.1)$$

where  $I_1, I_2, I_3, I_4$  are the irradiance patterns of each measurement, given by

$$\begin{aligned}
I_1(x, y; 0) &= I'(x, y) + I''(x, y) \cos[\Psi(x, y)], \\
I_2(x, y; \frac{\pi}{2}) &= -I''(x, y) \sin[\Psi(x, y)], \\
I_3(x, y; \pi) &= I'(x, y) - I''(x, y) \cos[\Psi(x, y)], \\
I_4(x, y; \frac{3\pi}{2}) &= I''(x, y) \sin[\Psi(x, y)].
\end{aligned}
\tag{2.3.2}$$

From Equation (2.3.1), the phase is recovered using the arctangent function. A drawback of this function is that it has principal values in the range of  $-\pi$  to  $\pi$ . When the phase value exceeds this range, the phase is wrapped back into this range. Consequently, the phase can only be known to some integer multiple of  $2\pi$ . To solve this ambiguity, well-known algorithms to unwrap the phase, must be applied. In this work, Goldstein's algorithm has been applied for the analyses performed in this dissertation.

After unwrapping the phase, we can use the data to find the slope information of the surface. Fringes in  $X$  and  $Y$  must be projected to get the local slopes in both directions.

## 2.4 SCOTS

The Software Configurable Optical Test System (SCOTS) was used to test the PAL surface [28]. SCOTS is a very powerful tool to test optical surfaces fast, accurately and in an inexpensive way. This technique was previously used to test the Large Synoptic Survey Telescope tertiary mirror (LSST M3) and the Giant Magellan Telescope (GMT) primary mirror [29]. In recent works, it has been shown that this technique can be used to test refractive optical systems by measuring simple refraction elements [30] and testing the Large Binocular Telescope (LBT) secondary mirror null corrector [31].

### 2.4.1 Principle

The SCOTS principle, which is based on a reverse Hartmann test, is implemented in a simple configuration. An LCD screen illuminates the test surface with a pattern, replacing the traditional Hartmann Plate. A CCD camera with an external stop, represents the point source in the Hartmann test. A laptop is used to collect the images of the pattern presented on the LCD screen and reflected or transmitted from the test surface [28]. SCOTS measures the transverse ray aberration by finding the correspondence between the screen pixel location and the pixels on the CCD sensor. The transverse ray aberration can be used to find the test objects wavefront slopes [32] which in turn can be integrated using a polynomial fit or by zonal integration to give the wavefront and the surface departure from the ideal shape [31].

### 2.4.2 Experimental Setup

After obtaining the surface shape as explained in Section 2.1, the lens specifications are input into a ZEMAX model of the entire SCOTS system and the distances between the LCD and the camera are set keeping in mind that the CCD sensor area needs to cover the entire PAL surface.

In the SCOTS setup, as is shown in Fig. 2.13, the lens was mounted in a tip and tilt stage for alignment with the freeform surface facing the LCD screen. The distance chosen between the LCD and the test lens was  $z = 715$  mm, and from the test lens to the pinhole  $z = 1120$  mm. We used an LCD screen of  $1280 \times 1024$  pixels with a pitch of  $0.2940$  mm, a digital CCD camera with a lens of focal length  $f = 50$  mm, and a computer. The PAL is measured in transmission and the spherical surface currently is assumed to be perfectly spherical.

To measure the transverse ray aberration, the correspondence between the LCD screen pixels and the CCD pixels needs to be determined. To find this mapping, phase shifted sinusoidal patterns are displayed on the LCD screen oriented in both the x

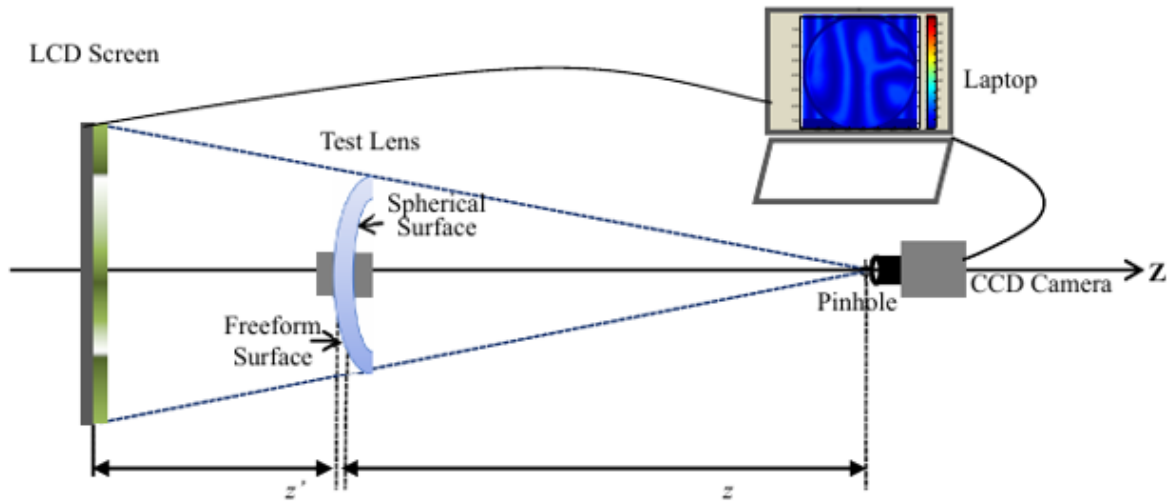


FIGURE 2.13. SCOTS experimental setup

and  $y$  directions. These fringes were green to improve the contrast of the images. Considerations of the pupil size and contrast are made. The image data are collected and compared to the ZEMAX model. The results are presented below.

### 2.4.3 Results

After data reduction, a comparison between the surface in the ZEMAX model and the measured surface is presented. It is important to mention that to separate the measurement error associated with the testing setup from the errors inherent to the test lens, repeated measurements rotating the lens by 180 degrees are captured. Figure 2.15 shows the differences between the profilometer data and the SCOTS data for orientations of 0 and 180 degrees. For 0 degrees a wavefront  $RMS = 12.2\mu m$  is found, while for 180 degrees the wavefront  $RMS = 13.9\mu m$ .

By direct subtraction of both maps reoriented to one another, the difference in RMS error is  $1.8\mu m$ . Averaging the results from the rotation, the wavefront RMS difference between the surface shape obtained with the profilometer data, and that



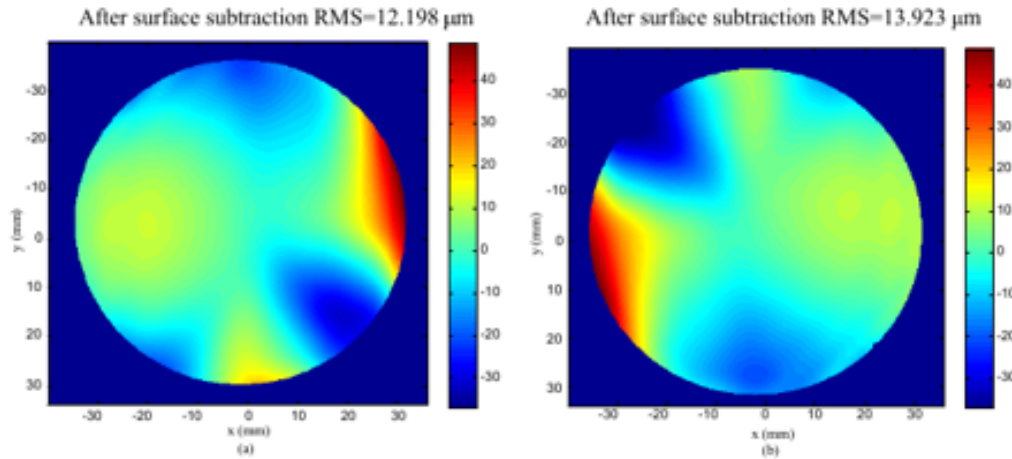


FIGURE 2.14. (a) Differences between profilometer and SCOTS data (b) Differences between profilometer and SCOTS data after a 180 degrees rotation (low order terms removed).

from SCOTS is  $12.3\mu m$ . Table 2.1 lists the wavefront errors departing from the ideal surface from the SCOTS test in the coefficients of the Zernike standard polynomial. The results show that the dominated errors were Astigmatism (Z6) and Trefoil (Z9).

Zernike Standard Polynomial	Coefficient	Zernike Standard Polynomial	Coefficient
Astigmatism Sin (Z5)	4.48	Coma Cos (Z8)	3.9424
Astigmatism Cos (Z6)	6.7001	Trefoil Sin (Z9)	6.0743
Coma Sin(Z7)	0.4103	Trefoil Cos (Z10)	2.6722

TABLE 2.1. Coefficient of the Zernike Standard Polynomial.

SCOTS can be used to test Progressive Addition Lenses with an average wavefront RMS of  $1.8\mu m$ , after removing low order terms. The profilometer measurements are limited by the accuracy of the repeated scans. While the profilometer is capable of highly accurate 1D scans, our addition of the translation stage likely introduced larger errors in the 2D cases through backlash and runout in the stage. However, by rotating the PAL between measurements, the error in the profilometer model and the

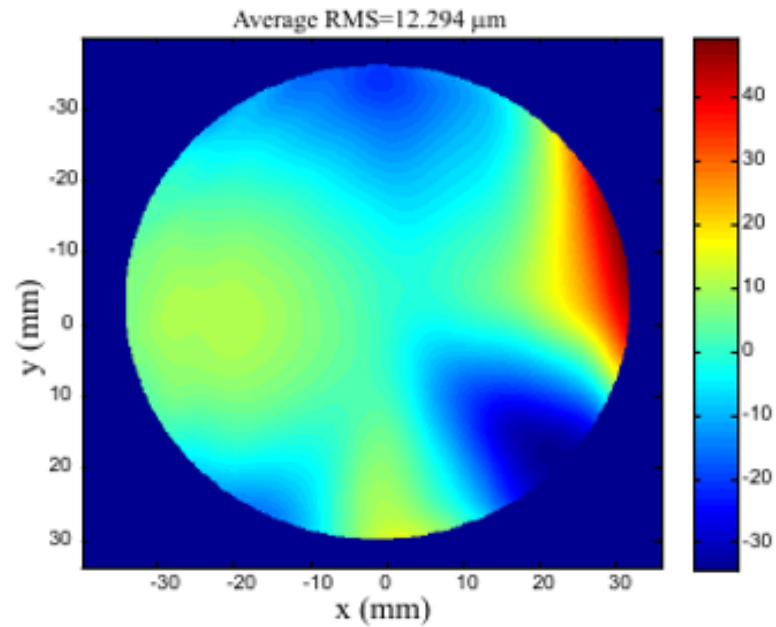


FIGURE 2.15. Differences between profilometer data and average of rotations.

measurement error of the SCOTS system can be separated to estimate the capabilities of the SCOTS system. The remaining discrepancies between the profilometry data and the SCOTS test are likely due to errors introduced by the back surface of the PAL. The back surface is assumed to be spherical so that the ZEMAX model can recover the progressive surface. Ideally, the back surface of the PAL should be measured by another means to incorporate its effect into the model. Traditional interferometry would be able to measure this back surface accurately since it is nearly spherical.

## 2.5 UV Deflectometry

The next technique to measure the Progressive Addition Lens is UV Deflectometry. The SCOTS test described above was performed in transmission and consequently, the back surface of the lens needs to be accurately known to back out the characteristics

of the freeform surface. Here, deflectometry in reflection is performed. One of the problems of testing the freeform surface of the PAL in reflection is the presence of ghost reflections due to the back surface. Both the anterior and posterior surfaces will reflect fringe patterns and in regions where these patterns overlap, the fringe contrast tends to become low. To avoid issues with the parasitic fringes from the back surface, a common technique is to temporarily coat the unwanted surface to reduce its reflectivity. This coating however slows down the testing and it would be beneficial to remove this step. To reduce unwanted reflections from the back surface, the transmission properties of the lens material will be used instead.

In Figure 2.16, a Transmission Plot for the PMMA is shown. At approximately  $\lambda = 365nm$ , the transmission of the PMMA is  $T \approx 10\%$ , which means that the reflection from the front surface at this wavelength is  $R \approx 90\%$ . If fringes are projected at this wavelength, the spurious reflections from the back surface are greatly reduced.

Figure 2.16 shows the same scene was taken under different lighting conditions to demonstrate the transmissivity of the PMMA. The left image depicts looking through the lens at a target with a UV camera and UV illumination. The lack of transmission through the lens obscures the target. The right image shows the same scene captured with a cellphone camera with visible illumination. In the wavelength region, the lens is transparent and the target is clearly visible to the camera.

### 2.5.1 Theory

To overcome the new challenges of testing freeform optical elements, different techniques have been studied to measure specular surfaces without contact.

One technique that has had successful results, in comparison with interferometric methods, is Phase Measuring Deflectometry. This technique measures the light deflection after the reflection or transmission from the surface under test [34].

Phase Measuring Deflectometry has been used to measure different ophthalmic

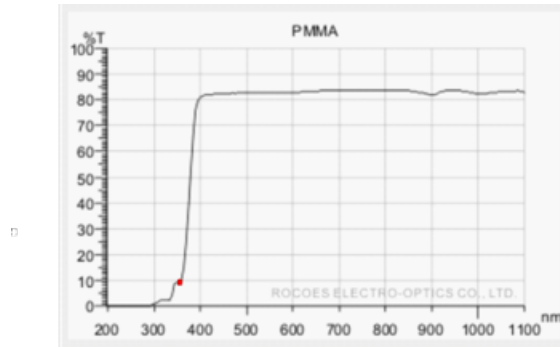


FIGURE 2.16. PMMA Transmission Plot, emphasizing transmission at  $\lambda = 365nm$  . Image reproduction from Roco.es Electro-optics.LTD [33].

elements. One example is the implementation of a deflectometric setup to measure the shape of a freeform IOL lens [35], and the measurement of the local curvature of the freeform surface of Progressive Addition Lenses [36].

However, this technique has some problems when testing transparent objects because of the reflections of the back surfaces. The reflection of the back surface and the front surface are superimposed. Several methods have been applied to overcome these problems [37]. One of them is the use of multiple fringe projections and work with an algorithm to separate the signals.

The second one is UV deflectometry, but because there are not spatial modulators at this wavelength, another approach has to be taken: Shift Line deflectometry. This technique instead of using a sinusoidal pattern, uses a line of UV light moved by a linear stage [36].

Here, a simple method to create a screen with a UV sinusoidal pattern is developed to enable UV deflectometry. This sinusoidal pattern, in turn, reflects from the surface under test and is captured by a camera.

Deflectometry consists of examining the distortions of phase shifted sinusoidal patterns reflected from the surface under test. These patterns reflected from the surface encode the local slope of the surface in their phase as given by Equation 2.5.1.

$$\phi = d \tan(2\alpha) \quad (2.5.1)$$

where  $\phi$  is the phase,  $d$  is the distance from the screen to the surface, and  $\alpha$  is the local slope.

To find a correlation between pixels in the CCD camera and fringes in the screen. Phase shifting techniques are employed, as it is explained in section 2.3, the same pattern phase shifted is projected onto the freeform surface and a series of pictures are taken. Later, phase unwrapping techniques are used to recover the local slopes of the surface.

### 2.5.2 Illumination System

To create the UV pattern, we used a high-power LED of wavelength  $\lambda = 365nm$  from Marktech Optoelectronics. This is an ultraviolet emitter working  $500mA$  at  $3.6V$ , with a view angle of  $120^\circ$ .

The fringes are projected onto a ground glass screen using a projection-condenser illumination system. This system is used because of a need for uniform illumination. This type of system consists on a condenser lens that images the light source into the plane of another lens called the projector lens. The condenser lens should be the faster one. A transparent object placed next to the condenser lens will be imaged by the projector lens onto the image plane.

In the setup, the condenser lens, focal length of  $f_1 = 35mm$  is placed at a distance of  $d_1 = 101.5mm$  from the LED source. A transparency with the fringe pattern is placed next to the condenser lens. The second lens, or projection lens of focal length  $f_2 = 50mm$  is placed at a distance  $d_2 = 53.4$  from the first lens, and the image screen is  $785.3$  from the second lens. Thorlabs UV lenses were used. A schematic diagram of the illumination system is shown in Figure 2.17.

The object was a binary line pattern printed on a transparency with a spatial

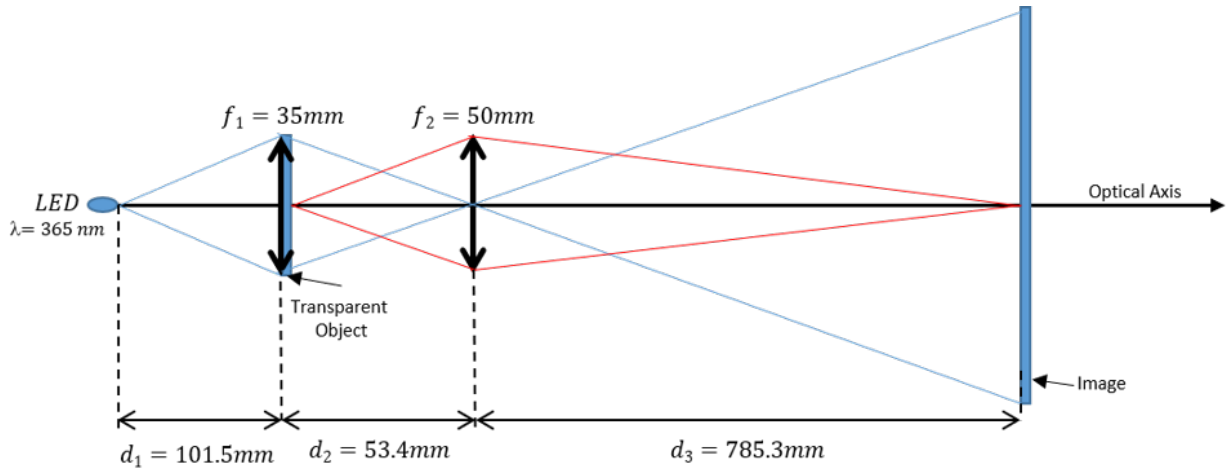


FIGURE 2.17. Fringe projection with an LED  $\lambda = 365nm$ .

frequency of  $f = 1.5lp/mm$ . This object is mounted on a linear stage to enable phase shifting the pattern. The image of the object is a sinusoidal pattern in the screen (ground glass) due mainly to high frequency losses from the aberrations associated with the projection lens. To characterize the required phase shifts, a relation between the distance displaced by the linear stage in the object plane and the resultant phase shift of the pattern on the image screen is found.

Pictures of the pattern on the image screen are captured and analyzed in MATLAB. A profile of the projected image is fit to a sinusoidal pattern such that

$$y(\Delta d) = A \sin(2\pi Bx + C(\Delta d)\pi), \quad (2.5.2)$$

where  $A$  is the amplitude,  $\Delta D$  the displacement of the linear stage in  $mm$ , and  $C(\Delta D)$  the phase shift as a function of the lateral displacement.. Eleven profiles are captured, displacing the translation stage every  $\Delta D = 0.05mm$ . In Figure 2.18, examples of some of the irradiance profiles through the captured images are shown along with the fitted sinusoid.

To find the lateral displacement corresponding to a phase shift the pattern of  $\pi/2$ ,

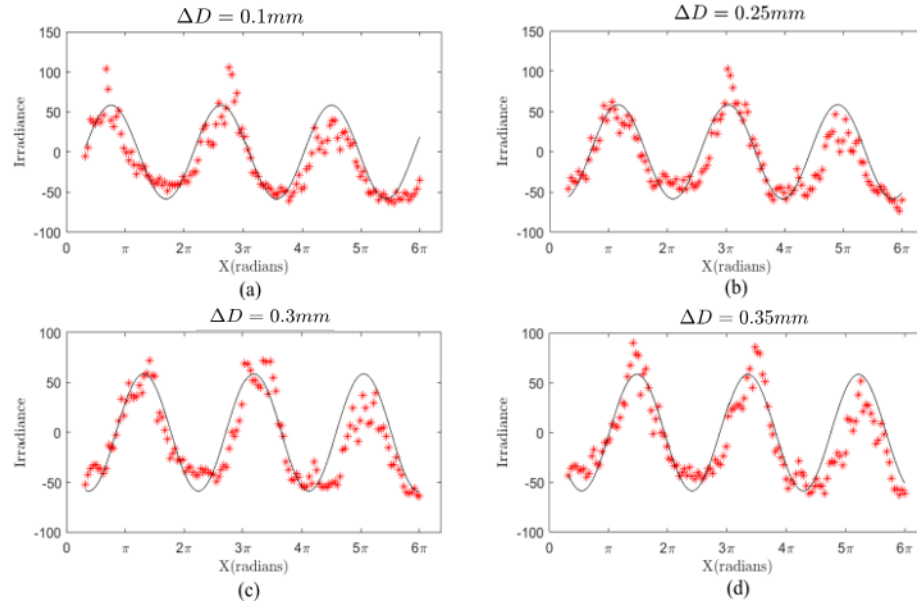


FIGURE 2.18. Irradiance profile at the screen with lateral displacement. (a) 10 mm (b) 25 mm (c) 30 mm (d) 35 mm.

the phase shift  $C(\Delta D)$  is plotted against the lateral displacement  $\Delta D$ , to find a linear relation. This linear relationship is shown in Figure 2.19. A translation of the object  $\Delta D = 0.15\text{mm}$  corresponds to a phase shift the irradiance pattern of  $\pi/2$ .

### 2.5.3 Experimental Setup

After constructing the illumination system and characterizing the phase shift, the PAL is mounted next to the image screen.

One consideration in setting up the deflectometry system is the size of the piece under test. The projection pattern should be big enough to cover all the surface area of the test part. Even though the focal lengths and the distances were carefully chosen to get a magnification of  $m = 14.6$ , the PAL had to be very close to the screen  $d_{\text{screen-lens}} = 40\text{mm}$  to cover the entire part. This proximity creates another complication in the pronounced angle that the lens made with respect to the screen

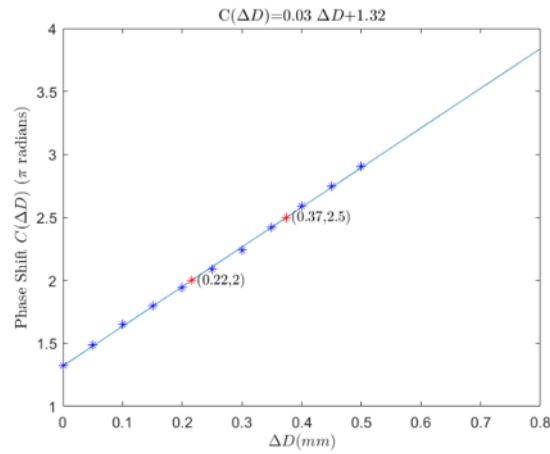


FIGURE 2.19. Linear Relation of irradiance profile phase shift in function of lateral displacement of the object.

and the location of the camera. An optimal position trying to cover the major part of the test surface was found and all images were captured from this location.

As mentioned in Section 2.5.1, fringes in orthogonal directions should be projected to recover the local surface in two directions.

The camera used to take pictures, was a Sony XC-EU50 1/2" CCD. It has an applicable wavelength sensitivity range of 300 – 420 nm with a near ultraviolet sensitivity in the i-line, 365nm. The camera is monochrome with a 768x494 pixel resolution. The CCD horizontal driving frequency is 14.318MHz, and the CCD vertical driving frequency is 15.734kHz.

The lens used was a 25mm Standard UV Fixed Focal Length Lens, with a wavelength range of 230-1200nm. A 1/2" sensor, and a field of view of  $FOV = 14^\circ$  and a working distance of 230 –  $\infty$ mm.



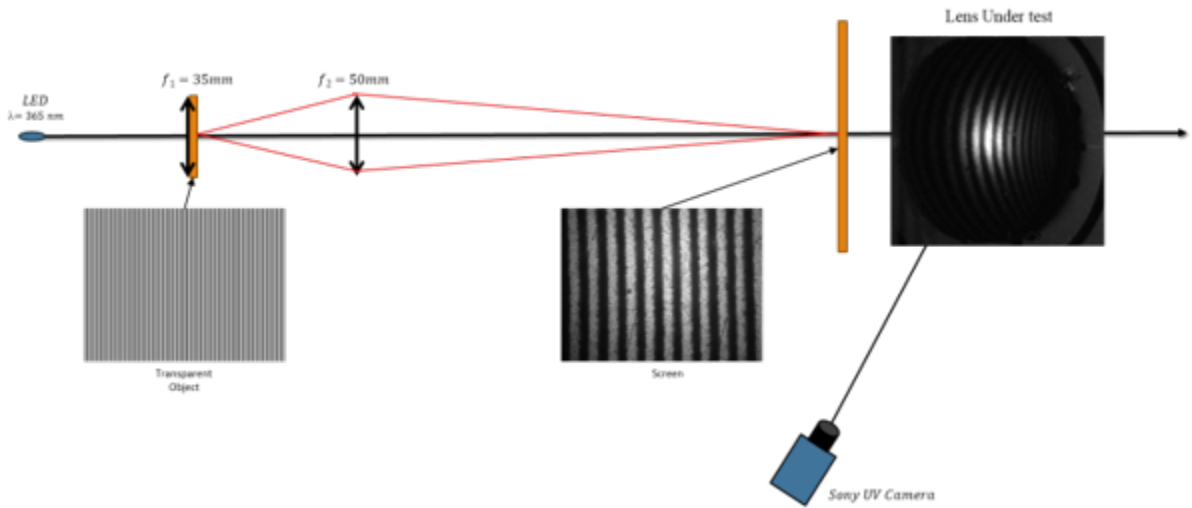


FIGURE 2.20. Experimental Setup Deflectometry System  $\lambda = 365nm$ .

#### 2.5.4 System Calibration

Due to the complicated geometry of the setup, a calibration method is proposed. After fixing the position of the projection screen and the camera. A calibration sphere is placed; this sphere is chosen to have a radius of curvature  $R_{sphere} = 77mm$ , close to the base curvature of the freeform surface of the progressive lens.

Phase shifting, and phase unwrapping techniques are applied to the reference sphere. However, the resultant images are distorted because of the angle between the camera and the lens. As shown in Figure 2.21, circular shape of the lens appears to be an ellipse.

The method proposed is to find a transformation to map the reflected curved fringes into the sphere to straight lines, representing the slopes in x and y direction of the reference sphere.

First, the pictures of the vertical lines were superimposed over the horizontal lines creating a mesh as shown in Figure 2.22(c). The coordinates of the intersections of the lines are found  $(x_N, y_N)$  as shown in Figure 2.22(a) and 2.22(b). A nominal grid

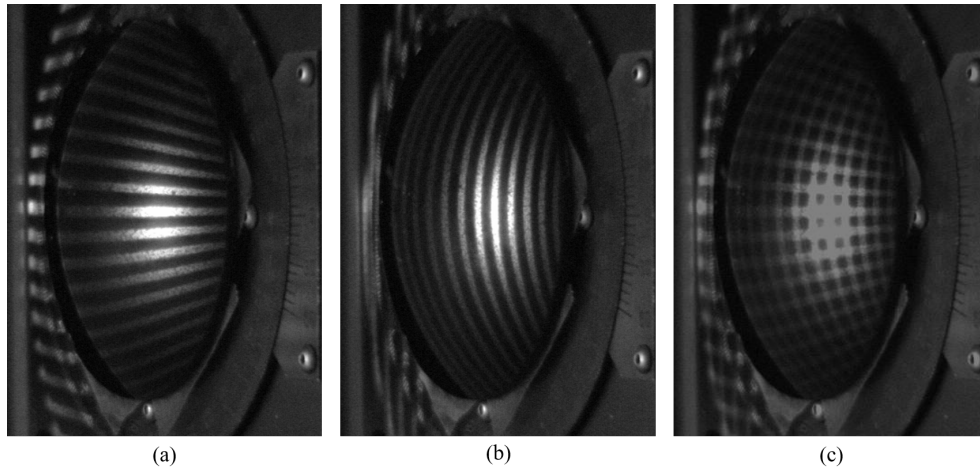


FIGURE 2.21. Reflected fringes into calibration Sphere.

is created with equally space points as shown in Figure 2.22(c).

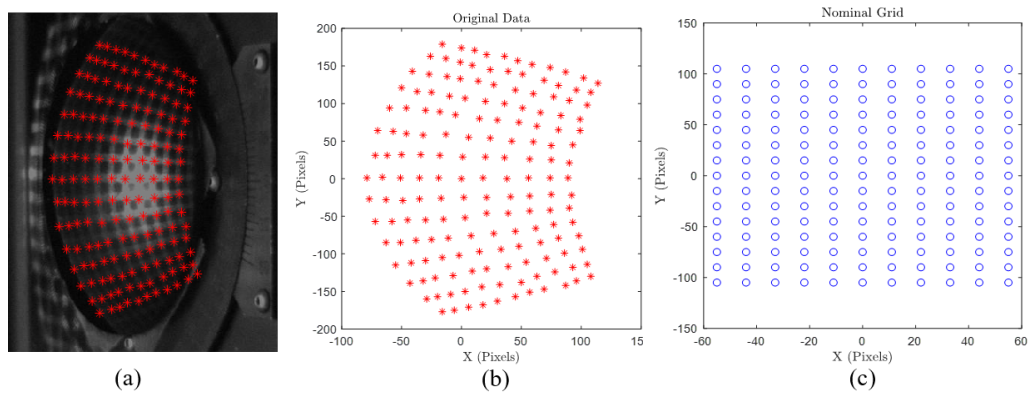


FIGURE 2.22. (a) Intersection of lines. (b) Original Data. (c) Nominal Grid.

The new coordinates are expressed by

$$\begin{aligned} x'(u, v) &= a_1u + a_2v + a_3u^2 + a_4uv + a_5v^2 + a_6u^3 + a_7u^2v + a_8v^2u + a_9v^3, \\ y'(u, v) &= b_1u + b_2v + b_3u^2 + b_4uv + b_5v^2 + b_6u^3 + b_7u^2v + b_8v^2u + b_9v^3. \end{aligned} \quad (2.5.3)$$

The goal is to find the coefficients that map the original coordinates  $(x_N, y_N)$  to

the nominal grid  $(x'_N, y'_N)$ . To find the expansion coefficients of the transformation, the square fit method is applied to find the new  $x$  coordinates, and then to find the new  $y$  coordinates. As described in Section 2.1.3, consider the matrix equation

$$\mathbf{Ax} = \mathbf{b}, \quad (2.5.4)$$

The matrix  $\mathbf{A}$  has  $N$  rows, where  $N$  is the number of sample points, and  $M$  columns, where  $M$  is the number of terms to fit in this case  $M = 9$ . The matrix  $\mathbf{A}$  is given by

$$\mathbf{A} = \begin{pmatrix} x_1 & y_1 & x_1^2 & x_1 y_1 & y_1^2 & x_1^3 & x_1^2 y_1 & y_1^2 x_1 & y_1^3 \\ x_2 & y_2 & x_2^2 & x_2 y_2 & y_2^2 & x_2^3 & x_2^2 y_2 & y_2^2 x_2 & y_2^3 \\ \cdot & \cdot & \cdot & \cdot & \cdot & \cdot & \cdot & \cdot & \cdot \\ \cdot & \cdot & \cdot & \cdot & \cdot & \cdot & \cdot & \cdot & \cdot \\ \cdot & \cdot & \cdot & \cdot & \cdot & \cdot & \cdot & \cdot & \cdot \\ x_N & y_N & x_N^2 & x_N y_N & y_N^2 & x_N^3 & x_N^2 y_N & y_N^2 x_N & y_N^3 \end{pmatrix}. \quad (2.5.5)$$

The vector  $\mathbf{x}$  is a column vector of  $M$  elements, containing the expansion coefficients that have to be determined.

$$\mathbf{x} = (a_1 \ a_2 \ a_3 \ \dots \ a_M)^T. \quad (2.5.6)$$

$$\mathbf{y} = (b_1 \ b_2 \ b_3 \ \dots \ b_M)^T. \quad (2.5.7)$$

The vector  $\mathbf{b}$  is a column vector of  $N$  elements, given by

$$\mathbf{b} = (x'_1 \ x'_2 \ x'_3 \ \dots \ x'_N)^T. \quad (2.5.8)$$

$$\mathbf{b} = (y'_1 \ y'_2 \ y'_3 \ \dots \ y'_N)^T. \quad (2.5.9)$$

Finally, the vector of expansion coefficients is given by

$$\mathbf{x} = [\mathbf{A}^T \mathbf{A}]^{-1} \mathbf{A}^T \mathbf{b}. \quad (2.5.10)$$

The elements of  $\mathbf{x}$  contain the expansion coefficients that will map the original coordinates to the corresponding coordinates in a nominal grid. Given as a result the undistorted data.

The method is applied two times, one for each coordinate ( $x$  and  $y$ ), and the coefficients found are presented in Table 2.2.

X Coefficients	Y Coefficients
$a_1 = 0.84111818$	$b_1 = -0.01004258$
$a_2 = -0.01271434$	$b_2 = 0.40216922$
$a_3 = -0.00083831$	$b_3 = -0.00022106$
$a_4 = -0.00003902$	$b_4 = 0.00100184$
$a_5 = -0.00171389$	$b_5 = -0.00004010$
$a_6 = 0.00000776$	$b_6 = 0.00000191$
$a_7 = 0.00000274$	$b_7 = 0.00000471$
$a_8 = 0.00000522$	$b_8 = 0.00000088$
$a_9 = 0.00000002$	$b_9 = 0.00000126$

TABLE 2.2. Distortion Coefficients.

Equations (2.5.5) were applied to the original data to find the new coordinates. A comparison between the undistorted data and the nominal grid can be found in Figure 2.23.

The coefficients found are applied to the unwrapped phase of the sphere shown in Figure 2.24(a) and 2.27(a), obtaining a new phase map shown in Figure 2.24(b) and Figure 2.27(b). As it was expected, after correcting for distortion, planes describing phase in  $x$  direction and phase in  $y$  direction are found.

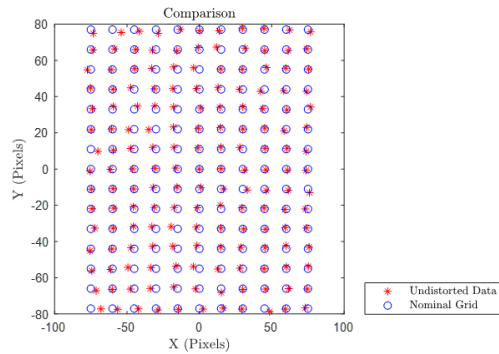


FIGURE 2.23. Comparison between Nominal Grid and Undistorted Data.

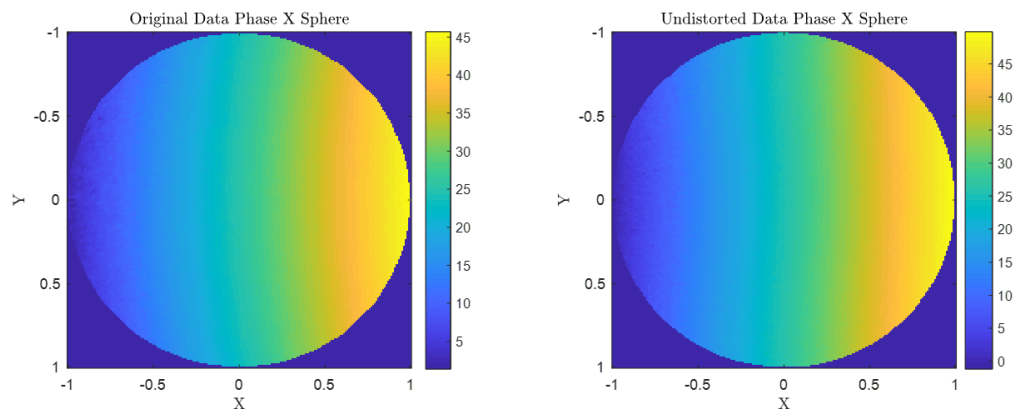


FIGURE 2.24. (a) Original map Phase in X from Reference Sphere. (b) Undistorted map Phase in X from Reference Sphere.

### 2.5.5 Fitting Data

The data obtained after applying the distortion transformation, is related to the surface slopes of the surface under test [25]. The phase maps in  $x$  leads to a set of  $N$  slopes in the  $x_P$  direction, and the phase maps in  $y$  leads to a set of  $N$  slopes in the  $y_P$  direction. Where  $N$  is the number of sample points, in this case number of pixels that covers the surface area. This set is given by

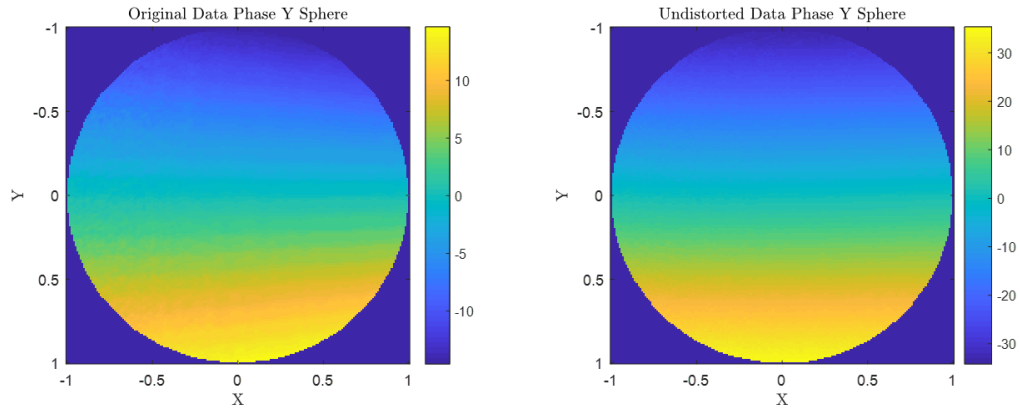


FIGURE 2.25. (a) Original map Phase in Y from Reference Sphere. (b) Undistorted map Phase in Y from Reference Sphere.

$$\left\{ \frac{\partial z_P(x_{Pk}, y_{Pk})}{\partial x_P}, \frac{\partial z_P(x_{Pk}, y_{Pk})}{\partial y_P} \right\}, \quad (2.5.11)$$

where  $k = 1 \dots N$ . This data is represented as a linear combination of the cartesian derivatives of the Zernike polynomials.

$$slopes_x = \sum_{n,m} a_{n,m} \frac{\partial Z_n^m(\rho_x, \rho_y)}{\partial \rho_x} \quad \text{and} \quad slopes_y = \sum_{n,m} a_{n,m} \frac{\partial Z_n^m(\rho_x, \rho_y)}{\partial \rho_y} \quad (2.5.12)$$

The expansion coefficients for the gradient data are the expansion coefficients for the fit of the surface shape (within a constant offset). Then the surface shape can be expressed by

$$z(\rho_x, \rho_y) = \sum_{n,m} a_{n,m} Z_n^m(\rho_x, \rho_y), \quad (2.5.13)$$

To fit the gradient data to the derivatives of the Zernike polynomials, the method used is similar to the one described in Section 2.1.3, consider the matrix operation

$$\mathbf{Ax} = \mathbf{b}, \quad (2.5.14)$$

In this case, the matrix  $\mathbf{A}$  has  $2N$  rows, and contains the derivatives values of the Zernike polynomials. The first  $N$  rows correspond to the  $N$  slopes in the  $x_p$  values followed by  $N$  rows of the  $N$  slopes in the  $y_p$  direction.

$$\mathbf{A} = \begin{pmatrix} \frac{\partial Z_{-1}^{-1}(x_{P1}, y_{P1})}{\partial x_P} & \cdots & \frac{\partial Z_{n_{max}}^{n_{max}}(x_{P1}, y_{P1})}{\partial x_P} \\ \cdot & \cdot & \cdot \\ \frac{\partial Z_{-1}^{-1}(x_{PN}, y_{PN})}{\partial x_P} & \cdot & \frac{\partial Z_{n_{max}}^{n_{max}}(x_{PN}, y_{PN})}{\partial x_P} \\ \frac{\partial Z_{-1}^{-1}(x_{P1}, y_{P1})}{\partial y_P} & \cdot & \frac{\partial Z_{n_{max}}^{n_{max}}(x_{P1}, y_{P1})}{\partial y_P} \\ \cdot & \cdot & \cdot \\ \frac{\partial Z_{-1}^{-1}(x_{PN}, y_{PN})}{\partial y_P} & \cdots & \frac{\partial Z_{n_{max}}^{n_{max}}(\rho_x, \rho_y)}{\partial y_P} \end{pmatrix} \quad (2.5.15)$$

The vector  $\mathbf{x}$ , contains the expansion coefficients data

$$\mathbf{x} = (a_{0,0} \ a_{1,-1} \ a_{1,1} \ \dots \ a_{n_{max}, n_{max}})^T, \quad (2.5.16)$$

and the column vector  $\mathbf{b}$  the measured gradient

$$\mathbf{b} = \left[ \frac{\partial z_P(x_{P1}, y_{P1})}{\partial x_P} \ \frac{\partial z_P(x_{PN}, y_{PN})}{\partial x_P} \ \frac{\partial z_P(x_{P1}, y_{P1})}{\partial y_P} \ \cdots \ \frac{\partial z_P(x_{PN}, y_{PN})}{\partial y_P} \right]^T. \quad (2.5.17)$$

The vector of the expansion coefficients is again

$$\mathbf{x} = [\mathbf{A}^T \mathbf{A}]^{-1} \mathbf{A}^T \mathbf{b}. \quad (2.5.18)$$

Because the  $\mathbf{A}$  matrix, is at the derivative, the piston coefficient is not included. Then this coefficient normally is set when the surface is zero at the origin.

### 2.5.6 Calibration Sphere

The method outlined in Section 2.5.4 is applied to the phase results obtained from the sphere. The data is fitted to 4 Zernike terms. The pixel size in  $mm$  is *pixel size* =  $0.1781mm$ . A scale factor is found by calculating the sag theoretical value of the sphere at the edge of the area used  $D = 21.37mm$ .

$$SAG = R - \sqrt{\left(R^2 - \left(\frac{D}{2}\right)^2\right)}, \quad (2.5.19)$$

where  $R = 77mm$ .  $SAG(21.37) = 0.7451mm$ . The scale factor found is *scale factor* =  $0.4565mm$ . The sphere map removing tip and tilt in *mm* is shown in Figure 2.26.

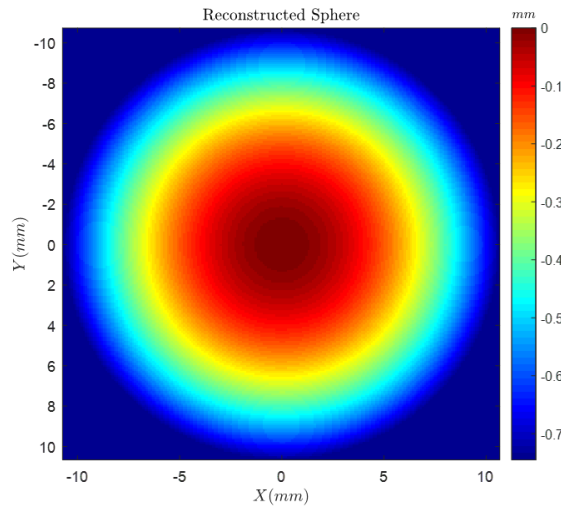


FIGURE 2.26. Reconstructed Sphere.

### 2.5.7 Results

Phase shifting, and phase unwrapping techniques are used to obtain the phase maps for the freeform surface of the Progressive Addition Lens. To undistort the data, the coefficients found in the calibration step are applied to the PAL phase maps, the final undistorted phase maps are shown in Figures 2.28(b) and 2.29(b). The data is normalized.

After applying the method outlined above to the gradient data, the recovered surface is fitted to 45 Zernike terms. The reconstructed freeform surface of the Progressive Addition Lens is shown in Figure 2.30.



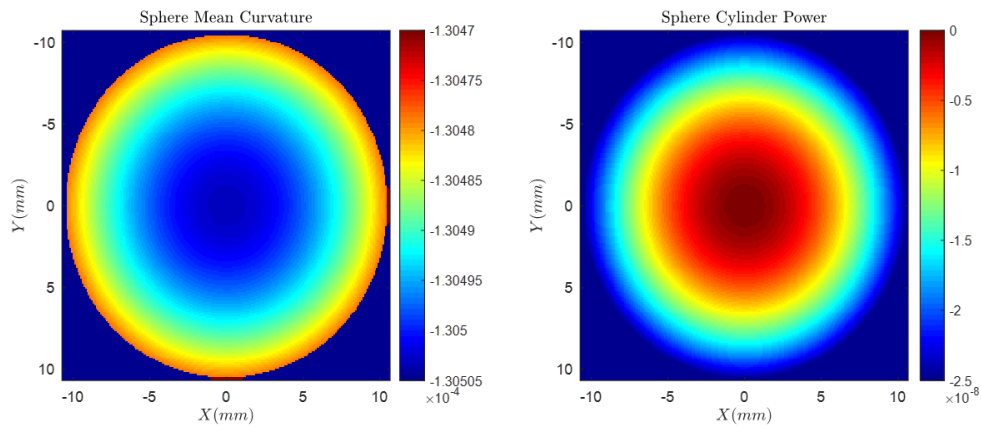


FIGURE 2.27. Sphere Mean Curvature and Cylinder power.

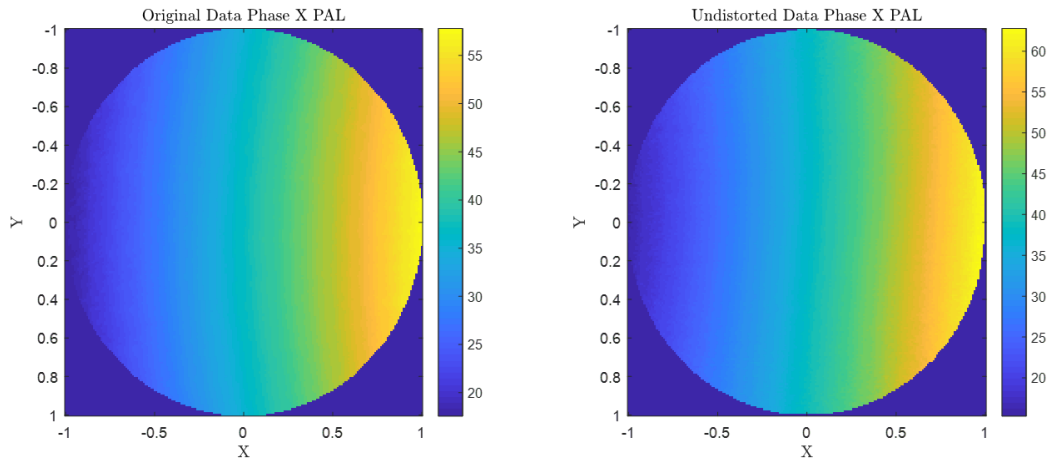


FIGURE 2.28. (a) Original map Phase in X from PAL under test. (b) Undistorted map Phase in X from PAL under test.

The scale factor previously found in Section 2.5.6 is applied to the data to find the surface map in  $mm$ . The Fundamental Forms for differential geometry mentioned before are applied to find the mean curvature related to spherical power and cylinder power. The PAL spherical power map and Cylinder power map are shown in Figures 2.31.

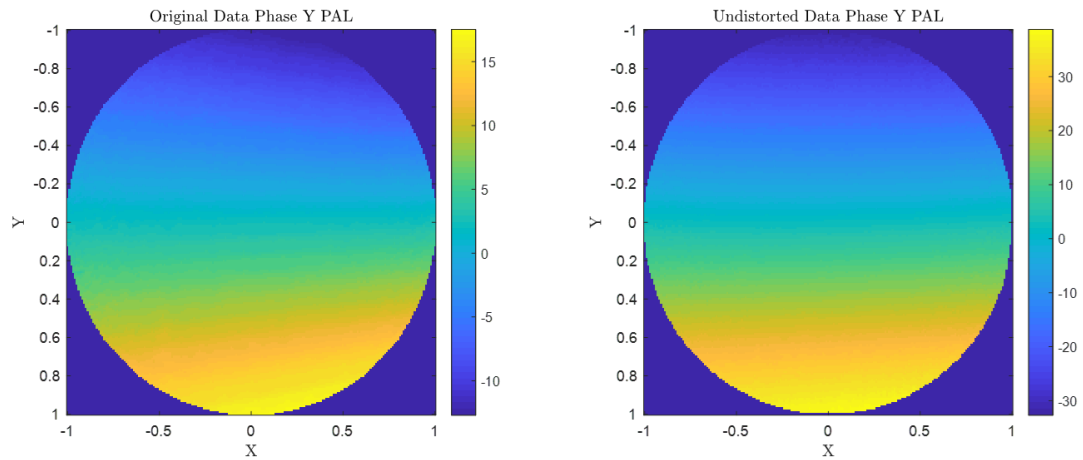


FIGURE 2.29. (a) Original map Phase in Y from PAL under test. (b) Undistorted map Phase in Y from PAL under test.

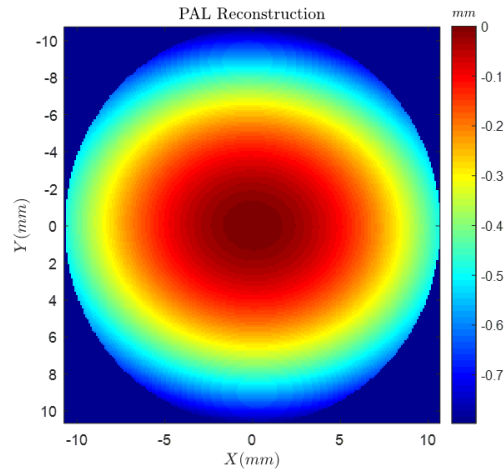


FIGURE 2.30. Reconstructed PAL surface.

### 2.5.8 Conclusions and Future Work

A new calibration method was proposed in order to recover the surface shape of the Progressive Addition Lens using a reference sphere. The distortion coefficients to obtain planes that represent the slopes in  $x$  and  $y$  direction of the reference sphere were

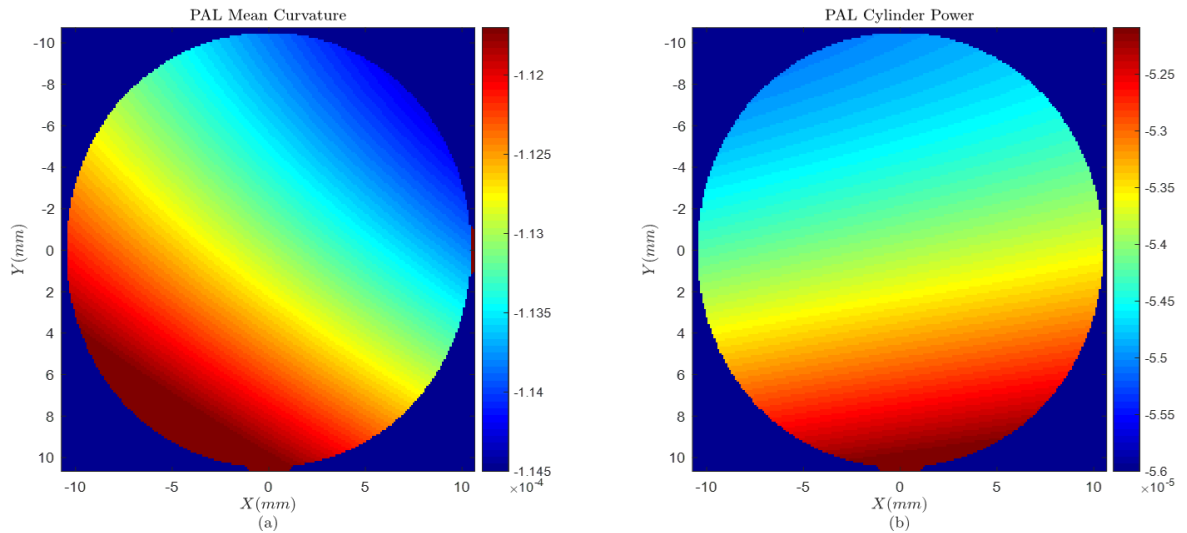


FIGURE 2.31. Reconstructed PAL surface.

found. However, the area to test is minimum because of the geometry of the system and the contrast of the reflected fringes at the edge of the lens. The reconstructed surface of the calibration sphere was used to find the scale factor that converts phase into  $mm$ . This scale factor is used to find surface height in  $mm$  of the PAL. The mean curvature and the cylinder power of the progressive addition lens didn't match the expected behavior of the Progressive Addition Lens. There are several reasons to consider, one is that the orientation and the area of the lens under test did not include the region of interest. Other reason is that other method to consider the geometry of the system has to be included. Future work by implementing another calibration method is suggested.

## CHAPTER 3

# SIMULATION OF MULTIFOCAL VISION

In Chapter 2, the freeform surface of a progressive addition lens is characterized by a mathematical approach. This is a very important process to see if the optical element is well fabricated and meets the design specifications. However, in terms of ophthalmic artifacts, acceptance by the wearer has the same importance as surface verification. If the wearer does not feel comfortable with the treatment used or has visual artifacts, it is as useless as a not well fabricated spectacle lens.

As explained in Chapter 1, there is a variety of progressive addition lens designs. The biggest trade-off is that PALs introduce unwanted aberrations not acceptable to all the patients. In this chapter, a new technique of realistic simulation is used as a suitable tool to give a preliminary insight into PALs performance. These simulations can allow the designer to understand the implications of various design choices, as well as provide an understanding of the required tolerances on freeform surface.

### 3.1 Theory and Image Simulation

The most important concept of this chapter is the notion of the point spread function (*psf*), also called the impulse response of an imaging optical system. It is the image of a perfect point source through the optical system. The *psf* is a metric of optical performance, serving as an indicator of the aberrations in a lens. If the system is diffraction limited, the *psf* will be the Airy pattern. In the presence of aberrations, the *psf* spreads out and its peak value diminishes leading to blurry of the point.

For scene simulation, each point in the scene can be considered a point source weighted by the local irradiance and spectral content. The simulated image is a superposition of all of the *psfs* from the scene. In general, the *psfs* will be dependent

upon the field position of the point source. The shape of the *psfs* will change from point to point and creating a simulation with this superposition is computationally intensive because of the need to recalculate the *psf* at each point in the field. To accelerate the simulation, scene simulation is usually achieved by convolving the system point spread function formed by an optical system with a scene. This technique assumes that the *psf* is shift invariant, so the *psf* only needs to be calculated once. Further increases in speed are achieved by performing this operation in Fourier domain using the convolution theorem and the computational optimization of the Fast Fourier Transform (FFT).

The convolution theorem states that in a linear shift invariant system (LSI), a convolution operation between the input  $f(x, y)$  and the impulse response  $h(x, y)$  in space domain, is equivalent to a multiplication operation in Fourier domain [38].

$$g(x, y) = f(x, y) h(x, y) \quad G(\xi, \eta) = F(\xi, \eta) H(\xi, \eta) \quad (3.1.1)$$

The following diagram illustrates this theorem, where *psf*  $(x, y)$  is the impulse response of the system,  $o(x, y)$  is the system input and  $i(x, y)$  the system output [39].

$$\begin{array}{ccccc} o(x, y) & \xrightarrow{*} & \text{psf}(x, y) & \xrightarrow{=} & i(x, y) \\ \mathcal{F} \downarrow & & \mathcal{F} \downarrow & & \mathcal{F}^{-1} \uparrow \\ O(\xi, \eta) & \xrightarrow{\times} & \text{PSF}(\xi, \eta) & \xrightarrow{=} & I(\xi, \eta) \end{array}$$

Nonetheless, optical systems have a shift variant point spread function, this means that the *psf* changes for different fields. To simulate shift variant cases, the scene is divided into regions over which the *psf* is approximately the same (i.e. isoplanatic patches), convolution is performed, and then all the regions are added to complete the

whole scene. Care must be taken using this technique. The field must be sufficiently sampled to ensure the variation in *psfs* is adequately sampled and the individual areas need to be blended to avoid artifacts at the edges of the regions. Raytracing software, such as Zemax OpticStudio (Zemax, LLC, Kirkland, WA), performs image simulation by sampling psf on a grid over a specific field of view, the *psf* for each pixel is then interpolated from the nearest *psfs*. Each point spread function is convolved with the corresponding pixel to obtain the final image [40]. Furthermore, image simulations using this technique typically only assume a single object plane. Due to the progressive addition lenses nature, consideration of different object plane depths has to be added.

As explained in Chapter 1, the different powers of a progressive addition lens are selected by eye rotation and head movement. Furthermore, the wearer is typically looking at objects at multiple distances, using the upper portion of the lens for distance objects and the lower portion of the lens to read. Therefore, in this dissertation, a different approach to scene simulation is used. The image simulation was built up by a superposition of *psfs* calculated across the field, as well as for a multitude of depths. In effect, a three-dimensional matrix of *psfs* is created and a three-dimensional scene processed to create the simulation. Details are explained in the following sections.

## 3.2 Algorithm Overview

In this section, an overview of the method used to perform scene simulation is presented. The method was implemented into a MATLAB script that in general terms consists in the following steps. The MATLAB script is contained in the Appendix.

1. Divide the image into the three RGB channels to process each separately.
2. Divide the field of view to simulate into the number of pixels for each image, in this manner each pixel will correspond to a certain field in the scene.

3. Choose the distance where the object plane is located.
4. Find the corresponding *psf* in the data base previously stored into .mat file.
5. Choose between these options: a) The *psf* exists. b) The *psf* doesnt exist: choose the 4 nearest point spread functions to the field of view, interpolate to get the correspondent *psf* at that field.
6. The point spread function is weighted by the RGB value at the corresponding pixel, the output *psf* is stored into a new matrix.
7. All the point spread functions are added to get the final values for each channel.
8. All the three-color channels are recombined up to obtain the simulated scene.

From the size of the image to simulate, to the optical system and the creation of the *psf* database employed, several factors must be considered to perform this process. In the following sections each step will be explained in detail.

### 3.3 *Psf* Database Creation

Before implementing the algorithm described in Section 3.2, a *psf* database has to be created. Due to the nature of the lens, the point spread function is not shift invariant, quickly changing at different points in the field. It also depends on depth information for each object.

This database is built by simulating the optical system under study in Zemax OpticStudio (Zemax, LLC, Kirkland, WA), sampling a field of view of  $FOV = \pm 30^\circ$ , that corresponds to the field of view of the eye, by an  $11 \times 11$  grid, and collecting the corresponding point spread function at every field. To do this, a MATLAB script was written to interface with Zemax for the collection of the *psf* map, field in  $X$ , field in  $Y$ , pixel size in  $mm$  and the depth location of the field.

In Zemax, there are two options to calculate the *psf* of an optical system: the Huygens *psf* and the *FFT psf*. The Huygens *psf* uses physical optics propagation to determine the electric field amplitude and the irradiance pattern given the wavefront shape in the exit pupil. While, this technique can be more accurate in some systems, the *FFT psf* technique provides advantages in computation time. In this dissertation, it is sufficient to use *FFT psf* to minimize computational time. It is important to know how Zemax calculates the point spread function of an optical system. In theory, it is computed by tracing a grid of rays from a point to the image plane, then tracing back to the exit pupil, and calculating the optical path difference at this plane. This in effect gives the pupil function of the system for a given field point. The modulus-squared Fourier transform of this pupil function is then the *FFT psf* [41]. Even with the computational efficiency of the *FFT*, the sheer number of *FFT*s needed to do shift variant simulations can rapidly make the simulation process infeasible and the *psf* database seeks to find a balance between computation time and simulation accuracy.

The *psf* database consists on a *.mat* file for different depth locations of the fields. Every *.mat* file contains information from the Zemax simulation output. The *psf* map is an image represented by  $N_x \times N_y$  pixels. It is important to consider that depending on the field of view, the pixel size in *mm* will change. To ensure proper scaling in the final simulation, the pixel dimensions have to be stored to a uniform physical size for of all the *psfs*, as explained more in detail in the following sections.

### 3.3.1 Lens-Eye Model

The optical system to characterize the progressive addition lens was simulated using raytracing software. It consists of a lens of diameter  $D_{lens} = 75mm$ , that is described by a combination of one Zernike surface (obtained from the methods described in Chapter 2) and a back surface represented by a perfect sphere of radius of curvature



$R = 83.728mm$ . The surfaces are separated by a center thickness  $t = 10.2mm$ , and *PMMA* material. Besides the Zernike surface, the parameters used to describe the PAL, were obtained from the product specification and processing guide of the Kodak progressive Lens [42].

The eye is simulated by a simplified system that facilitates the action of eye rotation. The simplified eye is simulated simply an aperture, considered to be in bright lighting conditions, having a diameter of  $D_{stop} = 3mm$ . The model is represented by the aperture stop located at the center of rotation of the eyeball,  $27mm$  from the vertex of the back surface of the spectacle [6]. At this position, a paraxial lens with focal length  $f = 16.6mm$  is added. The focal length of the paraxial lens matches the mean ocular power of the eye  $\phi = 60.24D$ . It is important to remember, that PALs are used as treatment for presbyopia when the eye loses accommodation. For this reason, it is safe to assume a fixed focal length for the paraxial lens for all object distances. Finally, the image plane is fixed at the paraxial lens focal point. The optical layout of the system is shown in Figure 3.1. In this manner, simply selecting different object fields has the same effect as the eye rotating to look at that field. The aberrations associated with the eye are assumed to be negligible compared to those introduced by the progressive lens. For a  $3mm$  pupil, this is a reasonable assumption.

For this analysis, the human eye field of view is  $\pm 30^\circ$  and the field was sampled every  $6^\circ$  to get a  $11 \times 11$  grid as it is shown in Figure 3.2. This sampling was sufficient, because later bilinear interpolation is applied to find the psf at locations between sampled points. Verification of this sampling is provided in more detail below. Eye rotation is effectively accomplished by selecting the various fields in Figure 3.2. For example, the dark blue field bundle in the figure represents the eye looking through the left side of the lens, whereas the green field bundle in the figure represents the eye looking through the top portion of the lens.

After creation of the Zemax model, a MATLAB script is used to retrieve the point spread functions information. This process is repeated for different depth locations

Surf.Type	Comment	Radius	Thickness	Material	Coating	Semi-Diameter	Chip Zone	Mech Semi-Dia	Conic
0 OBJECT	Standard	Infinity	Infinity			Infinity	0.000	Infinity	0.0...
1 (aper)	Zernike Standard Sag	Infinity	10.200	PMMA		37.500 U	-	-	0.0...
2 (aper)	Standard	83.728	27.000			37.500 U	0.000	37.500	0.0...
3 STOP	Standard	Infinity	0.000			1.500 U	0.000	1.500	0.0...
4	Paraxial		16.600			1.500 U	-	-	
5 IMAGE	Standard	Infinity	-			15.592	0.000	15.592	0.0...

Surf.Type	Maximum Term #	Norm Radius	Zernike 1	Zernike 2	Zernike 3	Zernike 4	Zernike 5	Zernike 6	Zernik
0 OBJECT									
1 (aper)	37	37.500	4.718	0.036	-0.234	2.805	-0.016	-0.118	-0.081
2 (aper)									
3 STOP									
4									
5 IMAGE									

FIGURE 3.1. Lens-Eye model layout in OpticStudio Zemax design software.

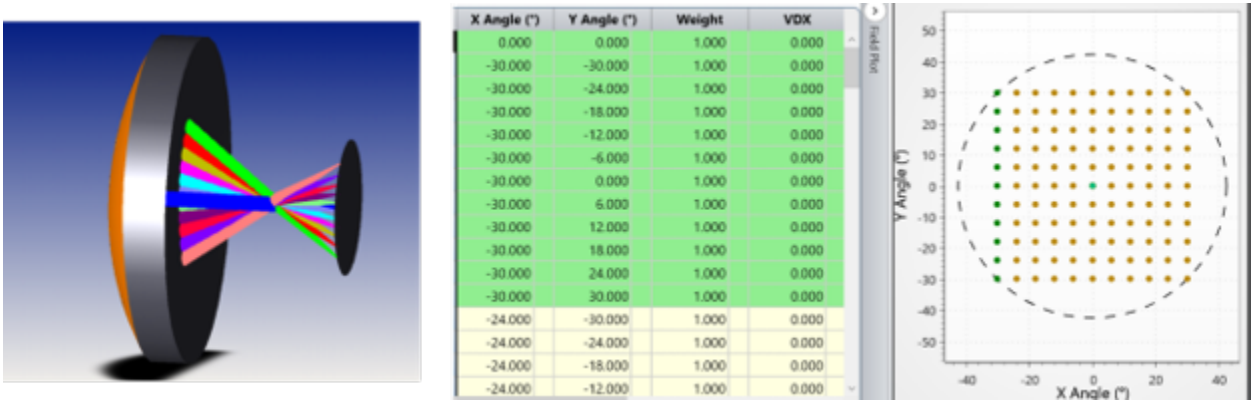


FIGURE 3.2. Lens-eye model used for point spread function calculation. The stop is at the center of rotation of the eye, 27 mm from the back vertex of the spectacle. The field of view is sampled with a Cartesian grid.

of the field. The number of .mat files matches the number of depths available to perform the simulation. The collection of .mat files, is the so called *psf* database.

### 3.3.2 Point Spread Function Interpretation

To understand progressive addition lenses behavior, a qualitative analysis of set of point spread functions for three different depths of field is presented. These planes, shown in Figure 3.3, represent far distance, intermediate distance, and near distance.

In far field region represented in Figure 3.3(a), the well-defined point spread functions at the top of the lens show that the best performance of the lens happens when the eye views distant objects through this region. At the bottom of the lens, however, the point spread functions have their energy distributed into the tails of the function, leading to a blurry image when viewing distant objects through this region. As expected, unwanted astigmatism also appears in the elongated point spread functions at the periphery of the lens.

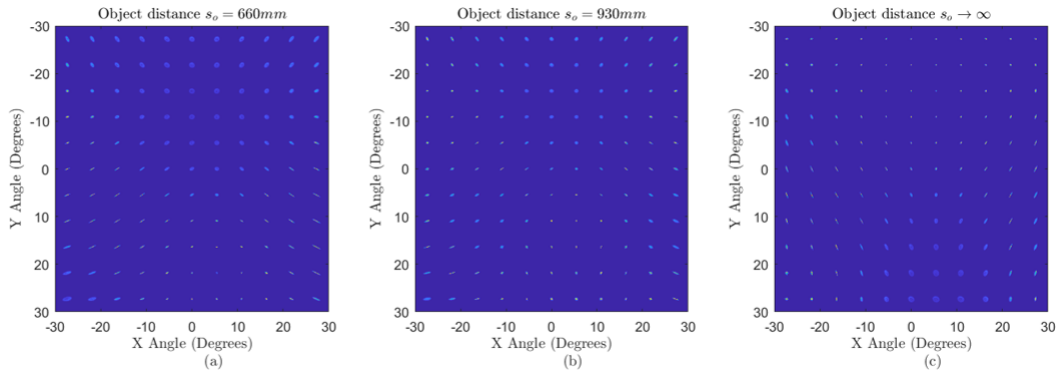


FIGURE 3.3. *psf* sampling for different object distances (a) Near Distance. (b) Intermediate Distance. (c) Far Distance.

The opposite effect happens when analyzing near region, represented by an object distance  $s_o = 600mm$  (Figure 3.3(c)). In this case, at the bottom of the lens, the *psfs* are sharp and well defined within a small region corresponding to approximately  $X$  angles of 0 to 10 degrees. Meanwhile at the top of the lens, the point spread functions size increases considerably in the near case. Again, enlarged astigmatic point spread functions appear at the edges of the lens. This means that when viewing near objects

through the lens, the eye has a narrow region in the lower portion of the lens where the image is sharp. However, the near objects would be blurry if viewed through any of the other regions of the lens.

At mid-distance, the well-defined point spread functions are located around the center of the lens, representing the corridor of the progressive addition lens. This corridor connects the upper distance viewing region with the lower near viewing region of the lens. Blurry *psf* regions are presented at the top, bottom and at the edges of the field of view.

This *psf* behavior can be related to results obtained in Chapter 2, by knowing that the optical power of an optical element is linearly dependent on the curvature of the surface. As shown previously in Figure 2.10(a), there is an increase of curvature towards the bottom of the lens. With more optical power at this lower region of the lens, closer objects are better focused when viewing through this part. Examples are shown later in this chapter.

### 3.3.3 Point Spread Function Scaling

Another fact to consider is that the point spread functions obtained from the Zemax simulation are images with the same dimensions in pixels ( $Nx_{psf} \times Ny_{psf}$ ), but with different pixel size in *mm*. Because a comparison between point spread functions and a bilinear interpolation will be performed, there is a need to have uniform size for all the elements when the database is created.

To scale all the point spread functions to the same size, a convenient size is chosen to cover the blurriest/biggest point spread function. This reference is chosen to be the on-axis field element from an object located at a distance  $d = 200mm$ . The size of this *psf* map is  $130 \times 130$  pixels. From raytracing code, the physical size of one pixel is obtained ( $\Delta x_{psf}$ ). Thus, the physical size in millimeters of the reference image can be calculated  $size_{ref} = Nx_{psf} \times \Delta x_{psf}$ .

As expected, the physical size of all the samples will be different. To match all sizes of these images, two actions were performed according the following conditions:

1. If  $size_{psf} > size_{psf-ref}$ , a pad operation is executed, inserting pixels to achieve the desired size.
2. If  $size_{psf} < size_{psf-ref}$ , a crop operation is executed, removing pixels to achieve the desired size.

where  $size_{psf}$  is the size in physical units of the point spread function under analysis. However, the number of pixels will differ between samples, and a uniform size is desired. After performing the described operations, it is safe to use the MATLAB function *resize*. This function applies an interpolation of the values to keep the size in *mm* but varies the sampling in pixels. Now, the physical size and the number of pixels will match, having accomplished the uniformity for the size in pixels and in physical units for all the point spread functions at different field and depth. Note that by using the largest anticipated *psf* as the reference image, the cropping done in action 2 above has minimal impact on the energy contained in all of the *psfs* within the database.

### 3.3.4 Point Spread Function Interpolation

Once the sampling and scaling is performed, the *psfs* are decomposed into a set of basis functions. These functions were chosen from adjacent fields of view. The *psf* functions between the basis functions are approximated by interpolating the expansion coefficients of the decomposition. Examples of seven regions for the distant object field are shown in Figure 3.4. These examples show different zones of the lens where similar *psf* functions are used for the interpolation. The interpolated *psf* is compared with *psfs* calculated directly from raytracing software for the same field point to provide a validation of the interpolation technique.

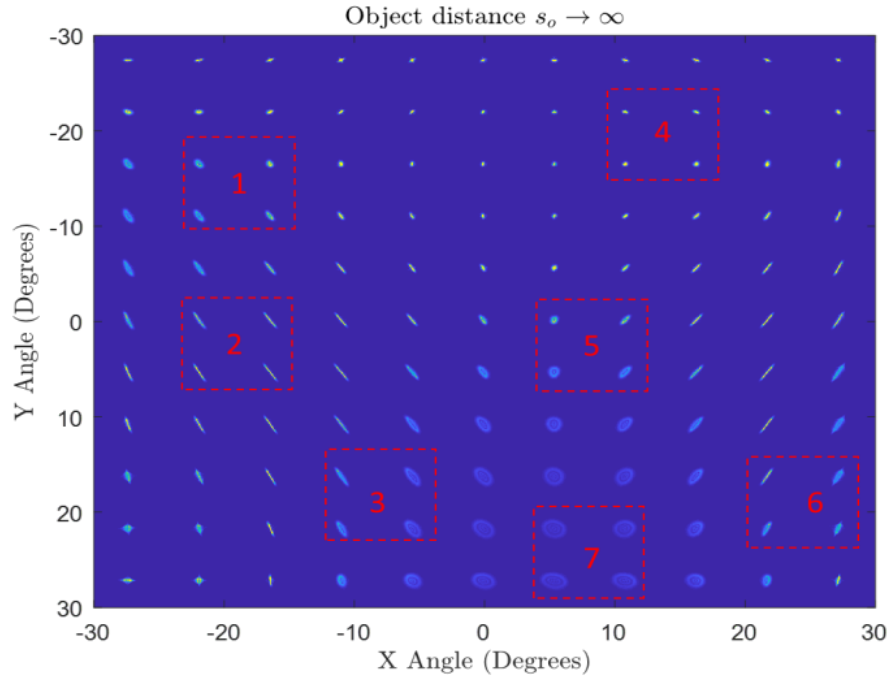


FIGURE 3.4. Examples of subsections of basis functions.

To complete bilinear interpolation, linear interpolation in one direction is performed, and then it is repeated in the orthogonal direction. One algorithm to write the interpolated function is explained as follows. Assuming  $psf_i$  is unknown, it is placed at the center of Figure 3.5 at coordinates  $(x, y)$ .

In this case,  $psf_{1,2}, psf_{1,1}, psf_{2,1}, psf_{2,2}$  are the basis functions, calculated previously from raytracing software and stored in the  $psf$  database. The interpolated function is found using Equation 3.3.1.

$$psf_i \approx a_0 + a_1x + a_2y + a_3xy, \quad (3.3.1)$$

where the coefficients are found by solving

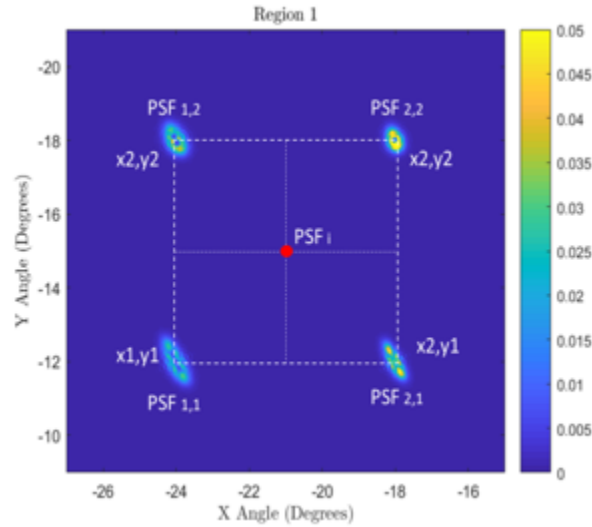


FIGURE 3.5. Bilinear interpolation example.

$$\begin{bmatrix} 1 & x_1 & y_1 & x_1 y_1 \\ 1 & x_1 & y_2 & x_1 y_2 \\ 1 & x_2 & y_1 & x_2 y_1 \\ 1 & x_2 & y_2 & x_2 y_2 \end{bmatrix} \begin{bmatrix} a_0 \\ a_1 \\ a_2 \\ a_3 \end{bmatrix} = \begin{bmatrix} psf_{1,1} \\ psf_{1,2} \\ psf_{2,1} \\ psf_{2,2} \end{bmatrix}. \quad (3.3.2)$$

The coefficients are given by

$$\begin{aligned} a_0 &= \frac{psf_{1,1} x_2 y_2}{(x_1 - x_2)(y_1 - y_2)} + \frac{psf_{1,2} x_2 y_1}{(x_1 - x_2)(y_2 - y_1)} + \frac{psf_{2,1} x_1 y_2}{(x_1 - x_2)(y_2 - y_1)} + \frac{psf_{2,2} x_1 y_1}{(x_1 - x_2)(y_1 - y_2)}, \\ a_1 &= \frac{psf_{1,1} y_2}{(x_1 - x_2)(y_2 - y_1)} + \frac{psf_{1,2} y_1}{(x_1 - x_2)(y_1 - y_2)} + \frac{psf_{2,1} y_2}{(x_1 - x_2)(y_1 - y_2)} + \frac{psf_{2,2} y_1}{(x_1 - x_2)(y_2 - y_1)}, \\ a_2 &= \frac{psf_{1,1} x_2}{(x_1 - x_2)(y_2 - y_1)} + \frac{psf_{1,2} x_2}{(x_1 - x_2)(y_1 - y_2)} + \frac{psf_{2,1} x_1}{(x_1 - x_2)(y_1 - y_2)} + \frac{psf_{2,2} x_1}{(x_1 - x_2)(y_2 - y_1)}, \\ a_3 &= \frac{psf_{1,1}}{(x_1 - x_2)(y_1 - y_2)} + \frac{psf_{1,2}}{(x_1 - x_2)(y_2 - y_1)} + \frac{psf_{2,1}}{(x_1 - x_2)(y_2 - y_1)} + \frac{psf_{2,2}}{(x_1 - x_2)(y_1 - y_2)}. \end{aligned} \quad (3.3.3)$$

To show the performance of the method, a grid of  $psfs$  in raytracing software is computed. The raytraced  $psfs$  at various points in the field are compared to the interpolated  $psfs$  at the same field location. Region 1 is used as example in Figure 3.6 to show interpolation between  $psfs$  that are clearly shift variant.

The  $psf$  at field  $(x, y) = (-21, -15)$ , comparable to the center of Region 1 is found by interpolation. This interpolated  $psf$  is compared to the one calculated at

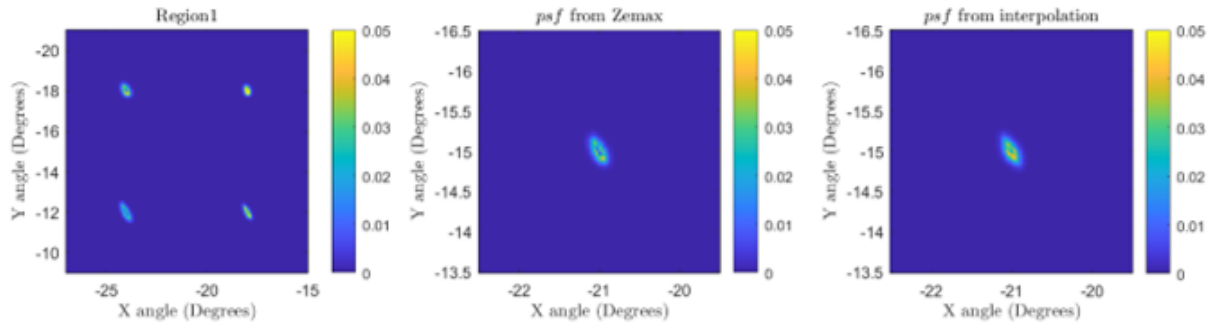


FIGURE 3.6. Region 1 analysis.

the same field using raytracing software. An RMS error of  $RMS = 0.00056$  or 1.6% of the relative irradiance is found in this case. The levels of these errors will depend on how the  $psf$  varies in the different regions analyzed. The difference between the point spread functions of this example is shown in Figure 3.7.

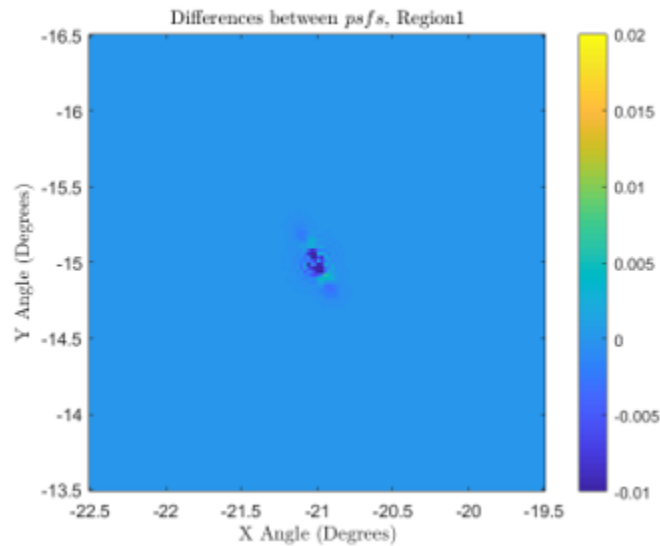


FIGURE 3.7. Differences between  $psf$  found by interpolation and  $psf$  found using raytracing code. The  $psf$  compared is at the center of Region 1,  $(x, y) = (-21, -15)$ .



The regions used as examples are summarized in Table 3.1. The table shows the coordinates of the *psf* position taken from the generated grid, which are the field coordinates of the interpolated *psf*. The *RMS* error and the absolute difference is presented.

Region	A (Upper Left Corner) (Degrees)	B (Upper Right Corner) (Degrees)	C (Lower Left Corner) (Degrees)	D (Lower Right Corner) (Degrees)	Field to find	RMS	Max abs Difference
1	-24, -18	-18, -18	-24, -12	-18, -12	-15, -21	0.00056	0.0210
2	-24, 0	-18, 0	-24, 6	-18, 6	-21, 3	0.00039	0.0076
3	-12, 18	-6, 18	-12, 24	-6, 24	-9, 21	0.00055	0.0121
4	12, -24	18, -24	12, -18	18, -18	15, -21	0.00051	0.0234
5	6, 0	12, 0	6, 6	12, 6	9, 3	0.00059	0.0181
6	24, 12	30, 12	24, 18	30, 18	27, 15	0.00066	0.0074
7	6, 24	12, 24	6, 30	12, 30	9, 27	0.00015	0.0017

TABLE 3.1. Examples of regions to analyze.

Figure 3.8 shows the four basis functions for the remaining six regions. As expected, the differences are dependent on the analyzed region, as shown in Figure 3.11. The change in shape of the *psfs* taken as the basis functions to interpolate the new one is related to the differences obtained. A comparison between the ray-traced and the interpolated *psfs* for each region are shown in Figure 3.9 and Figure 3.10. A more significant *RMS* error is found when the point spread function lacks similarity with its neighbors. In Figure 3.11(f), the four-point spread functions used to interpolate the intermediate points in region 7 are almost isoplanatic. In contrast the *psfs* in Region 6 that have a considerable change. Each *psf* shows astigmatism, but the two *psfs* on the left are at a tight line focus, whereas the two *psfs* on the right have additional blurring. The results show that the interpolation works worse when there is a quick change of the *psf* between regions. To decrease this error, the

distance between sampled points should decrease. Conceptually, the sampling could be non-uniform where a similarity metric is created for the groups of four *psfs* and for similar groups, the sampling frequency is maintained, while for dissimilar groups, the sampling region is further sub-divided.

The differences between the interpolated point spread functions of these regions and the ones obtained in raytracing code are shown in Figure 3.11.

### 3.3.5 Point Spread Function Scaling

One important consideration when performing realistic simulations, is having congruence in size between the *psf* and the scene to simulate. A technique for finding a scaling parameter to match the angular size of the point spread function with the field of view (*FOV*) of the realistic scene is explained. Once all the point spread functions in the database are uniform in size, the angular subtense of one pixel in the *psf* map can be computed. Since every pixel in the picture to simulate must correspond to one pixel in the *psf*, a scaling factor that meets this condition has to be found.

The angular size of an object is defined as the angle that an object subtends at the viewer distance. It is computed as the object size in distance units over the distance of observer. As explained in detail in the following section, all pictures representing the scene to simulate have a field of view of  $FOV = 60^\circ$ . By knowing the image size in pixels,  $Nx \times Ny$  with  $Nx = Ny$ , the angular size in degrees of one pixel in the picture is found

$$\alpha_{scene} = \frac{FOV}{N_x}. \quad (3.3.4)$$

A pixel with size  $\Delta X$  is located a distance  $d$  from the front nodal point of the eye, subtends an angle  $\alpha_{scene}$ . The image plane is located at the eye focal length  $f_{eye} = 16.6mm$ , distance from the rear nodal of the eye to the retina. Figure 3.12 illustrates a simplified view of the eye imaging. The *psf* size in pixels,  $Nx_{psf}$ , and

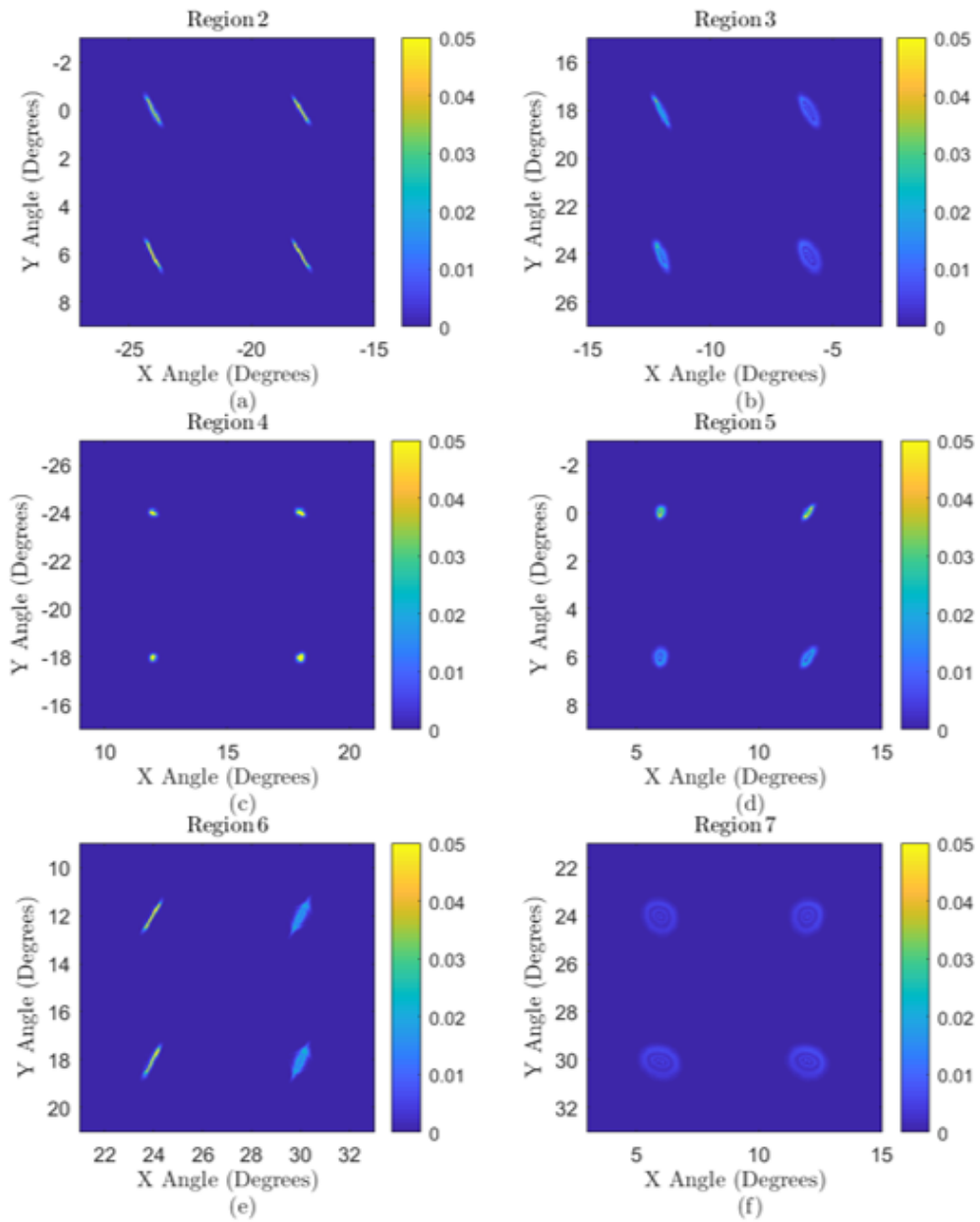


FIGURE 3.8. Examples of different regions for far field, where the Point Spread Function differs in function of glaze angle.

the  $psf$  pixel size in distance units,  $\Delta X_{psf}$ , are the same for all different depths as explained previously in Section 3.3.3. Therefore, the  $psf$  angular size in degrees  $\alpha_{psf}$

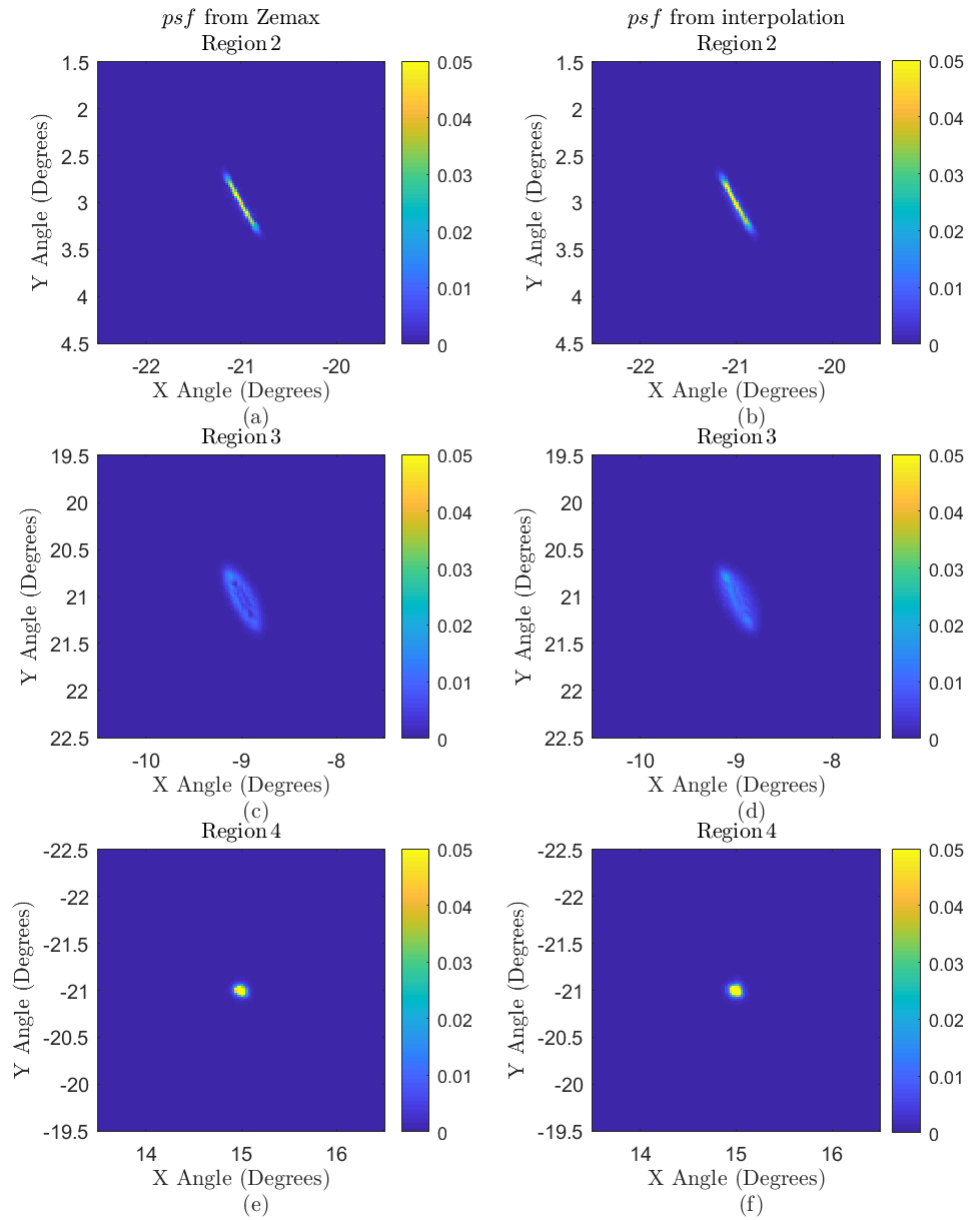


FIGURE 3.9. Interpolated  $psf$  and the  $psf$  obtained with raytracing for Regions 2, 3 and 4.

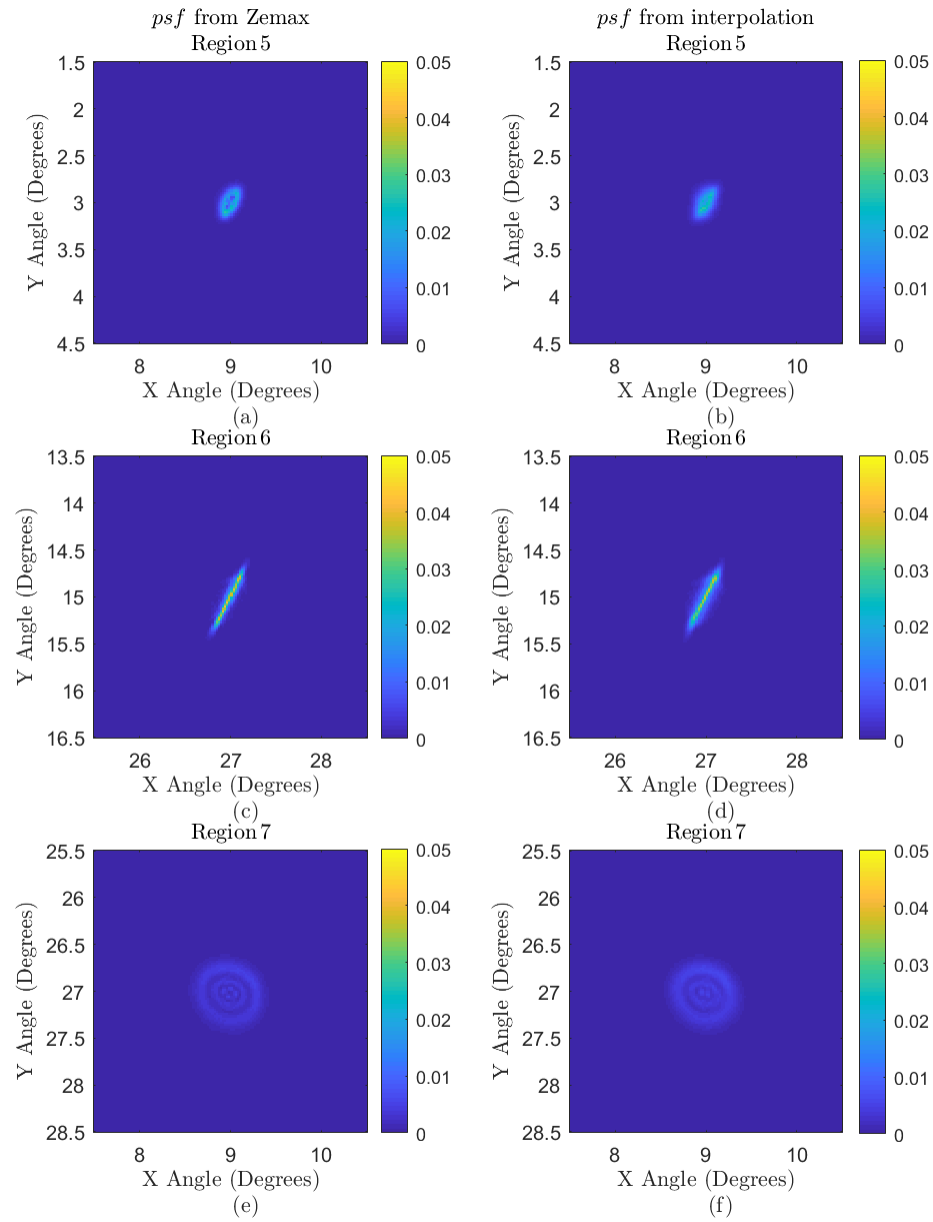


FIGURE 3.10. Interpolated *psf* and the *psf* obtained with raytracing for Regions 5, 6 and 7.

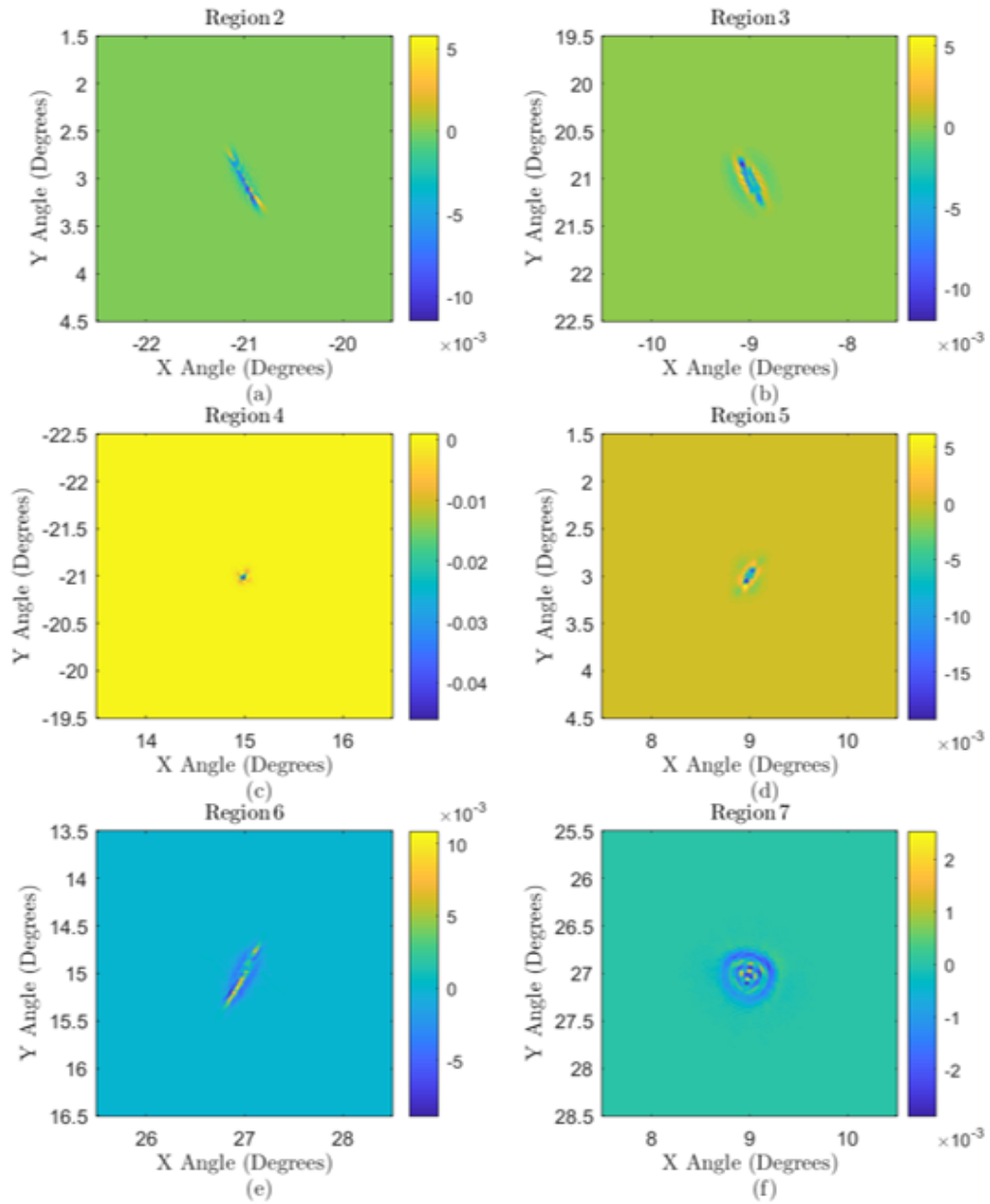


FIGURE 3.11. Differences of extrapolation and  $psf$  obtained using Zemax.

is given by

$$\alpha_{psf} = \frac{\Delta X_{psf}}{f_{eye}} \times \frac{180}{\pi}. \quad (3.3.5)$$

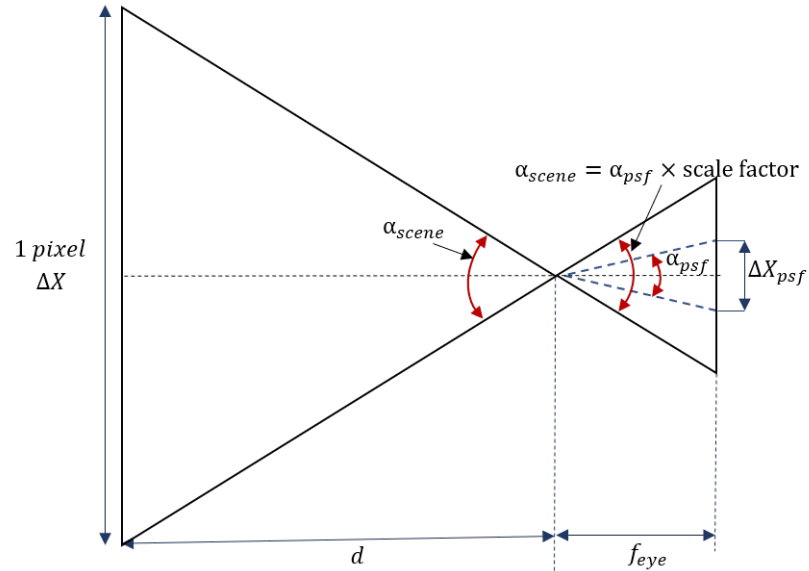


FIGURE 3.12. Angular relation between pixel angular size and point spread function angular size.

By knowing, the angular size of one pixel in the scene, and the angle that subtends one pixel in the *psf*, the unknown factor needed to match  $\alpha_{psf}$  and  $\alpha_{scene}$  is found

$$scale\ factor = \frac{\alpha_{scene}}{\alpha_{psf}}, \quad (3.3.6)$$

$$scale\ factor = \frac{f_{eye} \times FOV}{\Delta X_{psf} \times Nx} \times \frac{\pi}{180}. \quad (3.3.7)$$

To find the new *psf* size in pixels,  $Nx'_{psf}$ , the original *psf* is divided by scale factor.

$$Nx'_{psf} = \frac{Nx_{psf}}{scale\ factor}. \quad (3.3.8)$$

In this work,  $f_{eye} = 16.6mm$ ,  $FOV = 60^\circ$ ,  $\Delta X_{psf} = 0.0024mm$ , and  $Nx = 1296$  *pixels*, and  $Nx_{psf} = 23$  *pixels*, obtaining a new *psf* size of

$$Nx_{psf} \approx 23 \text{ pixels.} \quad (3.3.9)$$

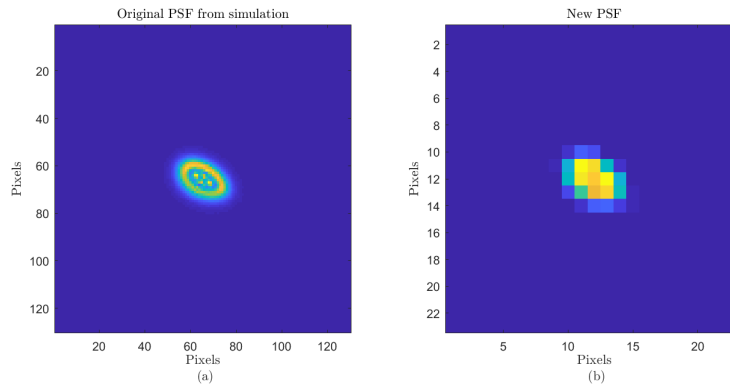


FIGURE 3.13. Comparison of the interpolated *psf* based on the *psf* database and its down-sampled version created to match the angular subtense of pixels in the simulation scene.

Figure 3.13 shows a comparison of an interpolated *psf* based on the *psf* database and its down-sampled version which is created so that the angular subtense of each *psf* pixel now matches the angular subtense of the pixels in the scene to be simulated. This downsampling also has the effect of reducing the errors associated with the interpolation process since small differences in the fine structure of the *psf* are merged into a single pixel in the downsampled version.

Until now, the considerations to create the *psf* database have been explained. In the following sections, the considerations for the scene to simulate will be treated in detail.



### 3.4 Realistic Simulation

In this dissertation, computational imaging is used to create a real scene simulation as seen through a progressive addition lens. Computational imaging is image formation that requires digital computer techniques [43]. A captured image is used that after image processing will provide insight of how the patient will see through an ophthalmic correction for presbyopia.

Several attempts have been done to simulate realistic scenes through the eye optical system. One method uses the concept of Depth Point Spread Function (DPSF). Each DPSF is a histogram of rays normal to the wavefront from a patient eye obtained using a Shack Hartmann sensor. These DPSFs are defined at different depths and they are in object space. After obtaining the DPSFs, depth images of the scene to simulate are created. The depth images are convolved with the corresponding DPSF, that are assumed to be isoplanatic. After convolution, the depth images are composited into a single vision-realistic image [44].

Another attempt to simulate scenes through progressive addition lenses is with the construction of a tri-dimensional *psf* matrix. Each *psf* is dependent on the angle of gaze and on the object depth. With this information, a trilinear interpolation is performed to find the *psf* at each pixel. Because of computational time the assumption that the *psf* is the same for a pixel area is made. The scene is decomposed into the RGB channels and each *psf* is weighted by the pixel value. the final image is obtained with a superposition of the resultant images. The simulated images are for a field of view of  $FOV = 20^\circ$  [45].

In this work, the method proposed uses a *psf* grid found for different depths using raytracing code. Each point spread function is calculated for each pixel.

The image to simulate must represent the eyes field of view  $\pm 30^\circ$ . Once this condition is accomplished, it is safe to assume that every pixel in the image will match the pixel angular size in the *psf* map.

The image will be taken with a Samsung Gear 360 Camera. This camera uses a CMOS sensor of  $8.4MP \times 2 F2.2$  lens  $360^\circ$  Dual Lens: up to  $15MP$  ( $5472 \times 2736$ ) Single Lens: up to  $3MP$  ( $2304 \times 1296$ ). It is shown in Figure 3.14.



FIGURE 3.14. Samsung gear 360 Camera

The camera was chosen because it covers a wide field of view, that can capture the head movement at different parts of a real-world scene. For this work, in order to show the algorithm performance, only one lens was used.

### 3.4.1 Wide Field Angle and Distortion

A scene with three different object depths is created. It consists of three planes. The first plane is a cellphone, representing a near object. The second plane is a computer screen that represents an intermediate object distance. Finally, a plane is represented by distant objects. Images are captured with the Samsung Gear 360 camera, and the final image dimensions is  $2304 \times 1296$ . An example of one of the raw images taken with the camera is shown in Figure 3.15.

As is readily apparent in Figure 3.15, this camera has a fish eye lens. These types of lenses have two important characteristics that impact this work. First, as mentioned previously, these lenses can achieve a full field of view. However, to achieve this convenient feature, these lenses also introduce high levels of distortion. The form



FIGURE 3.15. Example of scene with three object depths taken with the Samsung Gear 360 camera.

of the distortion introduced is barrel distortion. To use the image from this camera system in the simulations, a camera calibration is needed. Such a calibration has already been developed for fish eye lenses [46]. This process consists of determining the intrinsic parameters of the camera. To correct for distortion, the distortion coefficients are typically needed.

The free software GIMP 2, was used to undistort the image to simulate. This image manipulation software allows us to correct main and edge distortion. In this software, main distortion refers to the amount of spherical correction introduced in the image. Edge distortion is the amount of spherical correction introduced at the edges of the image. If the value of distortion is positive the software makes the image convex, as shown in Figure 3.16. On the contrary if the value is negative, the software makes the image concave [47]. The different effect applying the same amount of edge and main distortion is shown in Figures 3.16 and 3.17.

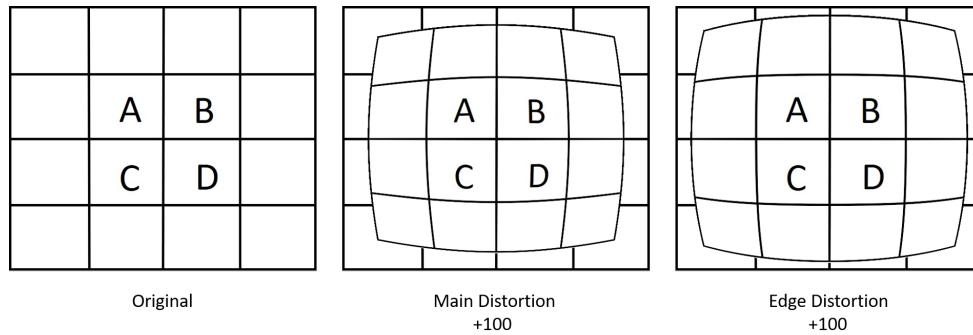


FIGURE 3.16. Example of a grid with positive main and edge distortion applied.

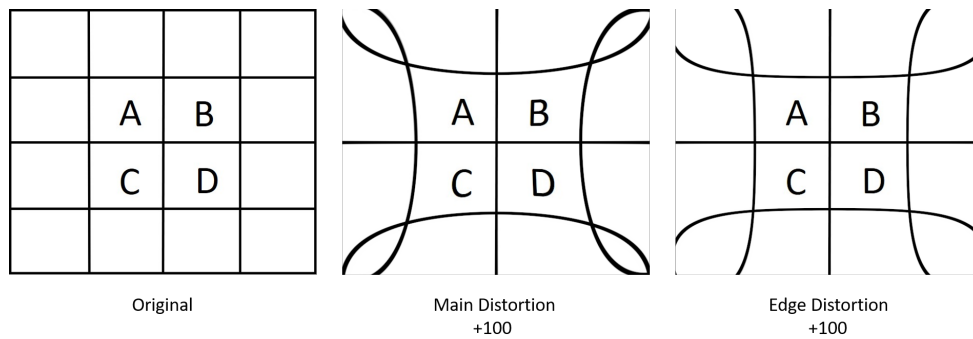


FIGURE 3.17. Example of a grid with negative main and edge distortion applied.

After finding the optimal parameters, or amount of each distortion type to add. This filter was applied to the images used for the final simulation. The undistorted image for the example shown before, is shown in Figure 3.18. This was an image undistorted using GIMP 2 software, with values of *maindistortion* =  $-90$  and *ledgedistortion* =  $+26$ .

### 3.4.2 Image Size

As mentioned in section 3.3.5, the field of view covered by the scene must match the field of view of the eye modeling done previously so that the angular size of one pixel

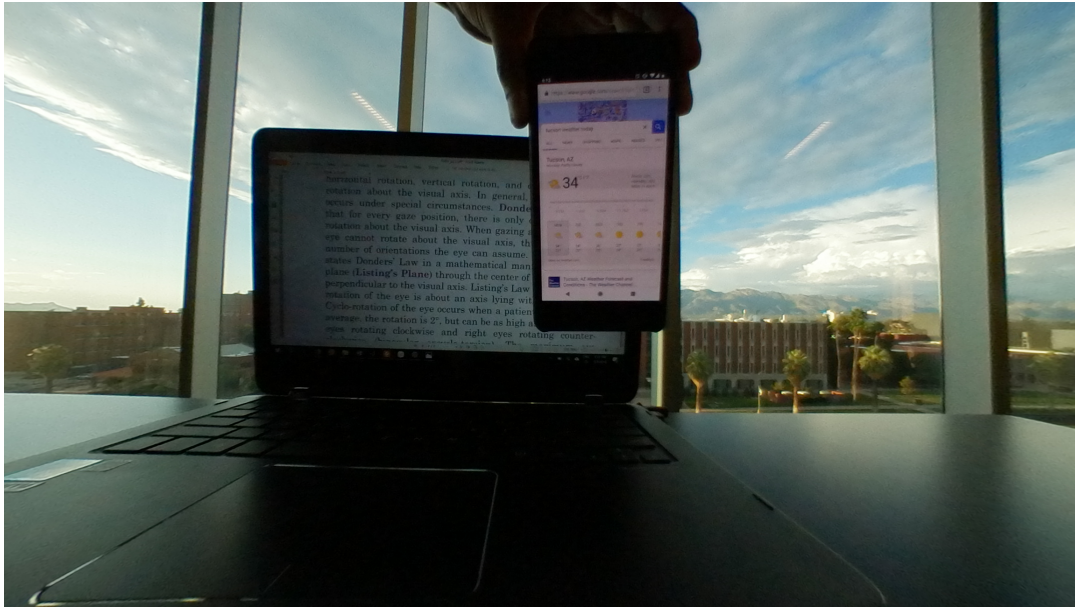


FIGURE 3.18. Example of undistorted scene using GIMP image manipulation software, with three object depths taken with the Samsung Gear 360 camera.

in the image matches the angular size of one pixel in the  $psf$  map from the database. To find the part of the image covered by a  $FOV = 60^\circ$ , the process described below is used.

Starting from the fact that the picture size is equal to  $Nx \times Ny$  pixels. The first step is to homogenize both sizes,  $Nx = Ny$ , in such manner that the horizontal and vertical field of view are the same. The size chosen to crop the image would be the smallest one, in this case  $Ny$ , resulting into a square image.

By knowing the physical dimensions of one object in the scene and the number of pixels that corresponds to the same object in the picture, the pixel size in units of distance  $\Delta X$  is found. The viewer distance corresponds to the distance from the object to the camera  $d$ . With this information, the angular subtense of one pixel is computed.

Taking as example the picture shown in Figure 3.19, the object known is the

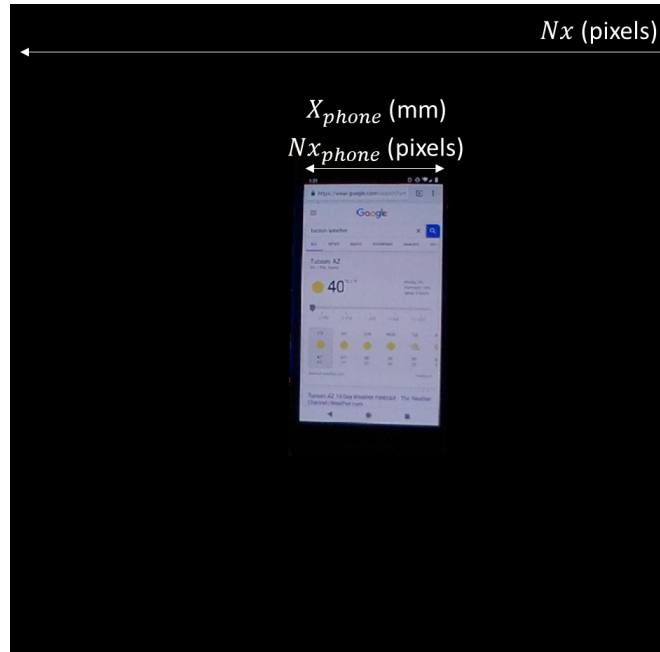


FIGURE 3.19. Cellphone picture taken at  $d = 200mm$  from camera.

cellphone, then

$$\Delta X = \frac{X_{phone}}{Nx_{phone}} = \Delta Y, \quad (3.4.1)$$

where  $X_{phone}$  is the cellphone size in millimeters and  $Nx_{phone}$  is the number of pixels that corresponds to  $X_{phone}$ . By knowing the pixel size and the distance from object to camera  $d$ , the angular size of one pixel  $\alpha_{scene}$  was computed

$$\alpha_{scene} = \frac{\Delta X}{d}, \quad (3.4.2)$$

with the information found, the field of view of the whole picture is given by

$$FOV_{scene}(Degrees) = (N_x \times \alpha_{scene}) \times \frac{180}{\pi}. \quad (3.4.3)$$

The visual field for the human eye model is approximately  $FOV_{eye} = \pm 30$  degrees. To assure that all the picture represents  $60^\circ$ , the image is cropped to the appropriate

size. This is an important step because *psfs* are calculated to start at  $-30$  degrees for the first pixel in the image. Obviously, larger fields of view and non-square fields of view could be used in the simulation by modifying the *psf* database to include *psfs* from these higher field angle. However, due to the dimensions of the spectacle lens, some of these fields might lie outside the aperture of the lens. Consequently, the field of view was restricted to  $60$  degrees in these simulations to ensure that the spectacle lens covered the full range of fields.

Figure 3.18 is taken as an example. For this case  $Nx = 1296$  pixels. From Equation (3.4.2), the angular size of one pixel is found  $\alpha_{scene} = 0.0634^\circ$ . The computed field of view is equal to  $FOV_{scene} = 82^\circ$ . Therefore, the difference in degrees is

$$N_{dif}(Degrees) = FOV_{scene} - FOV = 22 \quad (3.4.4)$$

To convert  $22^\circ$  to pixels, Equation (3.4.5) is used. The angular size of one pixel is already known,

$$N_{dif} = FOV_{picture} - FOV (pixels) = \frac{(FOV_{picture} - FOV) (Degrees)}{\alpha_{pixel} (Degrees)} = 347 pixels. \quad (3.4.5)$$

Consequently, the new picture size  $Nx'$  is given by

$$Nx' = Nx - N_{dif} = 1296 pixels - 347 pixels = 949 pixels, \quad (3.4.6)$$

$$Nx' = 949 pixels. \quad (3.4.7)$$

However, if the cellphone changes distance relative to the camera, the angular size of one pixel will change. Thus, by changing the distance  $d$ , if  $FOV_{picture} > FOV_{eye}$ , the same procedure must be followed to match a  $FOV = 60^\circ$ .

On the contrary, if  $FOV_{picture} < FOV_{eye}$ , instead of cropping the image, a padding operation will be performed. After scaling the images to the same field of view, a

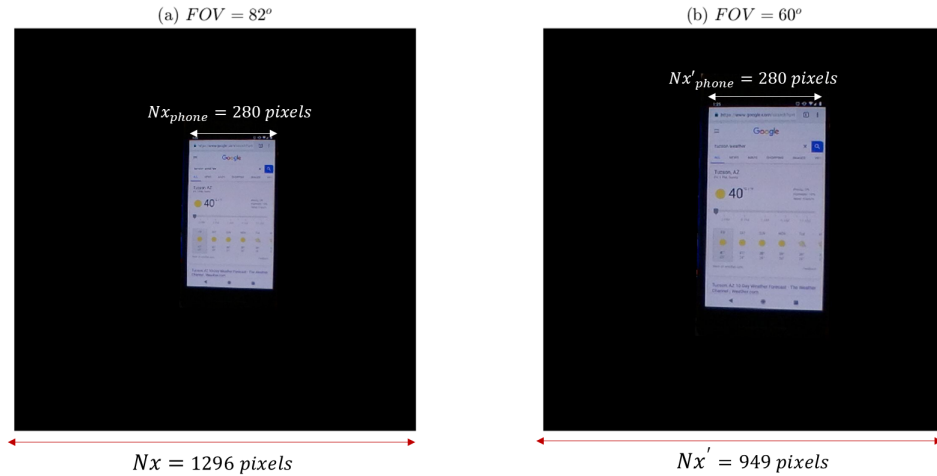


FIGURE 3.20. (a) Original Picture  $FOV = 82^\circ$ ,  $Nx = 1296$  pixels (b) Cropped Picture  $FOV = 60^\circ$ ,  $Nx' = 949$  pixels.

resize of the images is performed, so that all the images have the same number of pixels.

Examples of the cellphone at different distances from the viewer are shown in Figure 3.21. As expected, the angular size changes inversely proportional to the observer distance. The total angular size of a closer object is bigger than the angular size of the same object at a far distance.

### 3.4.3 Image Segmentation and Depth of Field

In real-world, objects are located at different distances from our eyes, so every object has different depth. To analyze progressive addition lenses, creating scenes with these multiple depths is an important feature because the psfs change considerably between planes, looking at the same field angle. In Figure 3.22, the change is appreciable for the same part of the lens depending where the object is.

As a consequence, every object in the scene located at a certain depth has to be



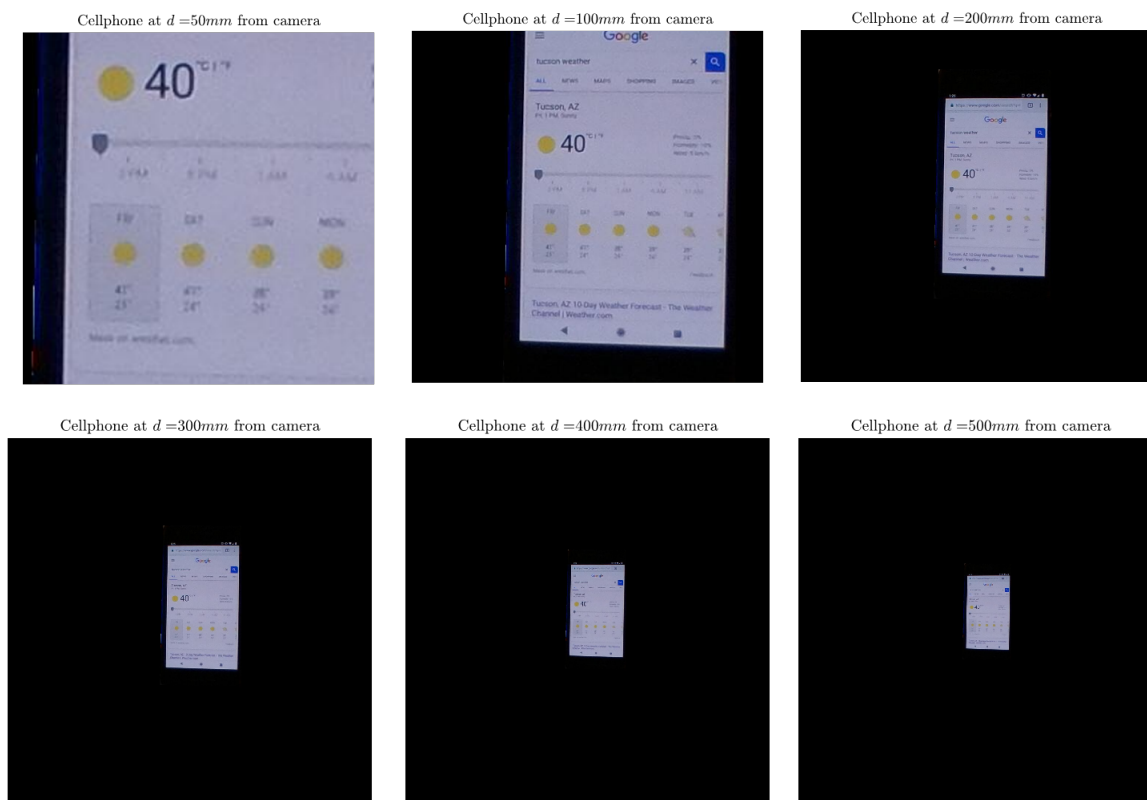


FIGURE 3.21. Examples of the cellphone at different depths. Everything relative assuming a field of view  $FOV = 60^\circ$  equal at  $N_x = 1296$  pixels.

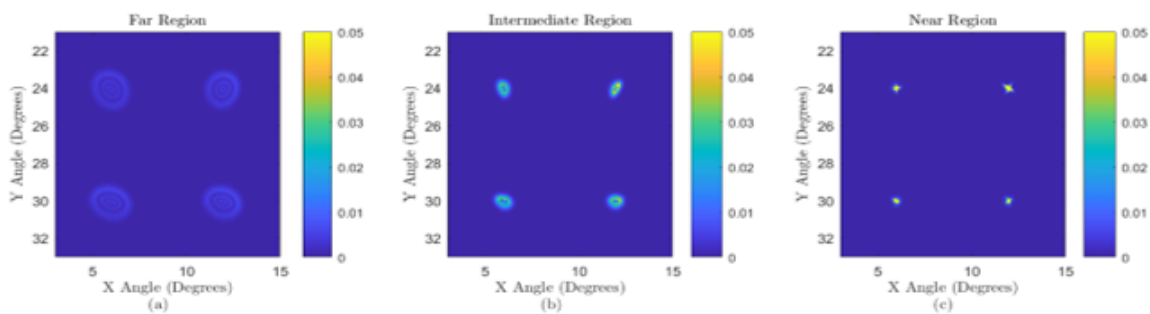


FIGURE 3.22. Basis functions in Region 7, at three different object depths.

simulated using the *psfs* calculated at the correspondent depth. In the *psf* database, *psfs* for different depths are collected. Nevertheless, a measure to separate the scene into different depth planes is performed for the simulation. The objects in the scene are simulated to be planar at their respective depths. This approximation is reasonable since the cellphone and laptop screen are planar and the distant landscapes can effectively be treated as being at infinity with regards to the camera.

To demonstrate how each plane is seen through the lens at different distances from the observer, the algorithm outlined previously is used for the same image. The scene was divided in three different depths, at the top far distance, at the center intermediate distance and at the bottom near distance. In image shown in Figure 3.23, it is noticeable that at the near object region, astigmatism is presented at the edges of the bottom part of the lens, and the letters are sharper at the center bottom part. Analyzing the distant power portion of the lens, all the top part of the image is now in focus. The progressive corridor is appreciated, by the r and s letters that are the representation of objects at mid-distance.



FIGURE 3.23. Simulation of the same object at different planes of the scene.

As mentioned in Section 3.4.1, a scene with three different depths of field is created.

In this way, the distance to the objects was known. Thus, the procedure to isolate different planes consists of masking the objects to isolate them into their appropriate depth plane. In this work, masking means to identify the region of interest and assign a zero value to the rest of the image. After performing this action, the masked image is saved.

The masked images used for this work are shown in Figure 3.24. These images were undistorted and rescaled as described previously, and every image represents a  $60^\circ$  field of view. Having the planes separated, the algorithm described in Section 3.2 is applied and then the images are recombined to get the final simulation. This process is explained with more detail in the following section.

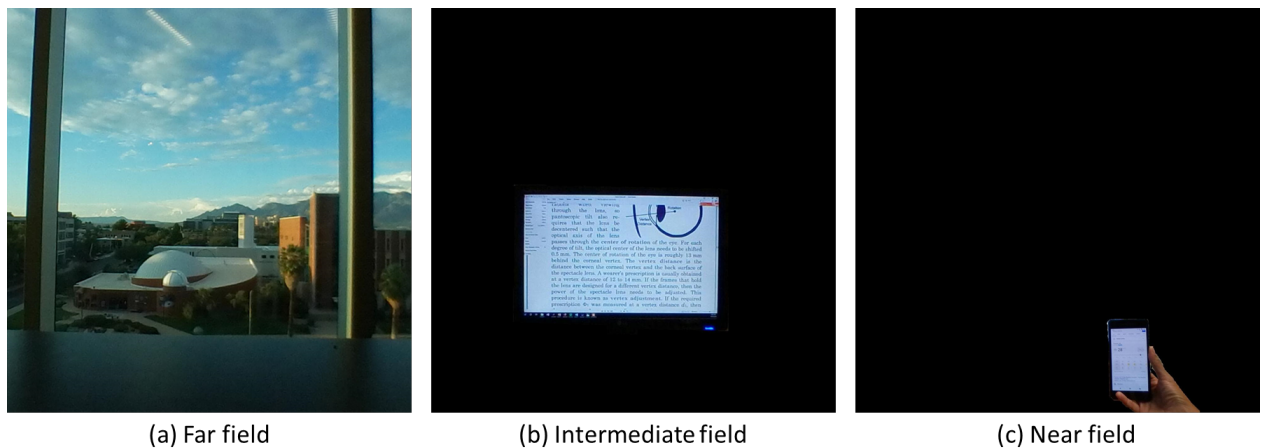


FIGURE 3.24. Masked images at different depth planes.

### 3.4.4 RGB Color Model

The physiology of the eye includes three color receptors called cones. These cones can perceive red, blue and green, a combination of these colors described the color world that we see. Digital representation of an image is based on the principle of human perception of color. Digital images have individual pixels that are RGB (red,

green and blue). The combination of these colors reproduces a large range or gamut of colors in a display [48].

In this work, a color scene is used. Each pixel is represented by three values, red, green and blue. Because the proposed method consists on scaling the *psfs* corresponding to one pixel with the respective value, the image is divided into its three-color channels, and each channel is processed by the algorithm separately. Conceptually, the psf database could be created with *psfs* corresponding to red, green and blue wavelengths. However, for this simulation only monochromatic *psfs* are used. The eye inherently has a high level of chromatic aberration, with nearly 2 diopters variation in power across the visible spectrum. The visual system has a remarkable ability to suppress the chromatic aberration of the eye and color fringing effects are rarely noticeable to people. Consequently, the dispersion associated with the spectacle lens material is ignored in the simulations without much impact on the results.

Figure 3.25 is an example of a digital color image. As it was explained before, this can be decomposed into three different channels.

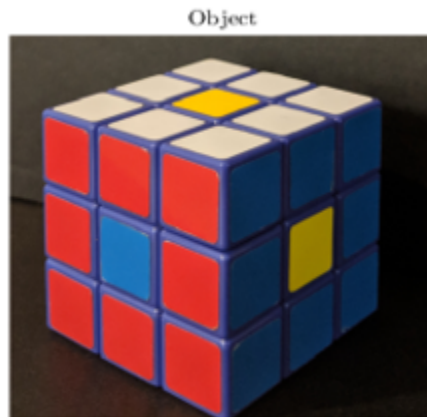


FIGURE 3.25. Color Object.

The decomposition into three color channels of this image is shown in Figure 3.26. Now, each image has only one value per pixel, and the proposed simulation method

is applied for each channel separately.



FIGURE 3.26. Object decomposed in three RGB channels.

### 3.5 Algorithm Implementation

Until now, different aspects have been considered to prepare the point spread function database and the image to simulate. Now that everything is ready, the MATLAB Script is applied to the image. Knowing that each pixel in the image represents a fraction of the  $FOV_{eye} = 60^\circ$ , the program searches the corresponding *psf* for each pixel in the *psf* grid. If the *psf* does not exist, bilinear interpolation is performed as previously described.

The pixel value from the scene image is read, and the point spread function is weighted by the value for each color channel.

The point spread function is represented by an array of pixels, so that the adjacent pixels of the current pixel under study are affected by the tails of the *psf*. To take into account this contribution, all the contributions from the various *psfs* (either directly or from the tails of adjacent *psfs*) are summed to get the final pixel value. A graphic representation of this step can be found in Figure 3.29.

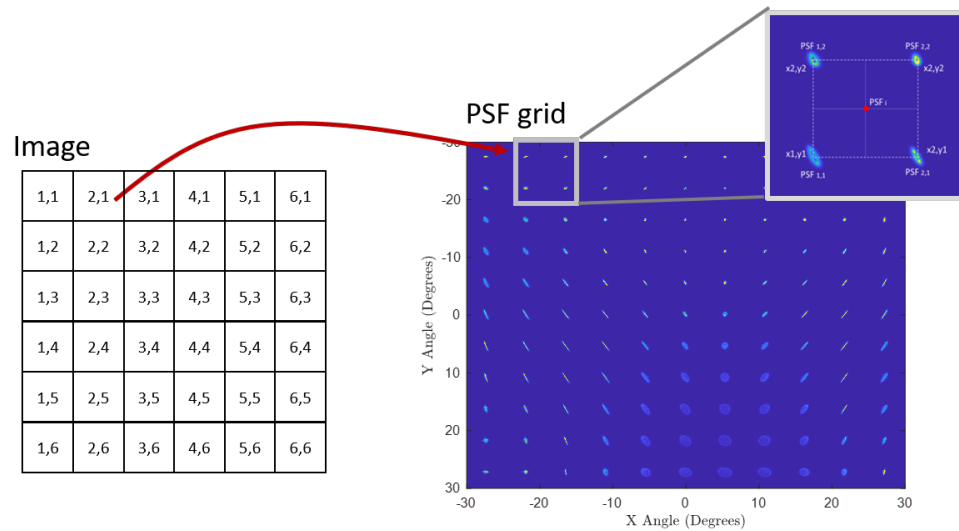


FIGURE 3.27. Graphic representation of the first step of the algorithm applied. The *psf* that corresponds to a determined pixel in the image is searched, if the *psf* does not exist, interpolation is performed.

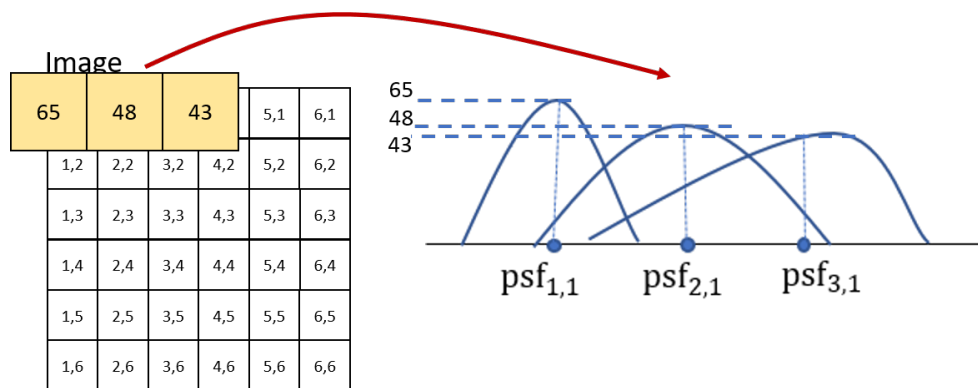


FIGURE 3.28. Graphic representation of the second step in the algorithm applied. The *psfs* are weighted by the correspondent pixel value.

This process is repeated for each color channel. The results are stored in a single matrix. Therefore, each matrix represents one RGB channel. The matrices are then recombined to obtain the final RGB image.

The results of image simulation with three object depths are described in the

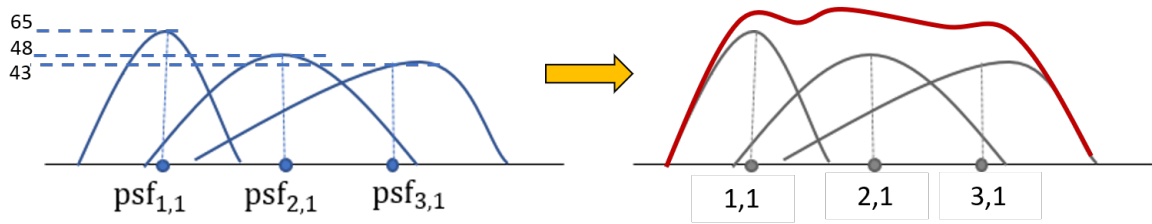


FIGURE 3.29. Graphic representation of the third step in the algorithm applied. Contribution of  $psfs$  at each pixel are summed to get the final value for each pixel.

following section. The simulated scene is from the point of view of a person looking out a window, while working at a laptop computer and viewing a cellphone. Since the cellphone distance can be moved, images from the same scene moving the cellphone closer and further away are shown.

## 3.6 Results

Assuming the far objects are at  $d_{inf} \rightarrow \infty$ , the intermediate object of the laptop screens is at  $d_{mid} = 930mm$  from the camera, and the near object of the cellphone is at variable distances of  $d_1 = 200mm$ ,  $d_2 = 300mm$ ,  $d_3 = 400mm$ ,  $d_4 = 500mm$ , and  $d_5 = 660mm$ .

### 3.6.1 Results for Three Different Regions

The pictures shown in Figure 3.24 are used as the base images in the simulation. Each picture is decomposed into RGB channels, and the  $psf$  corresponding to the respective object distance is found. The image size in pixels is  $N_x \times N_y = 1296pixels \times 1296pixels$ . Therefore, from Equation 3.3.9 the  $psf$  size is  $23 \times 23pixels$ . Before recombining the images, the result for each depth is shown in Figure 3.30.

The resultant images for near objects are obtained by using the images shown in Figure 3.32 and the corresponding set of  $psfs$ . As expected, the sharpest image is

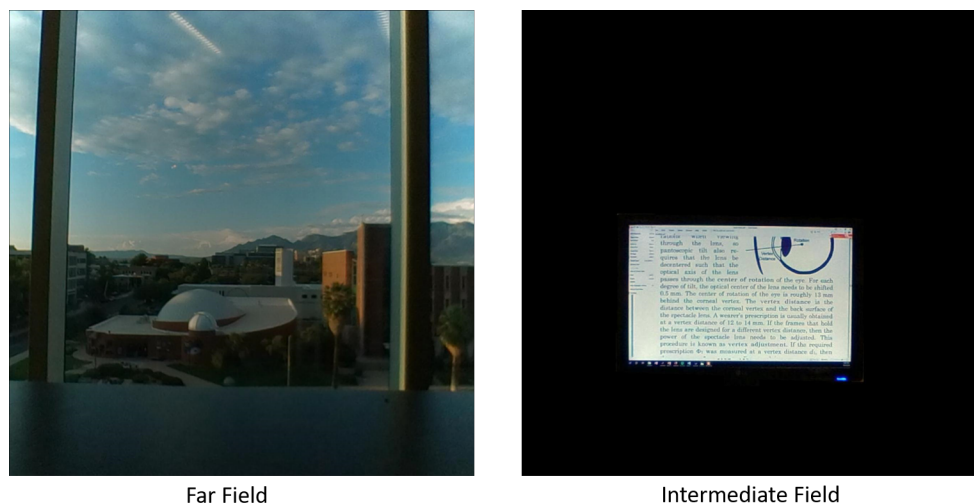


FIGURE 3.30. Simulation results for Far Field and Mid-Field.

the one representing the object at a distance  $d = 660\text{mm}$ , this distance matches the prescription for near zone of the PAL.

To better appreciate the effect of the progressive addition lens at different distances, the region with legible print was selected, and a comparison of the same letters are shown in Figure 3.32. The letters are blurriest and the contrast is reduced when the cellphone is closer to the observer. When the cellphone is at the prescribed distance, the letters are sharp.

### 3.6.2 High Performance Computer

The algorithm has to be executed one time for each scene depth per RGB channel. Taking into account that the computational time will depend on the number of pixels of the image, and the *psf* map size. The required time to perform a simulation increases considerably even for modest dimensions for these variables. Due to the amount of simulations required to show the effects of a progressive addition lenses, and the number of pixels of each image, a personal computer was inadequate to



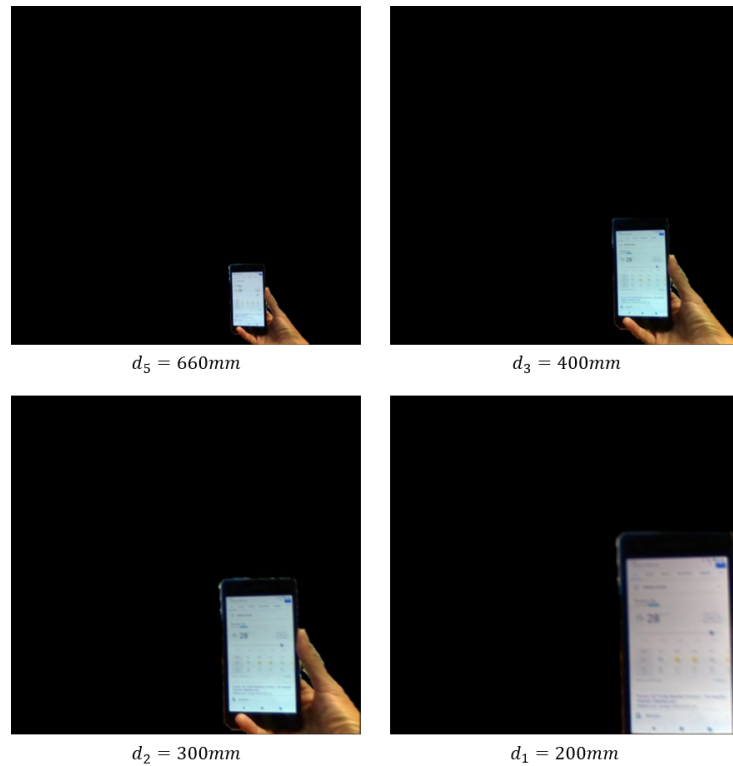


FIGURE 3.31. Simulation results for different Near Field distances.

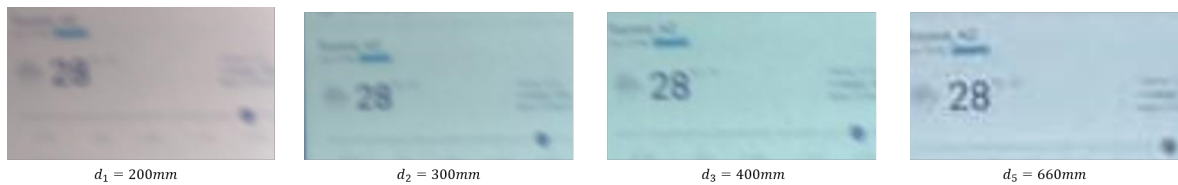


FIGURE 3.32. Comparison of Near Field visual performance.

perform these calculations in a timely fashion. Consequently, other means were used to complete the simulation.

One useful resource at The University of Arizona is the availability of a High Performance Computer (HPC) cluster. This resource is available for students and professors associated to the University of Arizona. Due to the computation time of

the simulations, the HPC was used to perform the simulation for different regions at different depths in parallel.

The computer resource used for these simulations is the Ocelote. It has 46 new compute nodes with Nvidia P100 GPU's [49].

Although the time per scene was around 24 hours, the advantage of using this computer is that the calculations can run in parallel, so instead of waiting 7 days per 7 images, the waiting time was 1 day for all the images.

### 3.6.3 Final Simulation

After the algorithm was applied to all of the images, the results for near, intermediate and far field were superimposed to get the final image. The resultant images are shown in Figure 3.33 and 3.34.

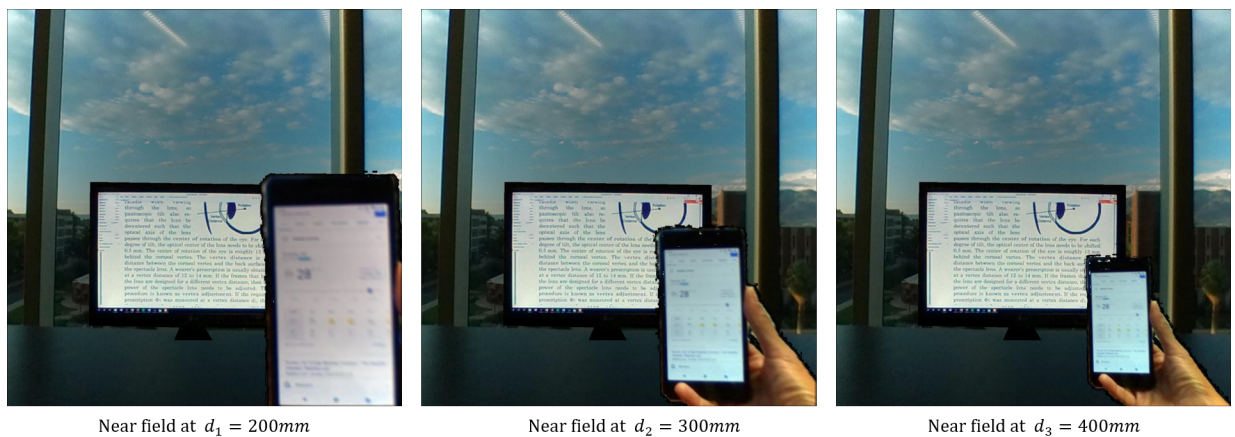


FIGURE 3.33. Complete simulated 3 depths scene for Near field  $d_1 = 200mm$ ,  $d_2 = 300mm$  and  $d_3 = 400mm$ .

By recombining the images some problems became visible. The edges from images at different distances, are not smooth. To avoid this problem an alpha blending technique has been previously used [13]. In general terms, this technique takes the boundaries of the objects and assigns a transparency values between 1 and 0 (white

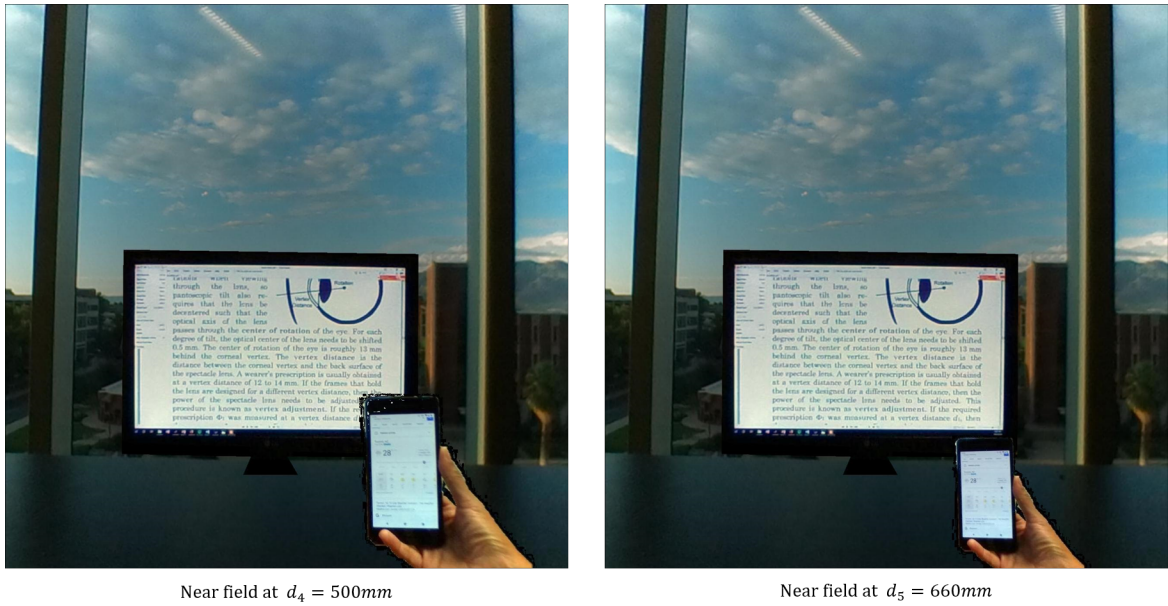


FIGURE 3.34. Complete simulated 3 depths scene for Near field  $d_4 = 500mm$  and  $d_5 = 660mm$ .

and black). Even though alpha blending is not a physical phenomenon, this operation results in a color blending at the edges which gives a more realistic appearing result.

As shown in Figure 3.33 and 3.34, simulations of multifocal vision have been successfully performed. With the creation of the psf database, final simulations were obtained at different depths and gaze angle of the wearer. These images could give a preliminary insight of the perception of the world when looking through different parts of a progressive addition lens. This fact is useful to explain that new eye movements and head movements have to be learned to take advantage of this ophthalmic artifact.

The simulated images show congruence between the freeform shape obtained in Chapter 2 with the ideal performance of a progressive addition lens. Unwanted aberrations at the edge of the lens are visible and may impact on the wearer decision to use PALs.

In this dissertation simulation of multifocal vision of one PAL is performed to

show the performance of the method. However, the approach used can be generalized for different lenses with different prescriptions, field of view considered, and objects at different depths. Computational time can be reduced by using the HPC.

As it was explained, these lenses have the peculiarity that depending on head movements and eye movements the resultant image is different. Future work have to be done to continue developing all the possible movements that can be achieved when wearing progressive addition lenses.

## CHAPTER 4

## CONCLUSIONS AND FUTURE WORK

In Chapter 1, the principal components of the optical system of the eye were briefly outlined to understand a condition that every human being develops when aging: Presbyopia. Common treatments for presbyopia were reviewed. Since there are trade-offs with each option, the wearer must make an informed decision as to which treatment is most suitable for their needs. One such treatment that will be the focus of this dissertation is the Progressive Addition Lens (PAL). The optical design of PALs is only the beginning of providing a beneficial treatment to the presbyope. PALs need to be accurately fabricated and high quality metrology is needed to verify the accuracy of the surface form. Furthermore, an understanding of the impact of various design choices on the perceived image of the wearer is needed to ensure comfort. This dissertation studied different techniques for the surface validation of PALs, as well as, provided insight into their on-eye performance. The particularities in the design of the freeform optical surface and their effect on the wearer were also explained.

Chapter 2 discusses the freeform surface verification of a KODAK Progressive Addition Lens. Four different metrology techniques were applied to measure the freeform surface of the PAL. The first two contact methods, the stylus profilometer and the Coordinate Measurement Machine, were used to get a point cloud of the freeform surface. These data were fitted to Zernike polynomials to get a mathematical description of the surface. Mean Curvature and Cylinder power maps were obtained to present the variation without discontinuity of optical power, as well as the presence of astigmatism over the surface.

Two non-contact methods for the freeform surface of the PAL were also presented. The first, SCOTS by refraction, gave a difference between the surface shape obtained

with the profilometer data and that from SCOTS. The discrepancy between the measures is likely due to assumptions made in the SCOTS procedure. Most notably, the back surface of the PAL was assumed to be spherical. As explained in Chapter 2, a perfect spherical surface was used in the Zemax model. In reality, the back surface will have its own inherent shape that will deviate from a true sphere and will introduce additional aberrations into the transmitted pattern in the SCOTS test. Future work to better characterize the back surface is required to isolate the effects of the freeform surface. Since the back surface is nearly spherical, this characterization could be done with traditional interferometry. An additional improvement to the SCOTS testing would be a distortion correction of the camera used.

UV Deflectometry was proposed in this dissertation as the second non-contact method. The proposed system used UV light to take advantage of the fact that PMMA lens material is opaque in this wavelength region. The opacity avoids ghost reflections from the back surface and parasitic fringes. For the method, a UV LED and Koehler illumination was used. However, in this configuration the fringe pattern needed to be projected onto a diffuser screen placed near the PAL. In turn the diffuser screen required the camera system to be at a large oblique angle to the test surface. The oblique angle makes it difficult to view the reflection from the entire convex test surface, as well as makes the aperture of the lens appear elliptical in the captured image. Using a reference sphere with a radius of curvature close to the radius of curvature of the freeform surface under test, a novel calibration method based on the correction by distortion was presented. Proof of concept of this method is shown.

While some obliquity between the projector and the camera is needed for the deflectometry technique, the configuration should be modified to help reduce the current angle. One option would be to use the UV LED as the source with a Digital Mirror Device (DMD). DMDs are at the heart of digital light projectors and using a DMD would enable projecting the fringes directly onto the test surface and enable the camera to be better placed for measurement.

Chapter 3 examines the surface shape relation with the visual performance of the PAL. By using the recovered surface in Chapter 2, simulation of three-dimensional images for multifocal vision was performed based on the psfs obtained using raytracing code. A psf database was created for different fields of view and different object depths. An algorithm was proposed where interpolated psfs for different fields of view were obtained. Preliminary images for a real scene were obtained, simulating what the wearer will see through progressive addition lenses at different glaze angles. An improvement for the simulation techniques would be a new method to get smooth transitions between the various depth planes. As previously explained, these spectacle lenses have the particularity that the image they produce is different depending on the head movement and eye rotation. Simulation of different orientation of the head and eye rotations needs to be performed.

The 360 camera can be useful to cover different parts of the real-world simulating head movement. The simulations were performed using only one lens, but the full 360-degree field of vision can be implemented. Furthermore, the scene can be composed of objects that are precisely localized, accurately positioned and a trilinear interpolation can be implemented to find the intermediate psf at many different depth planes. The main limitation to this implementation is computation time. Another important aspect is to test is whether PAL wearers have the same perception with real scenes and with simulation. If this connection is made, then the simulator can be used for virtually developing and testing new lenses.

The metrology techniques in this research demonstrated a new technique without expensive optical elements for the characterization of a freeform surface shape. After surface characterization, simulated images were presented for giving insight into the visual effects of PALs. While these results demonstrate the feasibility of UV deflection testing and simulation of PAL surface, the preceding suggestions for future work would lead to highly useful tools for the designer.

APPENDIX A  
ZERNIKE COEFFICIENTS

Zernike Term	Coefficient	Zernike Term	Coefficient
$Z_0^0$	-4.7180157	$Z_5^5$	$-7.2969642e - 03$
$Z_1^1$	$-3.5617096e - 02$	$Z_5^{-5}$	$-1.8477838e - 03$
$Z_1^{-1}$	$2.3376195e - 01$	$Z_6^0$	$3.2297570e - 04$
$Z_2^0$	$-2.8049186e + 00$	$Z_6^{-2}$	$2.7415363e - 03$
$Z_2^{-2}$	$1.6454016e - 02$	$Z_6^2$	$-2.2802097e - 03$
$Z_2^2$	$1.1759363e - 01$	$Z_6^{-4}$	$3.7286833e - 03$
$Z_3^{-1}$	$8.0809995e - 02$	$Z_6^4$	$-9.9409519e - 03$
$Z_3^1$	$1.3185891e - 03$	$Z_6^{-6}$	$2.6577480e - 03$
$Z_3^{-3}$	$2.2177069e - 02$	$Z_7^6$	$4.7804542e - 03$
$Z_3^3$	$5.7142848e - 03$	$Z_7^{-1}$	$2.2723415e - 03$
$Z_4^0$	$-5.8313036e - 02$	$Z_7^1$	$-2.4705662e - 04$
$Z_4^2$	$6.2111703e - 03$	$Z_7^{-3}$	$3.2513658e - 03$
$Z_4^{-2}$	$-1.5268369e - 02$	$Z_7^3$	$3.2424832e - 03$
$Z_4^4$	$3.9797824e - 02$	$Z_7^{-5}$	$-2.7655744e - 04$
$Z_4^{-4}$	$-6.7483869e - 03$	$Z_7^5$	$3.4022549e - 03$
$Z_5^1$	$2.3821696e - 03$	$Z_7^{-7}$	$6.9019242e - 05$
$Z_5^{-1}$	$-1.3839537e - 02$	$Z_7^7$	$3.1857329e - 04$
$Z_5^3$	$-7.9774266e - 03$	$Z_8^0$	$-2.7129996e - 03$
$Z_5^{-3}$	$-1.3605726e - 02$		

TABLE A.1. 37 Zernike Coefficients after fitting.



## APPENDIX B

SOURCE CODE USED TO PERFORM SIMULATION OF  
MULTIFOCAL VISION.

```

%Main program.
tic
%Open image that represents the scene.

rgbImage = imread('scene.jpg');
rgbImage=double(rgbImage);

%Decomposed it into RGB channels.
redChannel=double(rgbImage(:, :, 1));
greenChannel = double(rgbImage(:, :, 2));
blueChannel = double(rgbImage(:, :, 3));
A=redChannel;
B=greenChannel;
C=blueChannel;

sizeY=size(A,1);
sizeX=size(A,2);

% Load psf databased.
far='psf_images37Zern_11x11.mat';
int='psf_images37Zern_11x11_933mm.mat';
near='psf_images37Zern_11x11_660mm.mat';

images_far=load(far);
images_int=load(int);
images_near=load(near);

depth=[660;930;2000];
fieldy =[images_far.psf_images(:).fieldY];
fieldx =[images_far.psf_images(:).fieldX];

% Choose depth to simulate.
depth_1=660;

```

```

pitch=6;
cropSize=32;

[fieldX_degrees , fieldY_degrees]=meshgrid(linspace(-30,30,
    sizeX) , linspace(-30,30,sizeY));
new_filterSize2=floor(cropSize/2);

final=padarray(zeros(size(A)) , [new_filterSize2
    new_filterSize2]);
final_green=padarray(zeros(size(A)) , [new_filterSize2
    new_filterSize2]);
final_blue=padarray(zeros(size(A)) , [new_filterSize2
    new_filterSize2]);

%Performed Bilinear interpolation and superpostion of psfs
    for different
    %RGB Channel.
for ii=1:sizeX
for jj=1:sizeY

    [minFieldX , maxFieldX]=getNearFields(fieldx , fieldX_degrees(jj ,
        ii) , pitch);
    [minFieldY , maxFieldY]=getNearFields(fieldy , fieldY_degrees(jj ,
        ii) , pitch);

    images=images_far;

    if minFieldX==maxFieldX && minFieldY==maxFieldY
        psf=findFieldPSF(minFieldX , minFieldY , images);
        psf=imresize(psf , [cropSize , cropSize]);
    else

        [A1_region1]=findFieldPSF(minFieldX , minFieldY , images);
        [B1_region1]=findFieldPSF(maxFieldX , minFieldY , images);
        [C1_region1]=findFieldPSF(minFieldX , maxFieldY , images);
        [D1_region1]=findFieldPSF(maxFieldX , maxFieldY , images);

        psf=myInterpol3cases(fieldX_degrees(jj , ii) , fieldY_degrees(jj ,
            ii) , A1_region1 , B1_region1 , C1_region1 , D1_region1 , minFieldX
            , maxFieldY , maxFieldX , minFieldY , cropSize);
    end

```

```

new_psf_red= A(jj , ii).*psf;
new_psf_green= B(jj , ii).*psf;
new_psf_blue= C(jj , ii).*psf;
B_red= padarray(zeros(size(A)),[new_filterSize2
    new_filterSize2]);
B_green= padarray(zeros(size(A)),[new_filterSize2
    new_filterSize2]);
B_blue= padarray(zeros(size(A)),[new_filterSize2
    new_filterSize2]);
for k= 1:length(new_psf_red)
B_red(1+(jj-1):length(new_psf_red)+(jj-1),k+((ii-1)))=
    new_psf_red(:,k);
B_green(1+(jj-1):length(new_psf_green)+(jj-1),k+((ii-1)))=
    new_psf_green(:,k);
B_blue(1+(jj-1):length(new_psf_blue)+(jj-1),k+((ii-1)))=
    new_psf_blue(:,k);
end
final=final+B_red;
final_green=final_green+B_green;
final_blue=final_blue+B_blue;

end
end

%Normalized data
red_out=final./max(final(:));
red_out=imcrop(red_out,[new_filterSize2,new_filterSize2,size(
    A,2),size(A,1)]);
green_out=final_green./max(final_green(:));
green_out=imcrop(green_out,[new_filterSize2,new_filterSize2,
    size(A,2),size(A,1)]);
blue_out=final_blue./max(final_blue(:));
blue_out=imcrop(blue_out,[new_filterSize2,new_filterSize2,
    size(A,2),size(A,1)]);

%Add channels to get final scene
output=cat(3,(red_out),(green_out),(blue_out));

dlmwrite('red_far_0828.txt',red_out);
dlmwrite('green_far_0828.txt',green_out);

```

```
dlmwrite('blue_far_0828.txt',blue_out);
```

```
toc
```

```
Functions called by main program.
```

```
%
```

```
% Function Developed by Dulce.
```

```
% Visual and Ophthalmic Optics Lab, College of Optical  
Sciences, University of
```

```
% Arizona, Tucson, AZ. July 2018
```

```
%
```

```
%
```

```
% Given a point in the field function returns the maximum and  
minimum field
```

```
% in obne direction.
```

```
%
```

```
%
```

```
function [minField , maxField]=getNearFields(field ,field_2find  
 ,pitch)
```

```
[dif , ind_min]=min(abs(field-field_2find));
```

```
if dif==0
```

```
minField=field(ind_min);
```

```
maxField=field(ind_min);
```

```
else
```

```
op(1)=abs((field(ind_min)-pitch)-field_2find);
```

```
op(2)=abs((field(ind_min)+pitch)-field_2find);
```

```
[newField , indNewField]=min(op(:));
```

```
if indNewField==1
```



```
function [A, index]=findFieldPSF(fieldX , fieldY , images)
xsubField=fieldX;
ysubField=fieldY;
```

```
% images=openPSFfiles(depth_1 , depth);
% images=load(fileName);
```

```
for ii=1:length(images.psf_images)
if images.psf_images(ii).fieldX==xsubField(1) & images.
    psf_images(ii).fieldY==ysubField(1)
A=flipud(images.psf_images(ii).map);
index=ii;
end
end
```

```
%
```

```
%%%%%%%%%%%%%%%%%%%%%%%%%%%%%%%%%%%%%%%%%%%%%%%%%%%%%%%%%%%%%%%%%%%%%%%%%
```

```
% Function Developed by Dulce.
% Visual and Ophthalmic Optics Lab, College of Optical
% Sciences, University of
% Arizona, Tucson, AZ. March 2018
%
```

```
%%%%%%%%%%%%%%%%%%%%%%%%%%%%%%%%%%%%%%%%%%%%%%%%%%%%%%%%%%%%%%%%%%%%%%%%%
```

```
%
```

```
% Function interpolate PSF using Bilinear interpolation.
% Equations can be
% found in https://en.wikipedia.org/wiki/
% Bilinear_interpolation), given a set
% of basis functions, 4 corners and the coordinates to
% interpolate. Pixels
% in this case
% The input parameters are 4 matrices with the PSF that are
% going to be
% used to get the interpolation, the pixels position of this
% matrices x1, x2, y1,
% and y2 (be carefull with how matlab read pixels), and the
% final size of
% the PSF. 64 works fine, 256 kills computer.
```

```

% The output will be the interpolated matrix.
% (Program that calls this code: 'principal.m')
%
%
%%%%%%%%%%%%%%%%%%%%%%%%%%%%%%%%%%%%%%%%%%%%%%%%%%%%%%%%%%%%%%%%%%%%%%%%

%
% USAGE (SAMPLE CODE)
% positionX=10;
% positionY=10;
% cropSize=64;
% x1=1;
% y1=1;
% x2=25;
% y2=25;
%
% out(positionX , positionY).interpolation=myInterpol(positionX
    , positionY , A,B,C,D,x1,y2,x2,y1 , cropSize);
%
%%%%%%%%%%%%%%%%%%%%%%%%%%%%%%%%%%%%%%%%%%%%%%%%%%%%%%%%%%%%%%%%%%%%%%%%

function [out]=myInterpol3cases(x,y , A,B,C,D,x1,y1,x2,y2 ,
    cropSize)

%Arrays to interpolate
Q12=A;
Q22=B;
Q11=C;
Q21=D;

if x1==x2

out=((y2-y)/(y2-y1))*Q11+((y-y1)/(y2-y1))*Q12;
%     out=((y2-y)/(y2-y1))*Q22+((y-y1)/(y2-y1))*Q21;
out=imresize(out , [ cropSize , cropSize ] );

elseif y1==y2
out=((x2-x)/(x2-x1))*Q12+((x-x1)/(x2-x1))*Q22;
%     out=((x2-x)/(x2-x1))*Q11+((x-x1)/(x2-x1))*Q21;

```

```

out=imresize(out,[cropSize,cropSize]);

else
%Find Coefficients Bilinear interpolation
a0= ((Q11*x2*y2)/((x1-x2)*(y1-y2)))+((Q12*x2*y1)/((x1-x2)*(y2
-y1)))+((Q21*x1*y2)/((x1-x2)*(y2-y1)))+((Q22*x1*y1)/((x1-
x2)*(y1-y2)));
a1= ((Q11*y2)/((x1-x2)*(y2-y1)))+((Q12*y1)/((x1-x2)*(y1-y2))
+((Q21*y2)/((x1-x2)*(y1-y2)))+((Q22*y1)/((x1-x2)*(y2-y1))
);
a2= ((Q11*x2)/((x1-x2)*(y2-y1)))+((Q12*x2)/((x1-x2)*(y1-y2))
+((Q21*x1)/((x1-x2)*(y1-y2)))+((Q22*x1)/((x1-x2)*(y2-y1))
);
a3= (Q11/((x1-x2)*(y1-y2)))+(Q12/((x1-x2)*(y2-y1)))+(Q21/((x1
-x2)*(y2-y1)))+(Q22/((x1-x2)*(y1-y2)));

%X,Y to find

ii=x;
jj=y;

out=imresize(a0+(a1*ii)+(a2*jj)+(a3*ii*jj),[cropSize,cropSize
]);

end
end

```



## REFERENCES

- [1] C. M. Schor, “Accommodation and Presbyopia.” [Accessed: 2018-11-07].
- [2] A. VisionCare, “Multifocal intraocular lenses: Restor and tecnis multifocal iol.” [Accessed: 2018-10-31].
- [3] A. VisionCare, “Alcon multifocal contact lenses.” [Accessed: 2018-10-31].
- [4] R. D. Blum, W. Kokonaski, V. S. Iyer, J. N. Haddock, and M. Mattison-Shupnick, “Multifocal lens having a progressive optical power region and discontinuity,” Nov. 13 2012. US Patent 8,308,295.
- [5] P. Artal, “Optics of the eye and its impact in vision: a tutorial,” *Advances in Optics and Photonics*, vol. 6, no. 3, pp. 340–367, 2014.
- [6] J. Schwiegerling, “Field guide to visual and ophthalmic optics,” Spie, 2004.
- [7] L. A. Ostrin and A. Glasser, “Accommodation measurements in a prepresbyopic and presbyopic population,” *Journal of Cataract & Refractive Surgery*, vol. 30, no. 7, pp. 1435–1444, 2004.
- [8] D. A. Atchison, “Accommodation and presbyopia,” *Ophthalmic and Physiological Optics*, vol. 15, no. 4, pp. 255–272, 1995.
- [9] R. Gil-Cazorla, S. Shah, and S. A. Naroo, “A review of the surgical options for the correction of presbyopia,” *British Journal of Ophthalmology*, pp. bjophthalmol–2015, 2015.
- [10] A. Lichtinger and D. S. Rootman, “Intraocular lenses for presbyopia correction: past, present, and future,” *Current opinion in ophthalmology*, vol. 23, no. 1, pp. 40–46, 2012.
- [11] S. Jain, I. Arora, and D. T. Azar, “Success of monovision in presbyopes: review of the literature and potential applications to refractive surgery,” *Survey of ophthalmology*, vol. 40, no. 6, pp. 491–499, 1996.
- [12] E. S. Bennett, “Contact lens correction of presbyopia,” *Clinical and experimental optometry*, vol. 91, no. 3, pp. 265–278, 2008.
- [13] W. J. Duncan, *Visual Acuity Estimation from Simulated Images*. PhD thesis, University of Arizona, 2016.
- [14] T. E. Fannin and T. Grosvenor, *Clinical optics*. Butterworth-Heinemann, 2013.

- [15] C. This, “The optics of free-form progressive lenses,”
- [16] D. J. Meister and S. W. Fisher, “Progress in the spectacle correction of presbyopia. part 1: Design and development of progressive lenses,” *Clinical and experimental optometry*, vol. 91, no. 3, pp. 240–250, 2008.
- [17] D. J. Meister and S. W. Fisher, “Progress in the spectacle correction of presbyopia. part 2: Modern progressive lens technologies,” *Clinical and experimental optometry*, vol. 91, no. 3, pp. 251–264, 2008.
- [18] D. R. Pope, “Progressive addition lenses: history, design, wearer satisfaction and trends,” in *Vision Science and Its Applications*, p. NW9, Optical Society of America, 2000.
- [19] D. Lochegnies, P. Moreau, F. Hanriot, and P. Hugonneaux, “3d modelling of thermal replication for designing progressive glass moulds,” *New Journal of Glass and Ceramics*, vol. 3, no. 01, p. 34, 2013.
- [20] Z. Yin, Y. Dai, S. Li, C. Guan, and G. Tie, “Fabrication of off-axis aspheric surfaces using a slow tool servo,” *International Journal of Machine Tools and Manufacture*, vol. 51, no. 5, pp. 404–410, 2011.
- [21] Y. Y. Li, J. J. Chen, H. H. Feng, C. Li, J. Qu, and H. Chen, “Freeform manufacturing of a progressive addition lens by use of a voice coil fast tool servo,” in *7th International Symposium on Advanced Optical Manufacturing and Testing Technologies: Advanced Optical Manufacturing Technologies*, vol. 9281, p. 92810Q, International Society for Optics and Photonics, 2014.
- [22] M. F. Küchel, “Interferometric measurement of rotationally symmetric aspheric surfaces,” in *Optical Measurement Systems for Industrial Inspection VI*, vol. 7389, p. 738916, International Society for Optics and Photonics, 2009.
- [23] J. C. Wyant and F. D. Smith, “Interferometer for measuring power distribution of ophthalmic lenses,” *Applied optics*, vol. 14, no. 7, pp. 1607–1612, 1975.
- [24] C. Castellini, F. Francini, and B. Tiribilli, “Hartmann test modification for measuring ophthalmic progressive lenses,” *Applied optics*, vol. 33, no. 19, pp. 4120–4124, 1994.
- [25] J. Schwiegerling, *Optical specification, fabrication, and testing*. SPIE Press, 2014.
- [26] I. M. CMM Solutions, “Cmm history, fifty years of cmm history leading up to measuring revolution.” [Accessed: 2018-11-12].

- [27] G. P. Butel, G. A. Smith, and J. H. Burge, "Optimization of dynamic structured illumination for surface slope measurements," in *Interferometry XVI: Techniques and Analysis*, vol. 8493, p. 84930S, International Society for Optics and Photonics, 2012.
- [28] P. Su, R. E. Parks, L. Wang, R. P. Angel, and J. H. Burge, "Software configurable optical test system: a computerized reverse hartmann test," *Applied Optics*, vol. 49, no. 23, pp. 4404–4412, 2010.
- [29] P. Su, M. Khreishi, T. Su, R. Huang, M. Z. Dominguez, A. V. Maldonado, G. P. Butel, Y. Wang, R. E. Parks, and J. H. Burge, "Aspheric and freeform surfaces metrology with software configurable optical test system: a computerized reverse hartmann test," *Optical Engineering*, vol. 53, no. 3, p. 031305, 2013.
- [30] M. Z. Dominguez, L. Wang, P. Su, R. E. Parks, and J. H. Burge, "Software configurable optical test system for refractive optics," in *22nd Congress of the International Commission for Optics: Light for the Development of the World*, vol. 8011, p. 80116Q, International Society for Optics and Photonics, 2011.
- [31] W. Zhao, R. Huang, P. Su, and J. H. Burge, "Aligning and testing non-null optical system with deflectometry," in *Optical System Alignment, Tolerancing, and Verification VIII*, vol. 9195, p. 91950F, International Society for Optics and Photonics, 2014.
- [32] D. Malacara, *Optical shop testing*. John Wiley & Sons, 2007.
- [33] Rocoesy, "Pc/pmma." [Accessed: 2018-09-27].
- [34] C. Faber, E. Olesch, R. Krobot, and G. Häusler, "Deflectometry challenges interferometry: the competition gets tougher!," in *Interferometry XVI: Techniques and Analysis*, vol. 8493, p. 84930R, International Society for Optics and Photonics, 2012.
- [35] A. Speck, B. Zelzer, M. Kannengießler, A. Langenbacher, and T. Eppig, "Inspection of freeform intraocular lens topography by phase measuring deflectometric methods," *Applied optics*, vol. 52, no. 18, pp. 4279–4286, 2013.
- [36] M. C. Knauer, J. Kaminski, and G. Hausler, "Phase measuring deflectometry: a new approach to measure specular free-form surfaces," in *Optical Metrology in Production Engineering*, vol. 5457, pp. 366–377, International Society for Optics and Photonics, 2004.
- [37] C. Faber, M. C. Knauer, and G. Häusler, "Can deflectometry work in presence of parasitic reflections?," in *Proc. DGaO*, vol. 110, p. A10, 2009.

- [38] J. W. Goodman, *Introduction to Fourier optics*. Roberts and Company Publishers, 2005.
- [39] J. S. Tyo and A. S. Alenin, *Field guide to linear systems in optics*. SPIE Press, 2015.
- [40] Z. L. M. Nicholson., “How to simulate high resolution images-zemax knowledge-base, october 31, 2008..” [Accessed: 2018-11-05].
- [41] Z. L. B. Goodwin., “What is the difference between the fft and huygens psf? -zemax knowledgebase, october 30, 2015..” [Accessed: 2018-06-25].
- [42] Kodak, “Tips product specification & processing guide kodak polarized progressive lens with nupolartm technology, march, 2000.” [Accessed: 2018-10-12].
- [43] L. Marc, “New techniques in computational photography, computer science department .stanford university..” [Accessed: 2018-09-09].
- [44] B. A. Barsky, “Vision-realistic rendering: simulation of the scanned foveal image from wavefront data of human subjects,” in *Proceedings of the 1st Symposium on Applied perception in graphics and visualization*, pp. 73–81, ACM, 2004.
- [45] J. A. Rodríguez Celaya, P. Brunet Crosa, N. Ezquerro, and J. Palomar, “A virtual reality approach to progressive lenses simulation,” in *XV Congreso Espanol de Informatica Grafica*, 2005.
- [46] S. Shah and J. Aggarwal, “Intrinsic parameter calibration procedure for a (high-distortion) fish-eye lens camera with distortion model and accuracy estimation,” *Pattern Recognition*, vol. 29, no. 11, pp. 1775–1788, 1996.
- [47] G. documentation, “Lens distortion.” [Accessed: 2018-11-06].
- [48] R. C. Gonzalez, R. E. Woods, *et al.*, “Digital image processing,” 2002.
- [49] T. U. of Arizona, “High performance computing, information technology.” [Accessed: 2018-10-31].